RATIONAL ENGINEERING OF SEMICONDUCTOR NANOWIRE SUPERSTRUCTURES

A Dissertation
Presented to
The Academic Faculty

by

Ildar R. Musin

In Partial Fulfillment
of the Requirements for the Degree
Doctor of Philosophy in the
School of Chemical & Biomolecular Engineering

Georgia Institute of Technology
December 2013

RATIONAL ENGINEERING OF SEMICONDUCTOR NANOWIRE SUPERSTRUCTURES

Approved by:

Dr. Michael A. Filler, Advisor
School of Chemical & Biomolecular Engineering
Georgia Institute of Technology

Dr. Sankar Nair
School of Chemical & Biomolecular Engineering
Georgia Institute of Technology

Dr. Dennis W. Hess
School of Chemical & Biomolecular Engineering
Georgia Institute of Technology

Dr. Gleb Yushin
School of Materials Science and Engineering
Georgia Institute of Technology

Dr. Bernard Kippelen
School of Electrical and Computer Engineering
Georgia Institute of Technology

Date Approved: November 8, 2013

ACKNOWLEDGEMENTS

I would like to thank my advisor, Dr. Michael A. Filler, for the guidance through graduate school and these research projects. I would also like to thank my research group members for useful discussions and assistance through the years: Nae Chul Shin, Saujan Sivaram, Dmitriy Boyuk, Li-wei Chou, Ho Yee Hui, and Florencia Rusli. I would like to thank my thesis reading committee for the constructive comments on this work.

I would like to acknowledge the Air Force Office of Scientific Research, the National Science Foundation, support through the Georgia Tech Summer Undergraduate Research in Engineering (SURE) Program for their support of this research. Research was also supported by ORNL's Shared Research Equipment (ShaRE) User Program, which is sponsored by the Office of Basic Energy Sciences, the U.S. Department of Energy.

I would also like to acknowledge the technical support from J. Pham et al. at the Institute for Electronics and Nanotechnology (IEN) on the Georgia Institute of Technology campus. Significant part of the TEM characterization was performed at the Conn Center for Renewable Energy Research at the University of Louisville with the assistance of J. Jasinski. I would also like to thank W.-G. Kim for assistance with additional TEM imaging. Research was also supported by ORNL's Shared Research Equipment (ShaRE) User Program, which is sponsored by the Office of Basic Energy Sciences, the U.S. Department of Energy.

TABLE OF CONTENTS

LIST OF TABLES

LIST OF FIGURES

SUMMARY

Semiconductor nanowire synthesis provides a promising route to engineer novel nanoscale materials for applications in energy conversion, electronics, and photonics. In order to enable the appropriate function for a particular application, control of atomic and nanoscale structural details (e.g. diameter, orientation, faceting) is critical. The ability to engineer nanowire structure by tuning chemistry either at the nucleation point or on the sidewall is demonstrated in this work, thus enabling the rational fabrication of complex superstructures.

Chapter 3 demonstrates that methylgermane (GeH_3CH_3) can induce a transition from <111> to <110> oriented growth during the vapor-liquid-solid synthesis of Ge nanowires. This hydride-based chemistry is subsequently leveraged to rationally fabricate kinking superstructures based on combinations of <111> and <110> segments with user defined angles and segment lengths. The addition of GeH_3CH_3 also eliminates sidewall tapering and enables Ge nanowire growth at temperatures exceeding 475 °C, which greatly expands the process window.

Additionally, Chapters 4 and 5 demonstrate user-programmable diameter modulation using tetramethyltin ($Sn(CH_3)_4$) or trimethylsilane ($SiH(CH_3)_3$) reacting directly on the sidewalls of growing nanowires to either block or allow conformal deposition. Catalyst modification with tetramethyltin is demonstrated to decouple axial and radial growth kinetics and provides further control over nanowire design.

A method is presented in Chapter 5 for interrogating the kinetics of semiconductor nanowire growth via the vapor-liquid-solid (VLS) technique.

Morphological markers, generated via user-defined changes to diameter along the nanowire axial direction, enable the rapid, accurate, and facile extraction of growth rate information from electron microscopy images. $SiH(CH_3)_3$ is utilized for this purpose and does not permanently influence growth rate and kinking. As a proof of concept, we apply this approach to determine the diameter, temperature, and pressure dependence of Au-catalyzed Ge nanowire growth. These new synthetic strategies comprise a much needed toolbox for the precision engineering of nanoscale structures and materials properties.

CHAPTER 1

INTRODUCTION AND BACKGROUND

1.1 Demand for New Materials

Global energy consumption rate in 2008 was estimated to be 16.9 terawatts (TW), and is expected to rise to 25.8 TW by the year 2035.[1] The increasing demand for energy will eventually face the limited known supply of expendable energy sources, such as fossil fuels. Additionally, the result of deriving energy from oxidizing expendable carbon sources is the rapid accumulation of carbon dioxide in atmosphere at unprecedented levels compared to previous 500,000 years and observed changes in the pH of the oceans.[2] The desire to avoid the unpredictable results of chemical changes to the global atmosphere, to minimize and meet the energy demand, and to create sustainable nonexpendable energy sources for a secure energy future drives global research efforts on new methods of energy conversion and storage. Total capacities of renewable energies highlight the dominance of photovoltaics in their current technical potential of 340 TW, nearly two orders of magnitude above current global energy usage. Together with other dominant sustainable energy sources, such as wind and hydroelectricity, these processes largely rely on energy storage to be effective due to their intermittent nature.[2] However, to become cost competitive and more efficient, thus creating incentive for rapid change, new materials are in demand to complement new technologies and enable future progress. As new materials and structures have been explored, a myriad of improvements have been made over original concept designs in nearly every field of interest, including

energy generation and storage. For example, advances in photovoltaic materials have continuously progressed to higher efficiencies and lower costs aiding the large-scale expanding deployment.[3-6] Energy storage materials are improving as well in parallel.[7] Thermoelectrics for recovering wasted thermal heat to generate electricity or generate cooling and heating have also been moving progressively towards the goal of widespread use with new advances in materials.[8] The energy crisis requires a global approach on multiple fronts, with the aid of enabling technology and materials.

1.2 Group IV Materials

1.2.1 Industrial Compatibility

Group IV materials have a wide range of applications in many technologies of the energy landscape. Crystalline silicon (Si) and, to a lesser extent, germanium (Ge) are extensively used semiconductor materials in photovoltaics, transistors, computing, photonics, LEDs, etc. While the first transistors were made from Ge,[9] Si based transistors in computing have since taken over and stayed dominant for half a century.[10] Si-based solar cells dominate the photovoltaic markets and Ge finds many uses as a major component in most efficient multijunction solar cells, fiber optics, and infrared applications.[3, 11] These materials have the benefit of having been in the research spotlight for a long time with a vast amount of existing knowledge and industrial applications to ease the incorporation of new advances.

In order to scale up for meeting terawatt level energy challenges, abundance and extractability of raw materials becomes important. Ge is estimated at 1.4 ppm of Earth's crust,[12] with 128 tons of Ge refined and produced in 2012 mostly as a byproduct of zinc ore mining.[13] Nearly 70% of Ge consumption goes to optics and electronic end uses.[14] Si,

on the other hand, comprises nearly 25% of Earth's crust, with 7.4 million tons refined in 2011 with only about 3% going towards electronics-related applications.[12,15,16] While large scale bulk applications similar to Si of Ge may not be feasible, uses in specialized applications and in small (e.g. nanoscale) volumes are not out of the question. Additionally, these materials in elemental form have low toxicity avoiding contamination concerns.[17]

It is important to remember that exposure of Si and Ge to air leads to their oxide formation. Therefore, typically the depositions are done in vacuum environment under controlled conditions. There are also differences between their oxide qualities. Si oxide growth forms very smooth high quality electrically passivating layers, thus often used on purpose, while Ge oxide is uneven, rough, and filled with efficiency lowering defects.[18, 19] However, Ge chemical passivation is still possible, for example, via wet chemical approaches with long alkyl groups anchored by sulfur atoms.[19-22]

1.2.2 Basic Properties and Potential

Optoelectronic properties are particularly important for applications. Group IV materials hold potential for band gap engineering across a wide range of energies through alloying. Si and Ge semiconductor technologies have been expanding to the rest of group IV materials. Typically, Si and Ge display diamond cubic crystal structure, also observed in carbon (C) and tin (Sn). $Si_{1-x}Ge_x$ are miscible and well studied with band gaps varying between 0.66 eV of Ge and 1.12 eV of Si. Crystalline group IV materials band gap range has the potential to expand lower towards the 0 eV of metal-like Sn alloys, or higher towards 5.5 eV of C according to interpolation of Vegard's law with some alloy ranges already demonstrated.[23-27] Furthermore, while group IV alloys typically have indirect

band gaps, transitions to direct band gaps appear possible by forming alloys with Sn.[28, 29] Ideally, materials of various band gaps would be combined in a desired manner for target applications, such as to increase efficiency of capturing specific energy ranges of photons per layer. However, due to large variations in lattice sizes, these materials are difficult to combine to create heterostructures, such as the ones in highly efficient multijunction solar cells. Epitaxial growth of a crystal, used to create crystalline group IV materials, consists of forming a layer of material on top of pre-formed crystal that acts as a seed crystal and helps arrange new overlayer atoms into a certain crystallographic orientation. When the lattice size of the overlayers does not match, strain builds up. Strain often accumulates until the thin film thickness reaches a critical length, typically on the nanoscale, where it becomes enough to drive a defect formation for relaxation. For example, growth of lattice mismatched Ge_xSi_{1-x} films on top of Si causes a high density of dislocations.[30, 31] Due to the strain build up between mismatched bulk materials, defects and dislocations occur during growth creating recombination centers and strongly affecting end efficiencies.[32] Classically, lattice matching becomes important and severely restricts usable combinations in the bulk. Approaches that could allow material properties to be engineered with more flexibility are highly desired, such as finding methods to manipulate properties other than just compositionally and demonstrate ability for incorporation into application-demanded heterostructures. To this end, nanostructure offers to add additional options to expand the design space.

1.3 Nanostructures as Source of New Materials

Scaling down of materials has often been utilized to create a structure with new properties that enable new applications. The most direct effect of small scale structures is the increased ratio of surface area to volume, particularly useful for applications that require high surface area such as decreasing total material volume requirements for equivalent conversion in heterogeneous catalysis.[33] Electronics have also been scaling down exponentially following predictions of Moore's Law,[34] allowing more and more transistors and patterns on same area wafer that switch faster and reduce power losses.

As materials are scaled down, the amount of strain that can build up at their length scales decreases. Recent progress in battery capacity came from using nanoparticles, nanowires, and nanotubes that can expand dramatically by incorporating Li ions within the amorphous structure rapidly across high surface areas with strain relaxation preventing fracture.[35-37] Similarly, crystalline stiff materials in bulk can become flexible and elastic with higher Young's modulus at the nanoscale.[38, 39] In crystalline material, strain relaxation at the nanoscale is often observed naturally or can be utilized on purpose. While defect formation is one natural method of strain relaxation, surface roughness through nanostructures often forms as means of relaxing strain through the sidewalls. Lattice mismatched materials, including group IV, are known to naturally evolve nanodomes or nanowires as a method of strain relaxation.[40, 41] Alternatively, the feature sizes of the crystalline material could be specified precisely to allow strain relaxation in order to create defect free crystals and heterostructures. For example, nanowires with materials in an axial heterostructure have been demonstrated that have a

lattice mismatch as high as 14.6%.[42, 43] Highly strained material can also be deposited as a shell in a radial heterostructures around the wire.[44] This flexibility in accommodating mismatched materials in nanowires provides a viable platform for future device engineering.

Once the nanocrystal dimensions decrease, changes occur to density of electron states and available transitions due to the quantum confinement effects.[45-47] The dependence of semiconductor band gap on diameters of nanoparticles and nanowires has been demonstrated across a wide range of materials, including III-V's,[48] Si,[49-51] Ge,[52, 53] and $Si_{1-x}Ge_x$ alloys.[54] Additionally, transitions from indirect to direct band gaps at severely quantum confined nanowire diameters have been theorized.[55, 56] This provides an extra method for band gap engineering by simply changing the dimensions of nanomaterials.

Photon management becomes significantly important in photovoltaics where reflection losses have to be suppressed and absorption increased with structures that increase the optical path length through the material. The dimensions of nanostructures provide tools for enhanced scattering and light trapping.[57-59] Diameter, alignment, and spacing of nanowires have been shown to strongly affect their scattering strength and absorption enhancement.[60, 61] Diameter modulated nanowires have been theorized to enhance light trapping based on their chosen morphology.[62, 63] Light interaction with localized surface plasmon resonances has been demonstrated to be tunable in Si nanowires via a strong dependence on morphology and dopant concentrations.[64, 65] Efficient photon absorption with nanostructures may allow the reduction of the raw

materials consumption, thus lowering cost and allowing rarer and more expensive materials to be used efficiently.

Phonon scattering at the nanoscale is of particular interest for thermoelectric applications where high electric conductivity and low thermal conductivity are required. A discrete energy spectrum of quantum confined structures and higher electron effective masses provides electron filtering for increasing the Seebeck coefficient beneficial for thermoelectric efficiency.[66] Lattice thermal conductivity can be reduced through scattering phonons from point defects from alloying and scattering phonons at interfaces across the conduction path. Ideally this should be done without compromising crystallinity from epitaxy at interfaces for charge transport. Thin film superlattices take advantage of interface scattering and electron filtering, such as shown in SiGe superlattices[67] and nanowires.[68] This design is, potentially, an ideal match for nanowires due to their ability to form defect-free heterostructures with large mismatch to scatter phonons and tune quantum confinement. Silicon nanowires have shown experimental thermoelectric efficiencies much higher than in the bulk.[69] Additional roughness increases the efficiencies further by scattering phonons for thermal transport across a wider range.[70, 71] Diameter modulated nanowires have been theorized to give even higher efficiencies by precise tuning of the morphology.[72, 73] Geometric design of nanowires, such as through kinked structures, has also been found as a strong phonon scattering method.[74, 75] Direct electronic pathway provides for efficient charge transport without relying on electron hopping between particle interfaces, and offers high mobilities and fast charge carrier extractions.[37, 76-79]

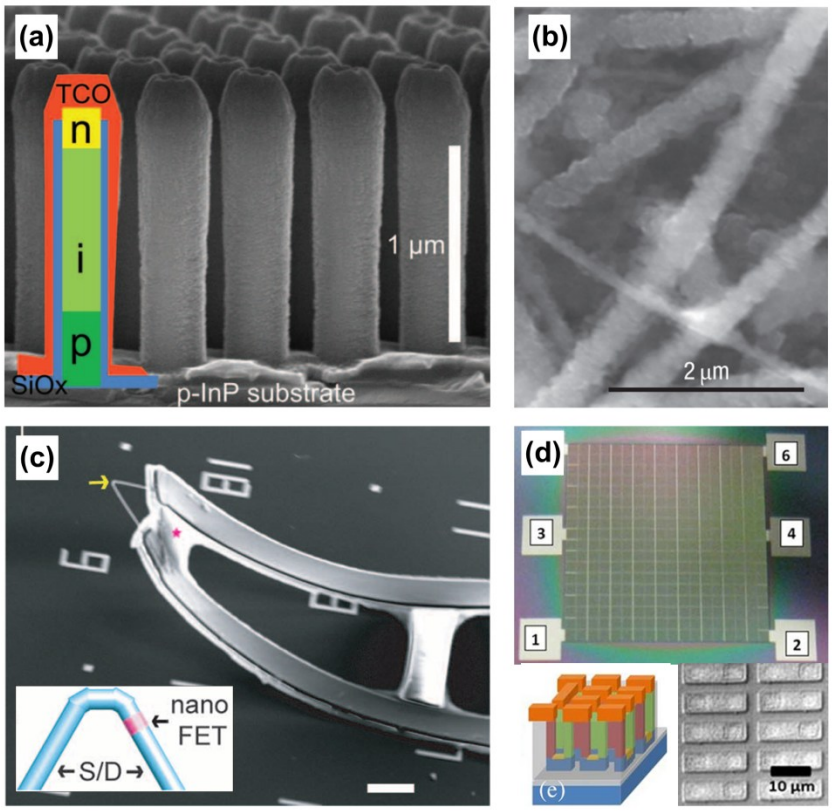

Figure 1.1 Highlights of some applications from nanowire-based prototype devices. (a) SEM of InP nanowire axial p-i-n doped heterostructures in a 13.8% efficient photovoltaic cell. From Wallentin et al.[80] Reprinted with permission from AAAS. (b) SEM of a high charge capacity Li battery anode made from Si nanowires that underwent lithiation. Reprinted by permission from Macmillan Publishers Ltd: Nature Nanotechnology, Chan et al.,[37] copyright 2008. (c) SEM of a three-dimensional field-effect transistor (FET) made from a kinked and dopant level modulated nanowire for chemical sensing applications. Inset shows the schematic of the nanowire FET component. From Tian et al.[81] Reprinted with permission from AAAS. (d) Photograph, schematic, and a close up SEM image of a thermoelectric power generator with charge carrier separation occurring in doped Si nanowire components. From Li et al., [82] © 2011 IEEE.

The higher surface area of nanowires could prove detrimental due to surface defects acting as centers for charge carrier recombination. However, surface passivation approaches are available options for Si and Ge nanowires with oxides,[83] carbon-based chemical species,[84, 85] and radial shells.[86] Furthermore, surface modification could become essential for 3-D band gap engineering in quantum confined systems, similar to

modifications to distribution of electronic states studied on surfaces and quantum dots.[87-89] Taking all these aspects into account, nanowires are of particular interest for high performance electronics. Nanowire architectures allow the combination of nanoscale attributes, such as strain relaxation, mismatched heterostructure formation, quantum confinement, light scattering, and phonon scattering with large scale direct charge transport.

Reported nanowire-based prototype devices vary greatly in applications among photovoltaics,[80, 90] energy storage,[37] sensors,[81] piezoelectrics,[91] thermoelectrics,[82, 92] nanoelectronics,[93] etc. Figure 1.1 highlights some of these demonstrations. In order to meet desired application demands through controlling the final material properties, corresponding structure must be first dictated through chemical synthesis. Ideally, production of desired materials should start with following an established chemistry-structure-property relationship. The expansion of the chemical "toolbox" to dictate basic aspects of material structure would enable their rational engineering. In the semiconductor nanowire case, even simply dictating morphological aspects, such as diameter and crystal orientation, is highly desired. Further progress demands research on improving current materials and pushing the limits of what is possible.

1.4 Growth of Group IV Semiconductor Nanowires

1.4.1 Manufacturing Approaches

There are two general approaches to creating semiconductor nanowire structures: top-down and bottom-up.[94, 95] The first is a top-down approach where unwanted material is removed through etching leaving behind the desired structure. The material has to be

first created in the bulk form, then patterned and consequently made to undergo a selective removal process. This approach typically takes multiple steps for completion and is limited by the synthetic limitations of the original bulk material and possible bulk heterostructures. Pattern lithography can be precise in positioning and shaping within a plane. Out of plane designs are limited in lithographic manufacturing approaches, but can still be demonstrated such as in FinFET and tri-gate MOSFET designs.[96]

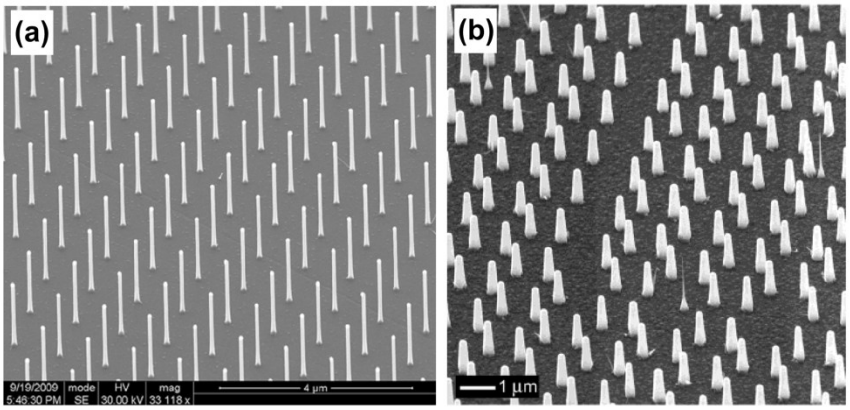

Figure 1.2 (a) SEM image of Ge nanowire array of user defined diameters and locations fabricated via placing the Au seed particles via electron-beam lithography followed by bottom-up nanowire growth. Reprinted with permission from Dayeh et al.[97] Copyright 2010 American Chemical Society. (b) SEM image of InP nanowire array with individual nanowires defined by diameter and location of Au seed particles via nanoimprint lithography followed by bottom-up growth. Reprinted with permission from Mårtensson et al.[98] Copyright 2004 American Chemical Society.

Alternatively, bottom-up fabrication is an additive process where desired structures are assembled directly from components. This can allow flexibility of specifying each layer directly. Nanowire bottom-up synthesis directly at the nanoscale offers the benefits of strain relaxation, potential ease of heterostructure formation, and provides options to break from planar design. Both approaches can also be combined, for example, by using the benefit of a top-down approach to dictate the precise location of where selective bottom-up growths will occur. Such combinations are demonstrated in

Figure 1.2 where electron-beam or nanoimprint lithography and lift-off techniques are utilized to dictate size and location of seed particles from which bottom-up growth can occur. The flexibility of a bottom-up approach for direct nanowire growth is of particular interest to build unique out of plane 3-D complexity directly, such as one offered by vapor-liquid-solid (VLS) nanowire growth mechanism.

1.4.2 Vapor-Liquid-Solid Growth

1.4.2.1 Growth Mechanism

The vapor-liquid-solid (VLS) growth mechanism, pioneered by Wagner in 1964, provides a systematic way to grow semiconductor nanowires.[99] VLS is a bottom-up technique that can be utilized with a chemical vapor deposition approach where gaseous precursor species containing desired atoms are flown over a substrate with a liquid catalyst. The precursor decomposition into the catalyst droplet leads to alloying, supersaturation, and precipitation of a solid crystalline nanowire at the liquid-solid interface. The continuous supply of vapor precursors continues to force supersaturation and 'layer by layer' epitaxial crystal nucleation events for continuous growth of the nanowire with the size of the liquid droplet constraining the diameter at the growth front. Diameter of the nanowire is dictated by the size and saturation solubility of the catalyst droplet at the top, in addition to the force balance between liquid, solid, and vapor interfaces at the triple phase line.[100] Similar vapor-solid-solid (VSS) growth has also been reported where the catalyst appears to be solid during nanowire growth.[101, 102] The epitaxial growth of crystalline nanowires allows orientation control by growth from a crystalline substrate. By matching the conditions of known nanowire crystal growth

orientation to the same normal of the substrate plane, ordered vertical aligned nanowires have been demonstrated to be grown.[103-105]

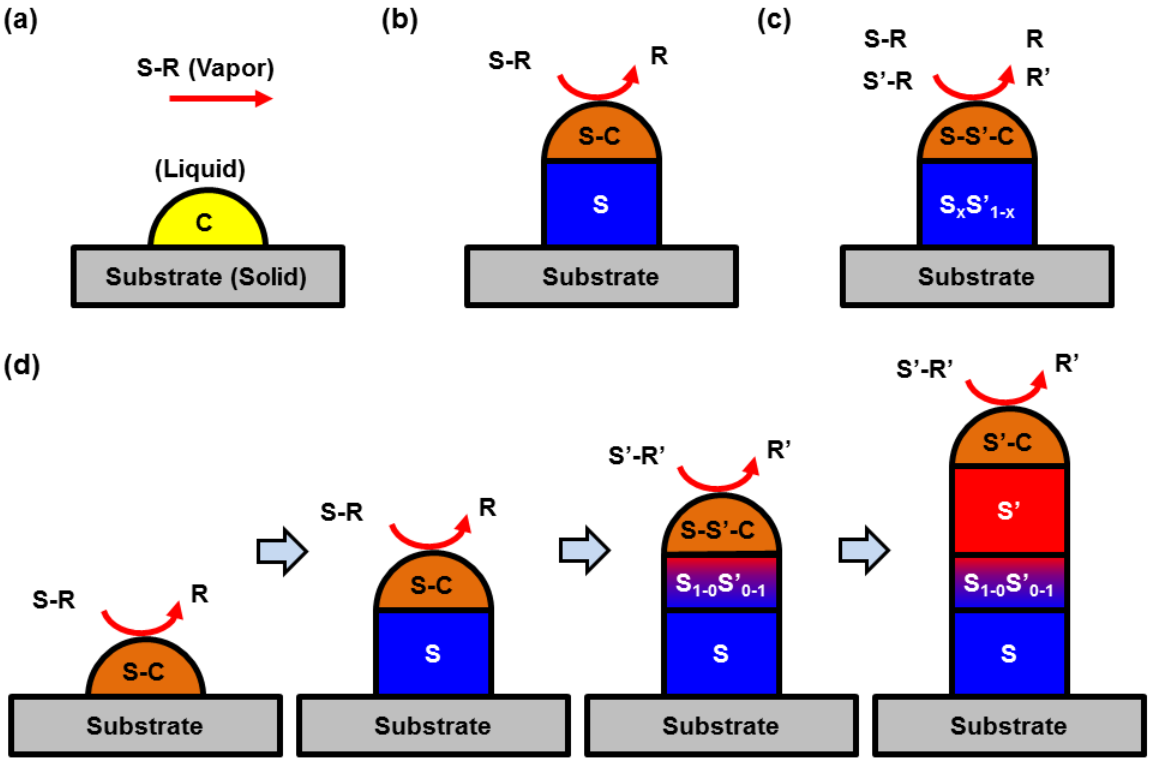

Figure 1.3 General schematic of VLS growth via chemical vapor deposition. (a) Identification before decomposition of the vapor phase precursor S-R, liquid catalyst C, and solid phase substrate. (b) Basic VLS growth from one precursor S-R forming semiconductor material S and leaving groups from ligands R. (c) VLS growth from multiple concurrent precursors for forming compositional alloys. (d) Axial heterostructure formation with reservoir effect gradients omitted for simplicity.

As shown in Figure 1.3 schematics, by placing catalysts of desired size on a solid substrate (Figure 1.3a), the user can dictate the size and placement of grown nanowire structures (Figure 1.3b). S-R is the precursor species (e.g. GeH_4) that decomposes in the catalyst C (e.g. Au), forming a S-C alloy (e.g. Au-Ge eutectic), as R groups leave (e.g. H_2). As the droplet supersaturates, it precipitates the atoms S at the liquid-solid interface forming a solid nanowire made of species S (e.g. Ge diamond cubic lattice). By specifying atomic makeup of the vapor phase precursors, the user can dictate the atoms

that form an alloy with the catalyst and precipitate as a single material (Figure 1.3b) or as an alloy (Figure 1.3c). The combinations of the vapor phase precursors allows the corresponding control of composition (Figure 1.3c), while manipulations of the vapor phase precursors during growth allows for control over their axial composition profiles (Figure 1.3d). While switching precursors in gas phase stops the supply of previous atomic contribution to the catalyst, the catalyst can act as a reservoir of old atoms that will have to first be depleted below saturation before the precipitated material switches completely to new target compositions. This 'reservoir' effect is responsible for characteristic gradients observed at heterostructure junctions. However, compositionally abrupt heterostructures have been achieved through reducing the solubility of transient species in the catalyst before the precursor composition switch through in-situ catalyst alloying[106, 107] or solidifying the catalyst and relying on VSS nanowire growth.[108] This catalyst-assisted approach has since been successfully used for a wide range of material systems (metal oxides, elemental group IV, II-VI, III-V nanowires, and heterostructures) and their combinations demonstrating its wide flexibility.[109, 110]

Ideal VLS catalysts should allow precursor decomposition reactions at low temperatures, have insignificant vapor pressure, have insignificant solubility in the nanowire material, and allow saturation of the desired material in their alloy. For example, Ge-Au bulk liquid eutectic alloy, formed above 361 °C at 28 % atomic Ge content far below individual melting points (e.g. 1064 °C for bulk Au) , allows Ge atoms to fully saturate the liquid alloy.[111] Additional effects are observed from the nanoscale of this binary system where smaller diameter eutectic droplets are able to have higher Ge content at the liquidus transition line at the same temperature, deviating from bulk

measurements.[112, 113] Figure 1.4 shows a binary Au-Ge phase diagram for the bulk in gray lines. The *in-situ* annealing (Figure 1.4a) and compositional analysis (Figure 1.4b) of liquidus transition as function of temperature and diameter are overlayed in the phase diagram. As expected from temperature dependent interface energy densities, the force balance at the triple phase line (Figure 1.4b inset schematic) was observed to change as a function of temperature, leading to changes in contact angles in Figure 1.4a. Diameter dependence of the observed liquidus line is attributed to smaller nanowire diameters requiring increased supersaturation for a phase transition, derived from the curvature dependent Gibbs-Thomson effect.[97] In addition, nanoscale VLS growth is often observed even far below the eutectic temperatures, once again deviating from the bulk phase thermodynamics. The subeutectic growth stabilization of the liquid eutectic phase is attributed to continuous supersaturation of Ge in the eutectic that prevents solid-Au nucleation in the Ge-rich environment. Furthermore, very small nanowire droplet alloys appear to have a substantial energy barrier to forming a diamond cubic crystal phase. [114, 115] With these effects, VLS growth of Ge nanowires has been observed at as low as 260 °C.[116]

Several events occur to initiate nanowire VLS growth. Gas phase species deliver semiconductor atoms to the surface of the droplet. Alternatively, exposed reactive semiconductor substrate can serve as an additional material source. The semiconductor atoms then begin to diffuse into the catalyst particle due to a concentration gradient, forming a new and growing Au-Si liquid alloy phase. This incubation step duration decreases with increasing temperature from an energy barrier governed diffusion process. The complete filling of the entire droplet to a state of supersaturation leads to a time

delay before nanowire growth can occur, increasing with larger diameters.[117, 118] However, at very small diameters the Gibbs-Thomson based increase in the chemical potential of the Au solid increases the catalyst alloying rate as well.[119] The relative time scales of Au particle liquification and nucleation of the diamond cubic nanowire material can lead to different growth mechanisms (e.g. VLS, VSS).[114, 120] As another transient process of initiating VLS growth, the droplet is forced to undergo a transition in the force balance from initial on-plane to the final top-of-pillar growth geometry, leading to rapid diameter changes at the base.[121] These issues with incubation can be avoided via often employed two step growth processes where all growth is initiated with high temperature incubation.[104]

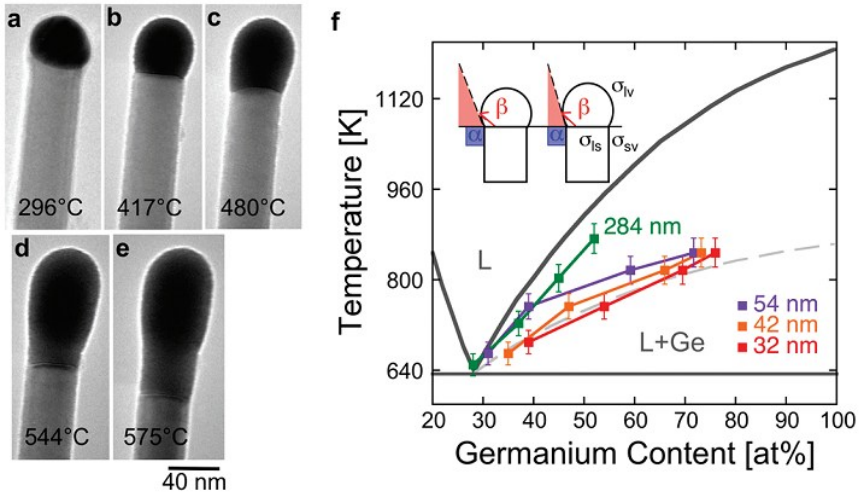

Figure 1.4 (a-e) *In situ* TEM images showing Ge nanowires with Au-Ge alloy tips annealed to specified temperatures. (f) Au-Ge binary allow phase diagram for bulk shown with gray lines. The data shown by the squares are the temperature dependent compositional measurements of the nanowire catalyst droplet for various diameters. Inset schematic signifies the change in the contact angle at the triple phase boundary observed upon increasing the temperature. Reprinted with permission from Sutter et al.[112] Copyright 2010 American Chemical Society.

Recent in-situ HRTEM nanowire growth studies reveal a periodically oscillating liquid-solid interface at the edge by the triple phase line in VLS growth (Si/Au, Si/Al,

Si/AlAu, Ge/Au, GaP/Au, α-Al_2O_3/Al nanowire/metal catalyst systems)[122-124] and even in VSS growth (Si/Cu system).[122] Figure 1.5 shows the schematic of such mechanism, using the Ge/Au system as an example, with the Ge nanowire growing in typical <111> direction. It is important to note that the <111> oriented nanowire shown here has 3-fold axial symmetry, thus from the observed zone axis only one truncated edge is clearly seen. Assuming continuous exposure to a Ge-containing precursor, once supersaturation of Ge in the droplet reaches critical value, a rate-limiting nucleation of a new bilayer occurs at the corner of the top {111} truncated facet in the liquid-solid interface[122] that then rapidly propagates across the liquid-solid interface adding to nanowire the length and raising the catalyst droplet (Figure 1.5a). As saturation drops after forming the bilayer, the material at the truncated edge is then quickly absorbed into the catalyst only to be slowly deposited back as supersaturation of the droplet increases (Figure 1.5b). While only a limited number of precursor and material systems were studied with in-situ microscopy and limitations in frame-rate resolution exist, no evidence was found for a previously assumed completely flat liquid-solid interface.[122]

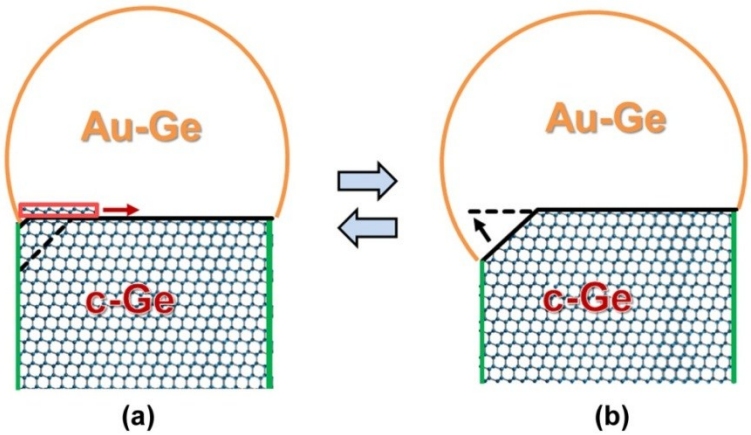

Figure 1.5 Schematic of layer by layer growth during Ge nanowire VLS growth during (a) rapid ledge flow and truncated edge depletion and (b) slow filling of the truncated edge.

1.4.2.2 Axial Kinetic Growth Models

Several growth kinetic models have been proposed since the discovery of VLS growth. Axial growth rate of elemental Si or Ge nanowires can be empirically estimated via a first order Arrhenius equation in the form

$$dL/dt = A \cdot \exp\left(\frac{-E_a}{RT}\right) \cdot P, \qquad (1.1)$$

where dL/dt is the axial growth rate, A is the pre-exponential factor, E_a is the activation energy, R is the gas constant, T is the temperature, and P is the partial pressure of the vapor species. However, additional concerns such as adatom diffusion to the catalyst may require additional parameters.[125] The nearly first order pressure dependence is often observed and has been used to claim precursor decomposition as the rate-limiting step. However, nucleation kinetics also depend on supersaturation and can be affected by pressure and flux. Furthermore, activation energy has been reported to be diameter-dependent as well.[126] Nanowires often show a decrease in growth rate at smaller diameters, often attributed to increased vapor pressure and solubility of the material due to curvature and the Gibbs-Thomson effect. To this end, nucleation at liquid-solid interface has also been considered as the rate limiting step.[127]

An alternative empirical model has often been used to describe nucleation based kinetics:

$$dL/dt = b\left(\frac{\Delta\mu_0}{kT} - \frac{4\Omega\gamma_{VS}}{kTd}\right)^2, \qquad (1.2)$$

where b is a temperature-dependent kinetic coefficient independent of supersaturation, $\Delta\mu_0$ is the difference in chemical potentials from vapor and solid phases, k is the Boltzmann constant, T is the temperature, Ω is the atomic volume of the solid, γ_{VS} is the

surface energy density of the vapor-solid interface, and d is nanowire liquid-solid interface diameter. Quadratic dependence was shown to fit experimental data and can be approximated only for a limited range through facet growth modeling.[97, 127, 128]

Finally, another version of the growth rate expression is often used based on the classical nucleation theory in a supersaturated liquid for 2-D islands overcoming a barrier for creating a nucleus of a critical size in a liquid in a form similar to:

$$dL/dt = V_0 \cdot \exp\left(-\frac{\Omega\gamma_{nuc}{}^2}{kT\Delta\mu}\right), \qquad (1.3)$$

where the pre-exponential factor V_0 often includes attachment frequency, Zeldovich factor describing the size-dependent curvature of the energy profile for forming a nucleus, and monomer concentration, and γ_{nuc} is the variously weighted surface energy density of a nucleating facet. $\Delta\mu$ is the actual difference in chemical potentials of liquid and solid phases that can incorporate the curvature-dependent Gibbs-Thomson effects.[123, 129]

While these and other versions of models proposed[130-134] all show some fitting ability to real data, the fits are largely empirical. The difficulty in proving the validity of a particular expression becomes easily evident when considering testing individual components of the theoretical equations, such as real-time surface energies, concentrations, and reaction kinetics across the three non-equilibrium fluctuating phases. Unexpected reported phenomena, for example simple diameter independence in Si nanowire growth from disilane,[135] demonstrate a lack of a clear unifying and predictive theory. The kinetic analysis of these observations suggests that poorly understood evaporation and reverse reactions may exist and play a significant role in VLS growth.[134]

1.4.3 Reactions on the Nanowire Surfaces

Nanowire sidewalls form at the edges of the catalyst droplet during epitaxial growth by the VLS method. Surface facets are often observed for Si and Ge nanowire growth.[136, 137] In the Si-Au case, surface faceting has been previously assigned to forces generated at the triple-phase line,[138] and Au wetting leading to morphological decomposition of larger facets.[139] Au wetting of sidewalls is often not observed for Ge nanowires,[140] but can be found as temperatures are increased.[141] Catalyst migration on sidewalls is often undesirable, but can be chemically controlled at higher hydride pressures or through surface modification (e.g. oxidation, carbon deposition).[142-145] Adatom diffusion (e.g. Si, Ge) can also play an increasing role at higher temperatures in formation of facets and add to VLS growth.[146, 147]

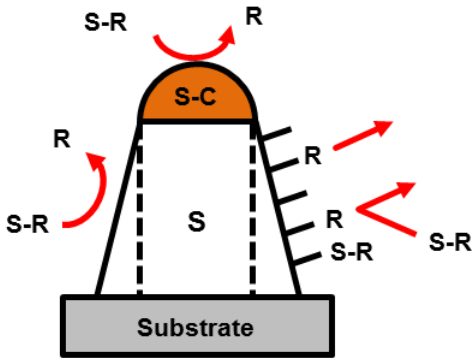

Figure 1.6 Schematic of vapor-solid chemical vapor deposition causing tapering during VLS growth. S – semiconductor atoms, R – ligands and leaving groups.

Additional major changes in diameter from growths of sidewall facets, observed as tapering, come from conformal vapor-solid (VS) deposition at elevated temperatures.[148, 149] VLS growth from vapor species is not always limited only to axial growth, but also concurrent radial expansion through the vapor-solid reactions can occur. Figure 1.6 shows a general schematic for vapor-solid reactions, analogous to thin film

growth. The tapered form can appear simply from the sidewall further down being exposed longer to conformal deposition. In chemical vapor deposition (e.g. from SiH_4, GeH_4), the delivery of additional species with the precursor (e.g. –H) results in blocking of surface sites needed for further VS decomposition until their rate-limiting desorptions.[150, 151] It has been also suggested that the presence of surface species at lower temperatures can limit the adatom diffusion caused faceting and lead to planar growth.[152]

Radial reactions and corresponding film growth can be utilized for creation of user-defined core-shell radial heterostructures.[44, 153] However, the attempts to create strictly axial specific compositional and dopant profiles can be complicated by undesired radial deposition and resulting profiles.[125, 154, 155] Recently, the use of surface-reaction blocking species, such as C_2H_2, have been demonstrated to prevent incorporations at the sidewall.[145]

1.4.4 Ge Nanowires as a Representative Material

Ge nanowires, in particular, are a good and promising platform for investigation of Group IV potential at the nanoscale. Ge offer higher intrinsic carrier mobilities and concentrations over Si, and good compatibility with silicon processes.[156] Additionally, Ge nanowires achieve quantum confinement at larger more accessible diameters due to a larger Bohr exciton radius of 24.3 nm than Si at 4.9 nm, a characteristic length scale near which available electronic energy states begin to vary from bulk.[157] Ge is less reactive with molecular O_2 than Si,[158] which is difficult without ultra-high vacuum conditions, at base pressures more industrially accessible. Ge is also known for forming less stable germanides with transition metals when compared to silicides of Si.[159] Furthermore, resistance of Ge to Au wetting the sidewalls could offer more control over sidewalls. Ge-

Au VLS offers a relevant and simple system to use as a basis for exploring chemical processes and forming a general "toolbox" for creating nanowire architectures, which could then be expanded to and combined with other more complex material systems.

1.5 Motivation for Current Research

The understanding of chemistry-structure-property relationship is essential for improving current nanowire applications and exploring the unknown accessible phase space of structures and properties. As the simple synthetic approaches with precursors from thin film chemistry are rapidly explored, additional approaches become desired. For example, specific pressure and temperature conditions have been reported to alter VLS grown axial nanowire orientations,[160, 161] defect introduction,[162, 163] and tapering.[104, 149] However, the observations were largely empirical and lacked fundamental certainty of the underlying processes.

Recently, several other studies have connected the possibility that chemical reactions on the sidewall and near the triple phase line can be responsible for morphological and structural changes of nanowires. Si_2H_6 growth of Si nanowires at various pressures and temperatures was studied in-situ to correlate changes in axial growth orientation to the presence of transient surface hydrogen and confirmed with atomic hydrogen.[164] Hydrogen rich conditions were then used for user defined twin and stacking fault introduction.[165] Chemically induced Si nanowire kinking via oxygen introduction has also been demonstrated.[166] Diameter modulation from user defined blocking and allowing conformal deposition through a shell formation from the catalyst has been demonstrated in Ge nanowires with C_2H_2/HCl[145] and O_2.[167] These studies

suggest chemistry at the triple phase line and further away from the droplet can be utilized in dictating final structure and building complexity from epitaxial VLS growth.

The concept of structural manipulation with chemistry has been previously utilized in other synthetic systems. Morphology control of nanocrystals in solution phase synthesis has been reported through selective surface passivation.[168, 169] Similarly, large differences in surface energies between facets based on orientation and passivation [170-172] can be utilized in VLS growth. Vacuum chemistry functionalization studies have been reported on many semiconductor surfaces, including Ge and Si.[173] Surface functionalization should allow changes in the force balance at the triple phase line, altering diameter, and related nanoscale effects such as supersaturation. Additionally it may allow selection or stabilization of preferential facets, governing crystal growth directions and radial growth. The goal of the following studies is to build a chemical 'toolbox" and gain the fundamental understanding for the rational synthesis of nanowires with user-defined structure.

Chapter 2 describes the equipment and methods used in synthesis and analysis of VLS grown nanowires used throughout this work. Chapter 3 will describe the study of methylgermane effect on basic VLS GeH_4 chemistry for the synthesis of Ge nanowires. The study takes advantage of stable methyl termination on Ge at low temperature, analogous to the mentioned hydrogen effect on Si nanowires. The study successfully gains control over nanowire crystal growth orientation between <111> and <110> directions at user defined periodicity. Additionally, methyl groups are shown to successfully prevent tapering, expanding the temperature phase space for constant diameter nanowires.[174]

Tetramethyltin precursor is used to deliver a resist during growth to prevent conformal deposition without inducing kinking in Chapter 4. Switching between exposure to tetramethyltin and regular GeH_4 growth allows synthesis of diameter modulated nanowires with user defined diameter profiles. Additionally, control over axial growth rate is achieved through Au catalyst alloying with Sn.[175] Chapter 5 takes advantage of trimethylsilane for diameter modulation without the permanent alloying effect to create diameter modulated superstructures. The process conditions for individual segments of the superstructures are modulated within a single wire for rapid exploration of the synthetic phase space. An empirical expression for the axial growth rate dependence on temperature, pressure, and Au gold colloid diameter is extracted from these structures. The summary of the conclusions and future outlook are provided in chapter 6. This work successfully adds to the modern understanding of the chemistry-structure relationship from exploring the precursor chemistry effect on nanowire structure and allows rational engineering of nanowire morphology through orientation and diameter control.

1.6 References

1. U.S. Energy Information Administration, International Energy Outlook 2011, Report No. DOE/EIA-0484(2011)

2. N. S. Lewis and D. G. Nocera, *Proc. Natl. Acad. Sci. U.S.A.*, 2006, **103**, 15729-15735.

3. C. A. Wolden, J. Kurtin, J. B. Baxter, I. Repins, S. E. Shaheen, J. T. Torvik, A. A. Rockett, V. M. Fthenakis and E. S. Aydil, *J. Vac. Sci. Technol. B*, 2011, **29**, 030801-030816.

4. B. K. Meyer and P. J. Klar, *Phys. Status Solidi RRL*, 2011, **5**, 318-323.

5. A. Goetzberger and C. Hebling, *Sol. Energy Mater. Sol. Cells*, 2000, **62**, 1-19.

6. C. Wadia, A. P. Alivisatos and D. M. Kammen, *Environ. Sci. Technol.*, 2009, **43**, 2072-2077.

7. H. Chen, T. N. Cong, W. Yang, C. Tan, Y. Li and Y. Ding, *Prog. Nat. Sci.*, 2009, **19**, 291-312.

8. L. E. Bell, *Science*, 2008, **321**, 1457-1461.

9. J. Bardeen and W. H. Brattain, *Phys. Rev.*, 1948, **74**, 230-231.

10. B. E. Deal and J. M. Early, *J. Electrochem. Soc.*, 1979, **126**, 20C-32C.

11. M. A. Green, K. Emery, Y. Hishikawa, W. Warta and E. D. Dunlop, *Prog. Photovoltaics*, 2013, **21**, 827-837.

12. K. Hans Wedepohl, *Geochim. Cosmochim. Acta*, 1995, **59**, 1217-1232.

13. GERMANIUM, U.S. Geological Survey, Mineral Commodity Summaries, January 2013 www.usgs.gov

14. Germanium, U.S. GEOLOGICAL SURVEY 2011 MINERALS YEARBOOK www.usgs.gov

15. SILICON, U.S. Geological Survey, Mineral Commodity Summaries, January 2013 www.usgs.gov

16. SILICON, U.S. GEOLOGICAL SURVEY 2011 MINERALS YEARBOOK www.usgs.gov

17. Center for Disease Control and Prevention, The National Institute for Occupational Safety and Health "International Chemical Safety Cards" www.cdc.gov

18. E. Yablonovitch, D. L. Allara, C. C. Chang, T. Gmitter and T. B. Bright, *Phys. Rev. Lett.*, 1986, **57**, 249-252.

19. P. W. Loscutoff and S. F. Bent, *Annu. Rev. Phys. Chem.*, 2006, **57**, 467-495.

20. J. M. Buriak, *Chem. Rev.*, 2002, **102**, 1271-1308.

21. D. Knapp, B. S. Brunschwig and N. S. Lewis, *J. Phys. Chem. C*, 2010, **114**, 12300-12307.

22. J. L. He, Z. H. Lu, S. A. Mitchell and D. D. M. Wayner, *J. Am. Chem. Soc.*, 1998, **120**, 2660-2661.

23. M. Jaros, *Rep. Prog. Phys.*, 1985, **48**, 1091-1154.

24. J. Kouvetakis, J. Menendez and A. V. G. Chizmeshya, *Annu. Rev. Mater. Res.*, 2006, **36**, 497-554.

25. W. Windl, O. F. Sankey and J. Menendez, *Phys. Rev. B*, 1998, **57**, 2431-2442.

26. P. Melinon, B. Masenelli, F. Tournus and A. Perez, *Nat Mater*, 2007, **6**, 479-490.

27. J. B. Casady and R. W. Johnson, *Solid-State Electron.*, 1996, **39**, 1409-1422.

28. P. Moontragoon, P. Pengpit, T. Burinprakhon, S. Maensiri, N. Vukmirovic, Z. Ikonic and P. Harrison, *J. Non-Cryst. Solids*, 2012, **358**, 2096-2098.

29. M.-Y. Ryu, T. R. Harris, Y. K. Yeo, R. T. Beeler and J. Kouvetakis, *Appl. Phys. Lett.*, 2013, **102**, 171908.

30. P. M. Mooney, *Mater. Sci. Eng. R-Rep.*, 1996, **17**, 105-146.

31. R. People and J. C. Bean, *Appl. Phys. Lett.*, 1985, **47**, 322-324.

32. H. J. Queisser and E. E. Haller, *Science*, 1998, **281**, 945-950.

33. J. Y. Ying, *Chem. Eng. Sci.*, 2006, **61**, 1540-1548.

34. G. E. Moore, *Proc. IEEE*, 1998, **86**, 82-85.

35. A. S. Arico, P. Bruce, B. Scrosati, J.-M. Tarascon and W. van Schalkwijk, *Nat Mater*, 2005, **4**, 366-377.

36. Y. Yang, G. Zheng and Y. Cui, *Chem. Soc. Rev.*, 2013, **42**, 3018-3032.

37. C. K. Chan, H. L. Peng, G. Liu, K. McIlwrath, X. F. Zhang, R. A. Huggins and Y. Cui, *Nat. Nanotechnol.*, 2008, **3**, 31-35.

38. J. He and C. M. Lilley, *Nano Lett.*, 2008, **8**, 1798-1802.

39. C. Q. Chen, Y. Shi, Y. S. Zhang, J. Zhu and Y. J. Yan, *Phys. Rev. Lett.*, 2006, **96**, 075505.

40. D. J. Eaglesham and M. Cerullo, *Phys. Rev. Lett.*, 1990, **64**, 1943-1946.

41. D. C. Nesting, J. Kouvetakis and D. J. Smith, *Appl. Phys. Lett.*, 1999, **74**, 958-960.

42. K. A. Dick, S. Kodambaka, M. C. Reuter, K. Deppert, L. Samuelson, W. Seifert, L. R. Walenberg and F. M. Ross, *Nano Lett.*, 2007, **7**, 1817-1822.

43. P. Caroff, M. E. Messing, B. M. Borg, K. A. Dick, K. Deppert and L. E. Wernersson, *Nanotechnology*, 2009, **20**, 495606.

44. I. A. Goldthorpe, A. F. Marshall and P. C. McIntyre, *Nano Lett.*, 2008, **8**, 4081-4086.

45. A. P. Alivisatos, *Science*, 1996, **271**, 933-937.

46. T. Takagahara and K. Takeda, *Physical Review B*, 1992, **46**, 15578-15581.

47. A. M. Smith and S. Nie, *Acc. Chem. Res.*, 2009, **43**, 190-200.

48. J. Arbiol, M. de la Mata, M. Eickhoff and A. F. i. Morral, *Mater. Today*, 2013, **16**, 213-219.

49. A. R. Guichard, D. N. Barsic, S. Sharma, T. I. Kamins and M. L. Brongersma, *Nano Lett.*, 2006, **6**, 2140-2144.

50. O. Demichel, V. Calvo, P. Noé, B. Salem, P. F. Fazzini, N. Pauc, F. Oehler, P. Gentile and N. Magnea, *Phys. Rev. B*, 2011, **83**, 245443.

51. S. Cahangirov and S. Ciraci, *Phys. Rev. B*, 2009, **80**, 075305.

52. S. Y. Ren, *Solid State Commun.*, 1997, **102**, 479-484.

53. J. R. Heath, J. J. Shiang and A. P. Alivisatos, *J. Chem. Phys*, 1994, **101**, 1607-1615.

54. J.-E. Yang, C.-B. Jin, C.-J. Kim and M.-H. Jo, *Nano Lett.*, 2006, **6**, 2679-2684.

55. C. Harris and E. P. O'Reilly, *Physica E*, 2006, **32**, 341-345.

56. L. Yang, R. N. Musin, X. Q. Wang and M. Y. Chou, *Phys. Rev. B*, 2008, **77**, 195325.

57. E. Garnett and P. D. Yang, *Nano Lett.*, 2010, **10**, 1082-1087.

58. B. S. Luk‘yanchuk, M. I. Tribelsky, V. Ternovsky, Z. B. Wang, M. H. Hong, L. P. Shi and T. C. Chong, *J. Opt. A*, 2007, **9**, S294.

59. J. Zhu, Z. Yu, S. Fan and Y. Cui, *Mater. Sci. Eng. R-Rep.*, 2010, **70**, 330-340.

60. O. L. Muskens, S. L. Diedenhofen, B. C. Kaas, R. E. Algra, E. P. A. M. Bakkers, J. Gómez Rivas and A. Lagendijk, *Nano Lett.*, 2009, **9**, 930-934.

61. L. Cao, P. Fan, A. P. Vasudev, J. S. White, Z. Yu, W. Cai, J. A. Schuller, S. Fan and M. L. Brongersma, *Nano Lett.*, 2010, **10**, 439-445.

62. G. Demesy and S. John, *J. Appl. Phys.*, 2012, **112**, 074326.

63. A. Deinega and S. John, *J. Appl. Phys.*, 2012, **112**, 074327.

64. L.-W. Chou, N. Shin, S. V. Sivaram and M. A. Filler, *J. Am. Chem. Soc.*, 2012, **134**, 16155-16158.

65. L.-W. Chou and M. A. Filler, *Angew. Chem. Int. Ed.*, 2013, **52**, 8079-8083.

66. G. J. Snyder and E. S. Toberer, *Nat. Mater.*, 2008, **7**, 105-114.

67. P. Hyldgaard and G. D. Mahan, *Phys. Rev. B*, 1997, **56**, 10754-10757.

68. D. Li, Y. Wu, R. Fan, P. Yang and A. Majumdar, *Appl. Phys. Lett.*, 2003, **83**, 3186-3188.

69. A. I. Boukai, Y. Bunimovich, J. Tahir-Kheli, J. K. Yu, W. A. Goddard and J. R. Heath, *Nature*, 2008, **451**, 168-171.

70. A. I. Hochbaum, R. K. Chen, R. D. Delgado, W. J. Liang, E. C. Garnett, M. Najarian, A. Majumdar and P. D. Yang, *Nature*, 2008, **451**, 163-U165.

71. M. G. Ghossoub, K. V. Valavala, M. Seong, B. Azeredo, K. Hsu, J. S. Sadhu, P. K. Singh and S. Sinha, *Nano Lett.*, 2013, **13**, 1564-1571.

72. X. Zianni, *Appl. Phys. Lett.*, 2010, **97**, 233106-233103.

73. X. Zianni, *Nanoscale Res. Lett.*, 2011, **6**, 1-6.

74. J.-S. Heron, C. Bera, T. Fournier, N. Mingo and O. Bourgeois, *Phys. Rev. B*, 2010, **82**, 155458.

75. J.-W. Jiang, N. Yang, B.-S. Wang and T. Rabczuk, *Nano Lett.*, 2013, **13**, 1670-1674.

76. H. Z. Song, K. Akahane, S. Lan, H. Z. Xu, Y. Okada and M. Kawabe, *Phys. Rev. B*, 2001, **64**, 085303.

77. J.-S. Lee, M. V. Kovalenko, J. Huang, D. S. Chung and D. V. Talapin, *Nat Nano*, 2011, **6**, 348-352.

78. X. Y. Chen and W. Z. Shen, *Appl. Phys. Lett.*, 2004, **85**, 287-289.

79. E. Galoppini, J. Rochford, H. Chen, G. Saraf, Y. Lu, A. Hagfeldt and G. Boschloo, *J. Phys. Chem. B*, 2006, **110**, 16159-16161.

80. J. Wallentin, N. Anttu, D. Asoli, M. Huffman, I. Åberg, M. H. Magnusson, G. Siefer, P. Fuss-Kailuweit, F. Dimroth, B. Witzigmann, H. Q. Xu, L. Samuelson, K. Deppert and M. T. Borgström, *Science*, 2013, **339**, 1057-1060.

81. B. Tian, T. Cohen-Karni, Q. Qing, X. Duan, P. Xie and C. M. Lieber, *Science*, 2010, **329**, 830-834.

82. Y. Li, K. Buddharaju, N. Singh, G. Q. Lo and S. J. Lee, *IEEE Electron Device Lett.*, 2011, **32**, 674-676.

83. O. Demichel, V. Calvo, A. Besson, P. No, B. Salem, N. Pauc, F. Oehler, P. Gentile and N. Magnea, *Nano Lett.*, 2010, **10**, 2323- 2329.

84. T. Hanrath and B. A. Korgel, *J. Am. Chem. Soc.*, 2004, **126**, 15466-15472.

85. M. Y. Bashouti, K. Sardashti, S. W. Schmitt, M. Pietsch, J. Ristein, H. Haick and S. H. Christiansen, *Prog. Surf. Sci.*, 2013, **88**, 39-60.

86. Y. Dan, K. Seo, K. Takei, J. H. Meza, A. Javey and K. B. Crozier, *Nano Lett.*, 2011, **11**, 2527-2532.

87. K. Dohnalova, A. N. Poddubny, A. A. Prokofiev, W. D. A. M. de Boer, C. P. Umesh, J. M. J. Paulusse, H. Zuilhof and T. Gregorkiewicz, *Light Sci. Appl.*, 2013, **2**, e47.

88. B. P. Bloom, L.-B. Zhao, Y. Wang, D. H. Waldeck, R. Liu, P. Zhang and D. N. Beratan, *J. Phys. Chem. C*, 2013, **117**, 22401-22411.

89. S. Yang, D. Prendergast and J. B. Neaton, *Nano Lett.*, 2011, **12**, 383-388.

90. Z. Y. Fan, H. Razavi, J. W. Do, A. Moriwaki, O. Ergen, Y. L. Chueh, P. W. Leu, J. C. Ho, T. Takahashi, L. A. Reichertz, S. Neale, K. Yu, M. Wu, J. W. Ager and A. Javey, *Nat. Mater.*, 2009, **8**, 648-653.

91. X. Wang, J. Song, J. Liu and Z. L. Wang, *Science*, 2007, **316**, 102-105.

92. J. Keyani, A. M. Stacy and J. Sharp, *Appl. Phys. Lett.*, 2006, **89**, 233106.

93. J. Goldberger, A. I. Hochbaum, R. Fan and P. Yang, *Nano Lett.*, 2006, **6**, 973-977.

94. B. Teo and X. H. Sun, *J. Cluster Sci.*, 2006, **17**, 529-540.

95. R. G. Hobbs, N. Petkov and J. D. Holmes, *Chem. Mater.*, 2012, **24**, 1975-1991.

96. B. Ho, S. Xin, S. Changhwan and L. Tsu-Jae King, *IEEE Trans. Electron Dev.*, 2013, **60**, 28-33.

97. S. A. Dayeh and S. T. Picraux, *Nano Lett.*, 2010, **10**, 4032-4039.

98. T. Mårtensson, P. Carlberg, M. Borgström, L. Montelius, W. Seifert and L. Samuelson, *Nano Lett.*, 2004, **4**, 699-702.

99. R. S. Wagner, W. C. Ellis, S. M. Arnold and K. A. Jackson, *J. Appl. Phys.*, 1964, **35**, 2993-3000.

100. V. Schmidt, J. V. Wittemann and U. Gosele, *Chem. Rev.*, 2010, **110**, 361-388.

101. F. M. Ross, *Rep. Prog. Phys.*, 2010, **73**, 114501.

102. J. L. Lensch-Falk, E. R. Hemesath, D. E. Perea and L. J. Lauhon, *J. Mater. Chem.*, 2009, **19**, 849-857.

103. J. H. Woodruff, J. B. Ratchford, I. A. Goldthorpe, P. C. McIntyre and C. E. D. Chidsey, *Nano Lett.*, 2007, **7**, 1637-1642.

104. H. Adhikari, A. F. Marshall, C. E. D. Chidsey and P. C. McIntyre, *Nano Lett.*, 2006, **6**, 318-323.

105. A. Lugstein, M. Steinmair, Y. J. Hyun, G. Hauer, P. Pongratz and E. Bertagnolli, *Nano Lett.*, 2008, **8**, 2310-2314.

106. D. E. Perea, N. Li, R. M. Dickerson, A. Misra and S. T. Picraux, *Nano Lett.*, 2011, **11**, 3117-3122.

107. K. A. Dick, J. Bolinsson, B. M. Borg and J. Johansson, *Nano Lett.*, 2012, **12**, 3200-3206.

108. C. Y. Wen, M. C. Reuter, J. Bruley, J. Tersoff, S. Kodambaka, E. A. Stach and F. M. Ross, *Science*, 2009, **326**, 1247-1250.

109. K. W. Kolasinski, *Curr. Opin. Solid State Mater. Sci.*, 2006, **10**, 182-191.

110. Kenry and C. T. Lim, *Prog. Mater Sci.*, 2013, **58**, 705-748.

111. J. Wang, C. Leinenbach and M. Roth, *J. Alloys Compd.*, 2009, **481**, 830-836.

112. E. A. Sutter and P. W. Sutter, *Acs Nano*, 2010, **4**, 4943-4947.

113. E. J. Schwalbach and P. W. Voorhees, *Nano Lett.*, 2008, **8**, 3739-3745.

114. A. D. Gamalski, J. Tersoff, R. Sharma, C. Ducati and S. Hofmann, *Nano Lett.*, 2010, **10**, 2972-2976.

115. H. Adhikari, A. F. Marshall, I. A. Goldthorpe, C. E. D. Chidsey and P. C. McIntyre, *Acs Nano*, 2007, **1**, 415-422.

116. S. Kodambaka, J. Tersoff, M. C. Reuter and F. M. Ross, *Science*, 2007, **316**, 729-732.

117. B. Kalache, P. R. i. Cabarrocas and A. F. i. Morral, *Jpn. J. Appl. Phys.*, **45**, L190.

118. F. Dhalluin, T. Baron, P. Ferret, B. Salem, P. Gentile and J.-C. Harmand, *Appl. Phys. Lett.*, 2010, **96**, 133109.

119. B. J. Kim, J. Tersoff, C. Y. Wen, M. C. Reuter, E. A. Stach and F. M. Ross, *Phys. Rev. Lett.*, 2009, **103**, 155701.

120. B. J. Kim, C. Y. Wen, J. Tersoff, M. C. Reuter, E. A. Stach and F. M. Ross, *Nano Lett.*, 2012, **12**, 5867-5872.

121. V. Schmidt, S. Senz and U. Gösele, *Appl. Phys. A*, 2005, **80**, 445-450.

122. C. Y. Wen, J. Tersoff, K. Hillerich, M. C. Reuter, J. H. Park, S. Kodambaka, E. A. Stach and F. M. Ross, *Phys. Rev. Lett.*, 2011, **107**, 025503.

123. A. D. Gamalski, C. Ducati and S. Hofmann, *J. Phys. Chem. C*, 2011, **115**, 4413-4417.

124. S. H. Oh, M. F. Chisholm, Y. Kauffmann, W. D. Kaplan, W. Luo, M. Rühle and C. Scheu, *Science*, 2010, **330**, 489-493.

125. K. K. Lew, L. Pan, E. C. Dickey and J. M. Redwing, *J. Mater. Res.*, 2006, **21**, 2876-2881.

126. J. H. Kim, S. R. Moon, H. S. Yoon, J. H. Jung, Y. Kim, Z. G. Chen, J. Zou, D. Y. Choi, H. J. Joyce, Q. Gao, H. H. Tan and C. Jagadish, *Cryst. Growth Des.*, 2011, **12**, 135-141.

127. E. I. Givargizov, *J. Cryst. Growth*, 1975, **31**, 20-30.

128. V. G. Dubrovskii and N. V. Sibirev, *Phys. Rev. E*, 2004, **70**, 031604.

129. N. Li, W. Li, L. Liu and T. Y. Tan, *J. Appl. Phys.*, 2013, **114**, 064302.

130. V. Schmidt, S. Senz and U. Gösele, *Phys. Rev. B*, 2007, **75**, 045335.

131. Y. Y. Lü, H. Cui, G. W. Yang and C. X. Wang, *Nano Lett.*, 2012, **12**, 4032-4036.

132. V. G. Dubrovskii, N. V. Sibirev, G. E. Cirlin, I. P. Soshnikov, W. H. Chen, R. Larde, E. Cadel, P. Pareige, T. Xu, B. Grandidier, J. P. Nys, D. Stievenard, M. Moewe, L. C. Chuang and C. Chang-Hasnain, *Phys. Rev. B*, 2009, **79**, 205316.

133. V. G. Dubrovskii, N. V. Sibirev, J. C. Harmand and F. Glas, *Phys. Rev. B*, 2008, **78**, 205316.

134. D. Shakthivel and S. Raghavan, *J. Appl. Phys.*, 2012, **112**, 024317.

135. S. Kodambaka, J. Tersoff, M. C. Reuter and F. M. Ross, *Phys. Rev. Lett.*, 2006, **96**, 096105.

136. T. Hanrath and B. A. Korgel, *Small*, 2005, **1**, 717-721.

137. F. Li, P. D. Nellist, C. Lang and D. J. H. Cockayne, *Acs Nano*, 2010, **4**, 632-636.

138. F. M. Ross, J. Tersoff and M. C. Reuter, *Phys. Rev. Lett.*, 2005, **95**, 146104.

139. C. Wiethoff, F. M. Ross, M. Copel, M. H. V. Hoegen and F. Heringdorf, *Nano Lett.*, 2008, **8**, 3065-3068.

140. E. Dailey, P. Madras and J. Drucker, *Appl. Phys. Lett.*, 2010, **97**, 143106.

141. M. Simanullang, K. Usami, T. Kodera, Y. Kawano and S. Oda, *J. Cryst. Growth*, 2013, **384**, 77-81.

142. P. Madras, E. Dailey and J. Drucker, *Nano Lett.*, **10**, 1759-1763.

143. J. B. Hannon, S. Kodambaka, F. M. Ross and R. M. Tromp, *Nature*, 2006, **440**, 69-71.

144. S. Kodambaka, J. B. Hannon, R. M. Tromp and F. M. Ross, *Nano Lett.*, 2006, **6**, 1292-1296.

145. B.-S. Kim, M. J. Kim, J. C. Lee, S. W. Hwang, B. L. Choi, E. K. Lee and D. Whang, *Nano Lett.*, 2012, **12**, 4007-4012.

146. L. Huang, F. Liu, G.-H. Lu and X. G. Gong, *Phys. Rev. Lett.*, 2006, **96**, 016103.

147. M. Kolibal, R. Kalousek, T. Vystavel, L. Novak and T. Sikola, *Appl. Phys. Lett.*, 2012, **100**, 203102.

148. F. Oehler, P. Gentile, T. Baron, P. Ferret, M. Den Hertog and J. Rouviere, *Nano Lett.*, **10**, 2335-2341.

149. S.-g. Ryu, E. Kim, J.-h. Yoo, D. J. Hwang, B. Xiang, O. D. Dubon, A. M. Minor and C. P. Grigoropoulos, *Acs Nano*, 2013, **7**, 2090-2098.

150. S. M. Gates and S. K. Kulkarni, *Appl. Phys. Lett.*, 1991, **58**, 2963-2965.

151. N. M. Russell and W. G. Breiland, *J. Appl. Phys.*, 1993, **73**, 3525-3530.

152. B. Cunningham, J. O. Chu and S. Akbar, *Appl. Phys. Lett.*, 1991, **59**, 3574-3576.

153. L. J. Lauhon, M. S. Gudiksen, C. L. Wang and C. M. Lieber, *Nature*, 2002, **420**, 57-61.

154. D. E. Perea, E. R. Hernesath, E. J. Schwalbach, J. L. Lensch-Falk, P. W. Voorhees and L. J. Lauhon, *Nat. Nanotechnol.*, 2009, **4**, 315-319.

155. P. Xie, Y. J. Hu, Y. Fang, J. L. Huang and C. M. Lieber, *Proc. Natl. Acad. Sci. U.S.A.*, 2009, **106**, 15254-15258.

156. L. Z. Pei and Z. Y. Cai, *Recent Pat. Nanotechnol.*, 2012, **6**, 44-59.

157. Y. Y. Wu and P. D. Yang, *Chem. Mater.*, 2000, **12**, 605-607.

158. X. L. Fan, W. M. Lau and Z. F. Liu, *J. Phys. Chem. C*, 2009, **113**, 8786-8793.

159. A. Pasturel, P. Hicter and F. Cyrot-Lackmann, *Physica B+C*, 1984, **124**, 247-250.

160. B. Tian, P. Xie, T. J. Kempa, D. C. Bell and C. M. Lieber, *Nat. Nanotechnol.*, 2009, **4**, 824-829.

161. P. Madras, E. Dailey and J. Drucker, *Nano Lett.*, 2009, **9**, 3826-3830.

162. P. Caroff, K. A. Dick, J. Johansson, M. E. Messing, K. Deppert and L. Samuelson, *Nat. Nanotechnol.*, 2009, **4**, 50-55.

163. S. A. Dayeh, J. Wang, N. Li, J. Y. Huang, A. V. Gin and S. T. Picraux, *Nano Lett.*, 2011, **11**, 4200-4206.

164. N. Shin and M. A. Filler, *Nano Lett.*, 2012, **12**, 2865-2870.

165. N. Shin, M. Chi, J. Y. Howe and M. A. Filler, *Nano Lett.*, 2013, **13**, 1928-1933.

166. K. W. Schwarz, J. Tersoff, S. Kodambaka, Y. C. Chou and F. M. Ross, *Phys. Rev. Lett.*, 2011, **107**, 265502.

167. C. J. Hawley, T. McGuckin and J. E. Spanier, *Cryst. Growth Des.*, 2013, **13**, 491-496.

168. Y. Yin and A. P. Alivisatos, *Nature*, 2005, **437**, 664-670.

169. X. Xia and Y. Xia, *Nano Lett.*, 2012, **12**, 6038-6042.

170. S. Hong and M. Y. Chou, *Phys. Rev. B*, 1998, **57**, 6262-6265.

171. A. A. Stekolnikov, J. Furthmüller and F. Bechstedt, *Phys. Rev. B*, 2002, **65**, 115318.

172. J.-M. Zhang, F. Ma, K.-W. Xu and X.-T. Xin, *Surf. Interface Anal.*, 2003, **35**, 805-809.

173. A. V. Teplyakov and S. F. Bent, *J. Vac. Sci. Technol. A*, 2013, **31**, 050810.

174. I. R. Musin and M. A. Filler, *Nano Lett.*, 2012, **12**, 3363-3368.

175. I. R. Musin, D. S. Boyuk and M. A. Filler, *J. Vac. Sci. Technol. B*, 2013, **31**, 020603.

CHAPTER 2

EXPERIMENTAL METHODS

2.1 Chemical Vapor Deposition Reactor

2.1.1 Introduction

Chemical vapor deposition (CVD) is a process where reactive gaseous chemical species are delivered to a substrate at which point they react and deposit to form a solid material. Any unreacted species or volatile byproducts are meanwhile removed in gas flow. In semiconductor industry such processes are often used to create films of amorphous, polycrystalline, or single crystalline material. FirstNano EasyTube 3000 CVD reactor was designed for custom nanoscale single crystalline group IV CVD chemistry for electronic materials ready for combinations of multiple highly reactive precursors for wide range of temperatures and pressures in a programmable fashion.

2.1.2 Gas Precursor Delivery Design

Silane (SiH_4, 99.999%, Air Products) and germane (GeH_4, 99.999%, Matheson Tri-Gas) gases are used as silicon and germanium precursors respectively. Other relevant gases include: hydrogen (H_2, 99.999%, AirGas), argon (Ar, 99.997%, Air Products), methylgermane (GeH_3CH_3, 97%, Gelest), trimethylsilane ($SiH(CH_3)_3$, 99.99%, Voltaix). Figure 2.1 shows a schematic for the gas lines used in the reactor. The gases are stored in the cylinders one floor below the reactor and are connected at minimum of 8 psig line pressure through submicron stainless steel filters to individual mass flow controllers (MFC) per gas source. Additionally, each MFC has an Ar purge line connected via

additional pneumatic valve. 316L seamless stainless steel lines and fittings are used throughout the reactor. Mass flow controllers (MKS) are calibrated by manufacturers specifications based on heat capacity and density of the precursors.

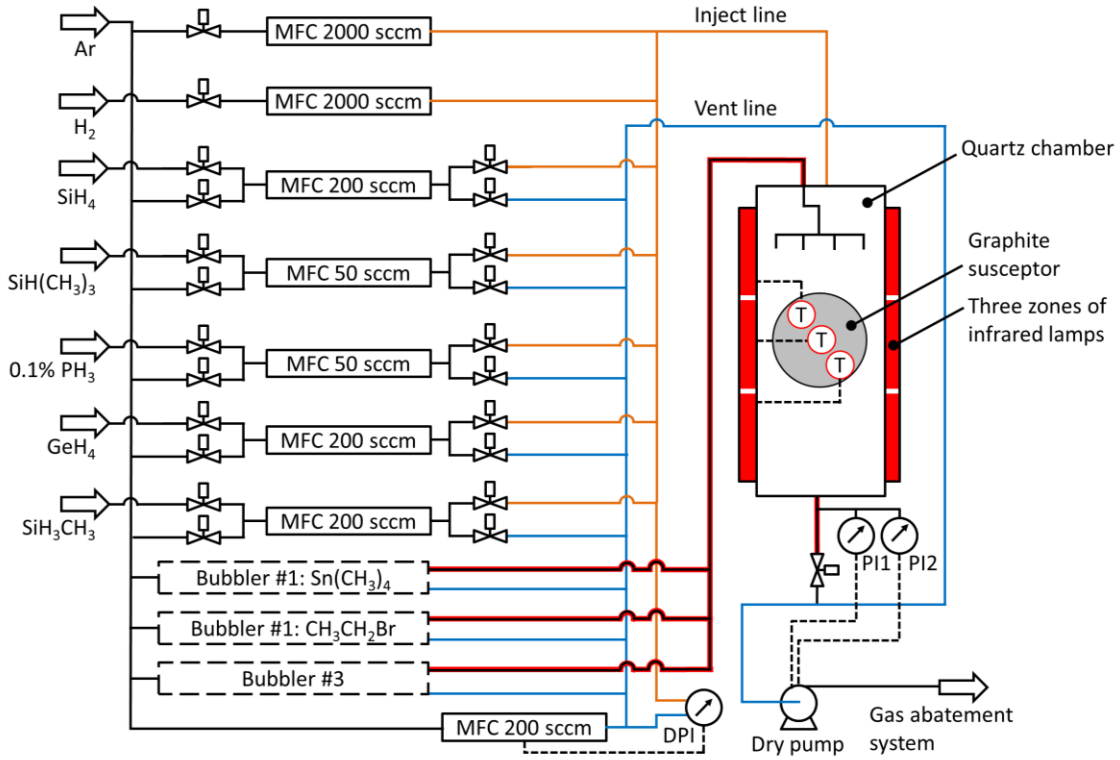

Figure 2.1. Schematic of the process lines in the reactor. Black line with red outline represents trace heated line. Orange lines are the inject lines into the quartz chamber. Blue lines bypass the chamber and head directly to pump. Standard bubbler schematic is shown separately in Figure 2.3 for three identical bubbler setups surrounded by long dashed lines. Short dashed lines represent microcontroller based feedback loops.

Pneumatic valves with mounted solenoids are used for rapid 0.005 second switching between open and closed states. If the pneumatic valves from gas line to MFC and from MFC to reaction chamber are open, the MFC deliver individual gases at set flowrates through the inject line into the chamber. Alternatively, when gas flows need to be stabilized, but not yet injected into the reaction chamber, the vent line is used that bypasses the reaction chamber. Through differential pressure sensor between vent line

and the inject line, with vent line controlled to same pressure via Ar MFC, gases can be switched between vent line (bypassing the chamber) to inject line (injecting into the chamber) without flowrates fluctuations. Figures 2.1 and 2.2 show the schematic and the physical images of the reactor.

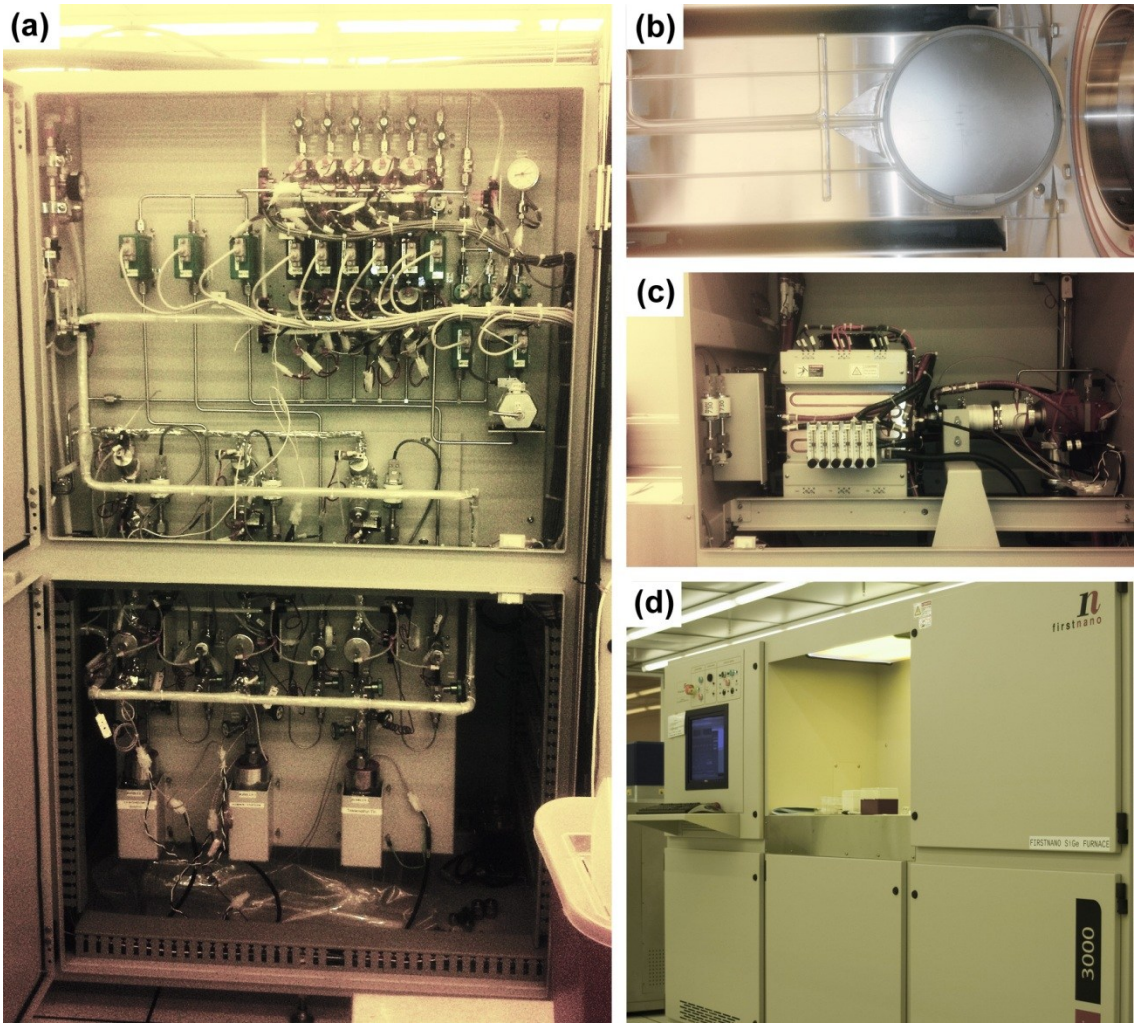

Figure 2.2. Photographs of (a) the precursor lines set up, (b) graphite susceptor, (c) infrared heating chamber with cooling water lines, and (d) reactor enclosure with computer interface.

2.1.3 Liquid and Solid Precursor Delivery

Multiple liquid precursors are also utilized: tetramethyltin ($Sn(CH_3)_4$, TMT, 98%, Strem Chemicals), bromoethane (CH_3CH_2Br, 99%, Sigma Aldrich). Figure 2.1 shows the

process schematic for liquid precursor lines used in the reactor with three identical bubblers, shown on Figure 2.3 schematic. Liquid precursors are stored in stainless steel bubblers inside the reactor case. Individual bubbler temperatures are monitored by a thermocouple in a stainless steel sheath embedded near the bottom center and controlled to set point (up to 130 °C) with an electric heating strip wrapping the bottom of the bubbler. The bubbler is additionally covered on the outside with a thick rubber sheet for thermal insulation.

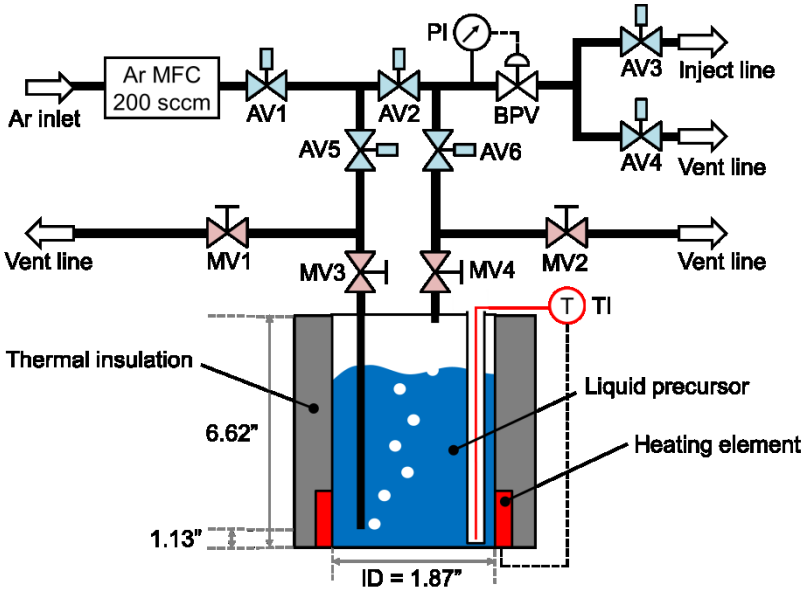

Figure 2.3. Schematic of the liquid precursor bubbler set up. MV are manual valves. AV are software controlled automatic valves. BPV is a backpressure valve. PI is a pressure indicator. TI is a temperature indicator.

Ar carrier gas is introduced at controllable flowrates (4-200 sccm) into the bubblers with an MFC through a line going to the bottom of the bubbler to allow Ar gas to bubble through the liquid or over a solid precursor before reaching the bubbler outlet line. The outlet leads to a pressure sensor in feedback loop to backpressure control valve that allows the bubbler pressure to be controlled independently higher than downstream line pressure. The outlet line temperature is independently controlled (up to 130 °C) all

the way to the reaction chamber. At the reaction chamber, a quartz tube distributes the flow of liquid precursors upstream across the susceptor.

The bubbler set up allows for controllable flowrates of precursors, with the assumption for full saturation of Ar carrier gas using the following equation:

$$F_L = F_{Ar} \frac{P^{sat}}{P_{bubbler} - P^{sat}}, \qquad (2.1)$$

where F_L is the flowrate of the liquid precursor, F_{Ar} is the Ar carrier gas flowrate, P^{sat} is the vapor pressure of the liquid precursor at bubbler temperature, and $P_{bubbler}$ is the pressure of the bubbler.

To achieve constant flowrate quickly with a backpressure valve, the following method is utilized. First, the bypass valve line (AV2 open, AV5 and AV6 closed) is brought to bubbler set point pressure and the bubbler is brought to temperature. Following, the bubbler pressure is brought to set point pressure with Ar (AV5 and AV6 open, AV2 closed). Immediately, the bypass bubbler line is used again to stabilize the flowrate at final Ar bubbler carrier gas set point and matching bubbler pressure. When the pneumatic valves are switched back to the bubbler, the pressure does not have to change significantly, and equilibrium pressure and flowrate of gas through liquid precursor is established quickly. The bubbler Ar carrier gas flowrate remains constant throughout the experiment to avoid re-stabilization. Stabilization is executed into the vent line, bypassing the reaction chamber, and remains there until needed for use. Once required, the flow is easily switched to and from inject line, leading to the chamber, without destabilizing the flowrate.

The bubbler level is estimated by filling the individual bubblers with exhaust closed from 300 to 400 Torr with Ar at 20 sccm and comparing the fill duration between

a filled and an empty bubbler. This approach roughly measures the available volume including the bubbler and local process lines.[1] As the time for pressure change approaches that of an empty bubbler, the bubbler is refilled in an air-free glovebox or in a fume hood followed by a freeze-pump-thaw procedure. The bubblers are connected and disconnected by evacuating the connection junction via MV1 and MV2 as labeled in Figure 2.3 to avoid air contamination and vapor exposure.

2.1.4 Pressure Controls

The pressure in the reaction chamber is controlled below 0.001 to above 500 Torr by two capacitance manometers (10.000 Torr and 1000.0 Torr maximum reading) in a feedback loop to variable speed dry vacuum pump (Busch BA100 70 CFM). The seal to the reaction chamber is differentially pumped between two Viton O-rings by a dedicated secondary pump to ensure effective seal. The leak up rate at base pressure is below 0.001 Torr per minute. The individual partial pressures are calculated via the following equation:

$$P_i = P_{Total} \frac{F_i}{F_{Total}}, \qquad (2.2)$$

where P_i is the partial pressure of precursor i, P total is the controlled total pressure of the chamber, F_i is the molar flowrate of the precursor i, and F_{Total} is the total molar flowrate of all precursors through the chamber.

2.1.5 Temperature Controls

Reaction chamber is a quartz tube surrounded by infrared lamps from top and bottom for cold wall heating of the graphite susceptor. The 4 inch diameter susceptor has three embedded K-type thermocouples across the length in a feedback loop to

corresponding three zones of infrared lamps for ±3 °C temperature uniformity across the length. The lamps are capable of heating and cooling the susceptor up to ±10 °C/sec. The effective temperature range is between 200-900 °C. For germanium wafers, where infrared light absorbs directly, only the bottom lamps are used, minimizing local heating from direct irradiation.

2.1.6 Reproducibility Measures

The reactor microcontrollers responsible for temperature, pressure, and flow rate control are programmable through software interface on a desktop computer with step by step recipe execution. Set points can be set in step wise or ramp manner. The values of all analog and digital readings are logged and stored continuously to the hard drive.

The quartz chamber, holder, and thermocouple sheaths were cleaned every several months in dilute HF. Graphite susceptor was cleaned via sandblasting. Multiple carrier wafers were used to reduce cross contamination. Between experiments involving liquid precursors, a cleaning recipe was used where 500 Torr of H_2 was brought up to 900 °C for 20-60 minutes with the carrier wafer inside the chamber.

The varying efficiency of the infrared lamps was dealt with by systematic calibration for steady state manual values across the desired temperature range to minimize variations over time. The total pressure was kept nearly identical across sets of experiments to minimize deviations in convective heat transfer.

2.1.7 Reactor Design Overview

The CVD reactor was constructed by First Nano based on custom specifications for simultaneous delivery of up to 8 different precursors in addition to Ar and H_2 carrier gasses. Individual mass flow controllers coupled with chamber pressure control allow

control over gas phase composition for exploration of the chemistry phase space. The number of precursor lines in addition to run-vent lines allow for rapid and vast changes in gas phase composition during growth for heterostructure formation and other synthetic opportunities. The three bubblers allow expanding precursor selection past limited commercial gas cylinder based precursors to vastly abundant less volatile liquid and solid phase precursors. The cold-wall infrared heating allows the chamber to heat and cool quickly for during growth synthetic applications and overall experimental duration, thus increasing the throughput of experimental processing. Digital control over the chamber allows the users to recreate and modify previous experiments with high reproducibility.

The initial precursors were chosen for group IV semiconductor chemistry to span C, Si, Ge, and Sn species for alloy and chemistry exploration. In particular, the hydride chemistry (e.g. SiH_4, GeH_4) has been successfully demonstrated in thin film[2] and nanowire synthesis.[3, 4] and was selected as a starting foundation for exploration. Additionally, this hydride chemistry allowed to minimize temperature based energy requirements for future industrial applications when compared to, for example, chloride chemistry.[5, 6] Other complementary precursors were selected to complement the hydrides for specific projects discussed in later chapters.

2.2 Substrate Preparation

Single-side polished Si(111) (El-Cat, CZ) and Ge(111) (MTI Corporation, CZ) substrates were initially etched in 10% HF and rinsed in DI water to remove the native oxide and hydrogen terminate the surface. Subsequent deposition of 20 or 50 nm Au colloid (unconjugated, BBI) was accomplished via immersion of the substrate in the colloid-containing solution with 0.1 M HF for 2 or 5 minutes, respectively, until desired

density of Au was achieved and rinsed in DI water. The negatively charged citrate ion that stabilized gold nanoparticles becomes neutral at lowered pH and allows adhesion to hydrogen terminated substrate.[7, 8] The wafers were then rinsed in 10% HF and DI water before quickly being loaded under vacuum into the reaction chamber.

2.3 Electron Microscopy

Scanning electron microscopy (SEM) was used to image the nanowires on the substrates using Zeiss Ultra-60 field emission scanning electron microscope. By cleaving the (111) wafers along the natural (112) planes, crystal directions based on crystal symmetry were extracted. The confirmation of crystal directions was done with transmission electron microscopy (TEM) with selected area electron diffraction (SAED) or high resolution TEM (HRTEM) and 2-D fast Fourier Transforms (FFT). Elemental analysis was done with energy dispersive spectroscopy (EDX) with the TEM. The TEM samples were prepared by sonication of nanowire covered substrates in methanol, followed by dropcasting the solution onto a lacey carbon grid (Ted Pella). JEOL 100CX 100 kV TEM, FEI Tecnai F20 200 kV, JEOL 2200FS, and FEI Titan S 80 – 300 HRTEM were used these studies.

2.4 X-ray Photoelectron Spectroscopy

2.4.1 Theory

X-ray photoelectron spectroscopy (XPS) is a spectroscopic method where the substrate is irradiated with X-rays and the kinetic energy and count of the emitted electrons is measured. The signal comes from the few nanometers near the surface where

the electrons are able to escape the material, making XPS a surface sensitive technique. The electron binding energy is calculated via the following equation:

$$E_B = h\nu - E_K - E_W, \qquad (2.3)$$

where E_B is the electron binding energy, hv is the energy of the X-ray photons, E_K is the measured kinetic energy, and E_W is the spectrometer work function. The schematic of the XPS energy diagram is shown in Figure 2.4.

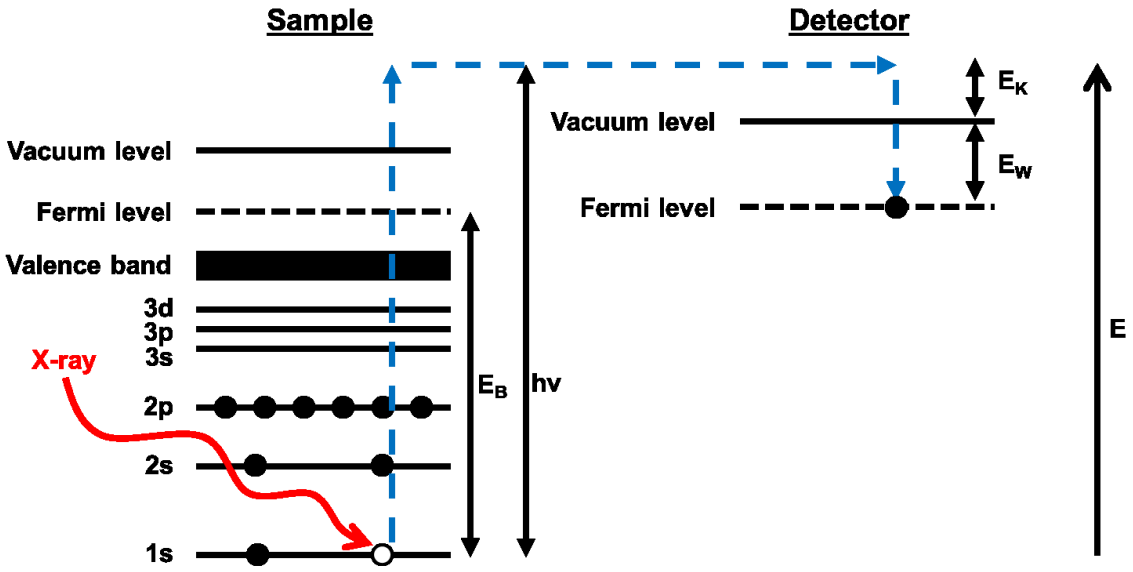

Figure 2.4: Schematic of the basic energy transitions in a typical XPS experiment with labels from Equation 2.3.

The electron binding energies are characteristic to specific elements and their chemical environment.[9] Lower sensitivity to chemical environment allows accurate elemental association and examination of multiple environmental states of each element through peak fitting. For example, higher oxidized states of Ge, due to delocalization of their electron density, would have higher binding energy.

2.4.2 Analysis Methods

Thermo K-Alpha XPS instrument was used to collect XPS data for ex-situ measurement of nanowires on original substrates, utilizing monochromated Al source with double-focusing hemispherical analyzer. Adventitious carbon C 1s peak at 284.5 eV is used to calibrate the spectra for comparison between samples. The spectra are collected with 50 scans at 0.1 eV step size, 50 ms dwell time, and 50 eV pass energy.

2.5 References

1. D. Bour, Z. Yang and C. Chua, *J. Cryst. Growth*, 2008, **310**, 2673-2677.

2. J. Murota, M. Sakuraba and B. Tillack, *Jpn. J. Appl. Phys.*, **45**, 6767.

3. X. Wu, J. S. Kulkarni, G. Collins, N. Petkov, D. Almécija, J. J. Boland, D. Erts and J. D. Holmes, *Chem. Mater.*, 2008, **20**, 5954-5967.

4. J.-E. Yang, C.-B. Jin, C.-J. Kim and M.-H. Jo, *Nano Lett.*, 2006, **6**, 2679-2684.

5. K. K. Lew, L. Pan, E. C. Dickey and J. M. Redwing, *Adv. Mater.*, 2003, **15**, 2073.

6. E. I. Givargizov and N. N. Sheftal, *J. Cryst. Growth*, 1971, **9**, 326-329.

7. J. H. Woodruff, J. B. Ratchford, I. A. Goldthorpe, P. C. McIntyre and C. E. D. Chidsey, *Nano Lett.*, 2007, **7**, 1637-1642.

8. A. J. O'Reilly, C. Francis and N. J. Quitoriano, *J. Colloid Interface Sci.*, 2012, **370**, 46-50.

9. Hollas, J. M., Modern Spectroscopy. 3rd ed.; John Wiley & Sons: Chinchester, 1998

CHAPTER 3

CHEMICAL CONTROL OF SEMICONDUCTOR NANOWIRE KINKING AND SUPERSTRUCTURE

3.1 Introduction

Control of nanowire crystal structure during synthesis, via the vapor-liquid-solid (VLS) growth technique[1] or other method,[2] is required to engineer electrical, optical, and mechanical properties.[3] The recent demonstration of Si nanowire "kinking" superstructures creates new opportunities to accomplish this task and achieve nanoscale devices with novel function. The ability to manipulate nanowire growth orientations could allow to control electronic properties,[4] phonon scattering at kink interfaces,[5] complex out-of-plane electronics,[6, 7] etc. Lastly, understanding the phenomena underlying the kinking mechanisms could in turn allow to avoid deviations from 1-D geometry when is so desired. Lieber and coworkers temporally modulate pressure during the VLS growth of Si and Ge nanowires to yield a kink between two <112> oriented segments at user-defined positions along the nanowire length. While the mechanism underlying this process still requires additional clarification, the ability to rationally select other kink angles would enable additional levels of complexity.

Changes in nanowire crystal growth direction are most commonly observed by modulating global process parameters such as precursor partial pressure or substrate temperature.[6, 8] Kinking from <111> to <112> crystal orientations has been shown to occur at lower temperatures and higher hydride pressures in SiH_4 grown nanowires.[8]

Unfortunately, multiple aspects of nanowire morphology can be impacted with this approach. For example, pressure and temperature changes often lead to the nucleation of small diameter nanowires in both the Si/Au and Ge/Au nanowire/catalyst systems.[9] Unwanted tapering and radial dopant incorporation are also observed in the Ge/Au system when growth temperature is increased.[10-12] Ge nanowire tapering can be reduced by maintaining growth temperatures below 300 °C,[13] but doing so greatly restricts the process window and increases the complexity of Si/Ge heterostructure formation.

The side effects described above complicate superstructure fabrication and motivate the search for more direct and flexible methodologies with which to dictate nanowire crystal structure and kinking. Recent work shows that O_2 can direct Si nanowire kinking at constant temperature and pressure,[14] and modeling suggests that this effect results from changes to solid-vapor interface energetics.[15] In the present work, we show how the introduction of a bifunctional organohydride, methylgermane (MG), to a traditional Ge nanowire growth environment (i.e. GeH_4/H_2) can modulate crystal growth direction and generate kinking superstructures with user-defined segment lengths and a range of angles. In addition, we find that MG creates a passivating layer on the nanowire sidewall, which prevents tapering and significantly expands the process window for Ge nanowire growth from hydride-based precursors.

3.2 Experimental Details

Substrates for nanowire growth are prepared by a gold colloid deposition method on hydrogen-terminated Si (111) substrates (El-Cat, CZ, 3-5 Ω-cm) in a manner similar to that described previously.[13] The native oxide is initially etched with 10% HF for 5 min. Substrates are subsequently dipped into a citrate-stabilized 50 nm gold colloid suspension

(BBI) with 0.1M HF for 5 min. The samples are rinsed in DI water, dried with nitrogen, and immediately transferred to a cold wall rapid thermal processing chemical vapor deposition reactor. A Zeiss Ultra60 scanning electron microscope (SEM), a FEI Tecnai F20 200 kV high resolution transmission electron microscope (HRTEM), and 100kV JEOL 100CX II TEM are used to assess nanowire morphology and crystallography. For HRTEM analysis, nanowires are removed from the growth substrate via sonication in methanol and then drop-cast onto lacey carbon grids (Ted Pella). X-ray photoelectron spectroscopy (XPS) is accomplished with a Thermo K-Alpha instrument equipped with a monochromated Al source and double-focusing hemispherical analyzer. Samples are analyzed as-grown on the Si(111) substrate and binding energies are calibrated using the adventitious carbon C 1s peak at 284.5 eV. All spectra consist of 50 scans acquired with a 50 eV pass energy, 0.1 eV step size, and 50 ms dwell time.

3.3 Results and Discussion

The cross-sectional SEM images shown in Figure 3.1 for Ge nanowire growth with and without MG reveal important morphological differences as a function of temperature. To enable a direct comparison between different process conditions, all samples in Figure 3.1 include an initial nucleation step at 375 °C with 0.44 Torr GeH_4 and 8.81 Torr H_2 for 1 min. For the samples shown in Figures 3.1a and b, this step is followed by an elongation step at the same partial pressures and 375 °C or 475 °C, respectively. While the radial growth rate increases as a function of temperature,[10] nanowires grown with the standard GeH_4/H_2 chemistry always exhibit a <111> crystal orientation. Increasing the partial pressure of GeH_4 by 50% (0.65 Torr) or 100% (0.86

Torr) results in a faster growth rate, but the growth direction always remains the same (Figure 3.2).

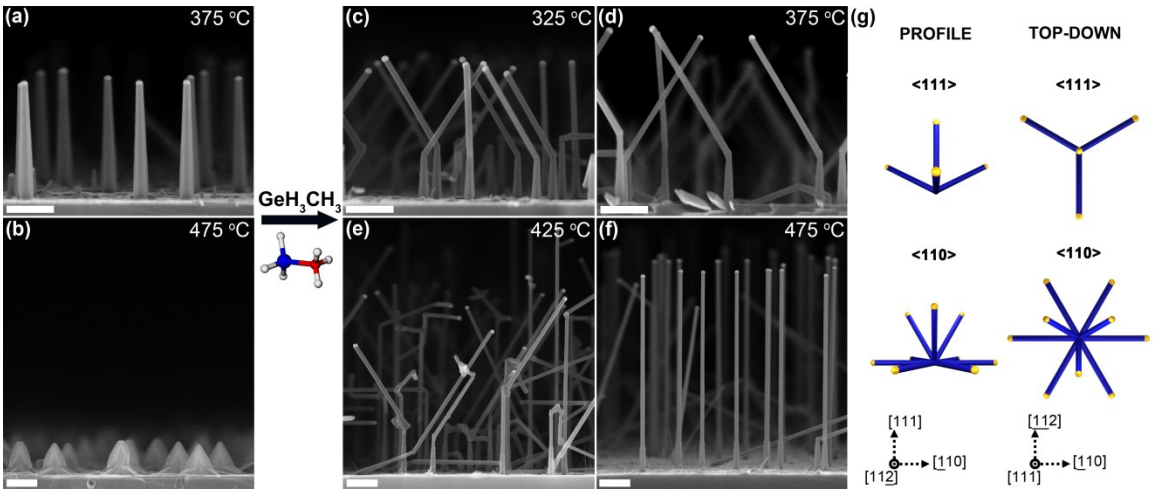

Figure 3.1 SEM images of Ge nanowires grown on Si (111) (a-b) without and (c-f) with GeH_3CH_3. All growth protocols begin with a 1 min nucleation step at 375 °C with 0.44 Torr GeH_4 and 8.81 Torr H_2. The second step consists of (a) 3 min at the same conditions or (b) a ramp to and 1 min growth at 475 °C with the same partial pressures as (a). For the remaining images, the second step takes place at 0.44 Torr GeH_4, 0.21 Torr GeH_3CH_3, and 8.81 Torr H_2 with (c) a ramp to and 3 min growth at 325 °C, (d) a ramp to and 3 min growth at 375 °C, (e) a ramp to and 3 min growth at 425 °C and, (f) a ramp to and 1 min growth at 475 °C. (g) Schematic illustration of various <111> and <110> orientations for comparison with SEM images. The profile schematic is slightly tilted for clarity. All scale bars are 400 nm.

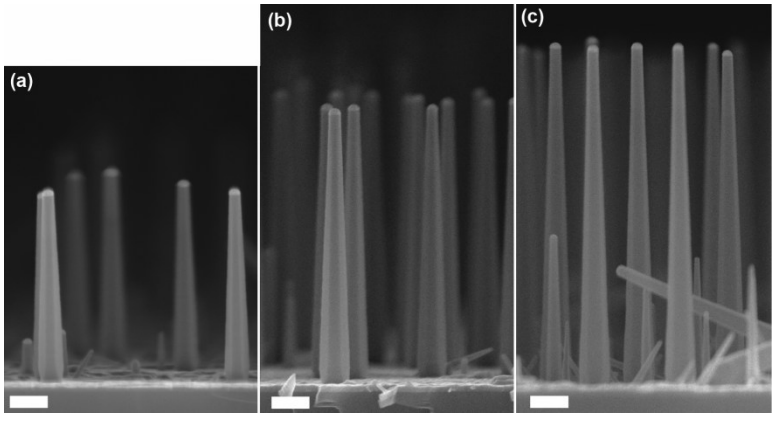

Figure 3.2 SEM images of <111> oriented Ge nanowires grown at 375 °C with 0.44 Torr GeH_4 and 8.81 Torr H_2 for 1 minute, followed by 8.81 Torr H_2 and (a) 0.44, (b) 0.65, and (c) 0.86 Torr GeH_4 for an additional 3 minutes. (a) is the same image as shown Figure 3.1a and is included for comparison. Scale bars, 200 nm.

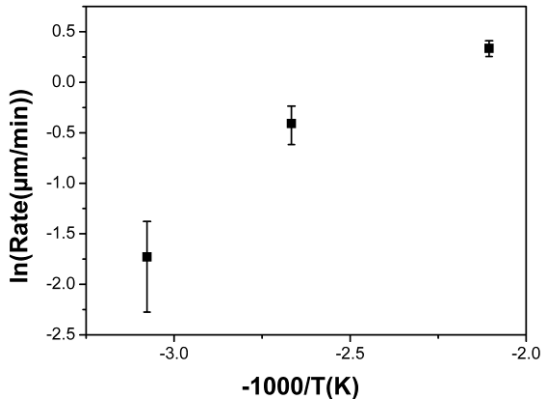

Figure 3.3 Arrhenius plot of Ge nanowire growth rate normal to the substrate for conditions matching Figure 3.1c, d, and f. To eliminate the uncertainty associated with the initial nucleation time (i.e. at the substrate), growth rates were determined by growing two samples at the same conditions for times that differ by 1 min. An accurate growth rate for each temperature is readily calculated by subtracting the length of nanowires from each run.

The elongation step for the samples shown in Figures 3.1d-f occurs at temperatures between 325 °C and 475 °C in the presence of 0.21 Torr MG at the same GeH_4 and H_2 partial pressure. Importantly, the addition of MG leads to a transition from <111> to <110> oriented growth below 425 °C. As illustrated in Figure 3.1g, this initial assignment is made by considering the diamond cubic lattice structure and noting the angle by which nanowires deviate from the vertical. 85% and 77% of the nanowires shown in Figures 3.1c and 3.1d, respectively, transition from <111> to <110> oriented growth upon addition of MG. While uncontrollable kinking is observed with MG at elongation temperatures near 425 °C (Figure 3.1e), kinking ceases and we observe vertically oriented <111> nanowires at 475 °C (Figure 3.1f). 88% of the nanowires in Figure 3.1f remain <111> oriented when MG is added. The growth rates for nanowires in Figures 3.1c, d, and f are 0.18 ± 0.07, 0.67 ± 0.12, and 1.40 ± 0.1 μm/min, respectively (Figure 3.3). Unfortunately, the uncontrolled kinking in Figure 3.1e precludes an accurate determination of axial growth rate and kinking yield. Nanowires grown at 375 °C in the

absence of MG exhibit a hexagonal cross-section as previously reported,[16] but no clear sidewall facets are observed for nanowires exposed to MG.

The change of radial deposition rates with and without MG is striking. As previously reported, conformal deposition is common when utilizing hydride precursors at elevated temperatures.[17] Thermal desorption studies of vacuum-prepared Ge surfaces indicate that surface-bound hydrogen largely desorbs by 375 °C[18] and the presence of free surface sites enables additional precursor adsorption and decomposition. This behavior is exemplified by the extensive tapering of the nanowires shown in Figure 3.1b. On the other hand, MG creates a passivation layer on the nanowire sidewall as evidenced by the elimination of sidewall tapering after its introduction (Figure 3.1c-f).

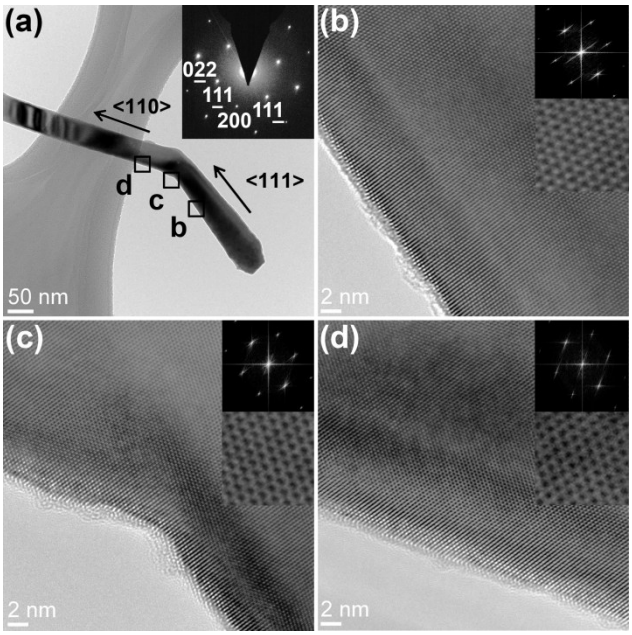

Figure 3.4 HRTEM images along the [011] zone-axis of a representative Ge nanowire grown by the same protocol as used in Figure 3.1d. (a) Low-magnification image of the nanowire with a selected area diffraction pattern inset. High magnification bright field image of the nanowire (b) below, (c) at, and (d) above the <111> to <110> transition. Insets are corresponding FFTs and 300% fringe magnifications.

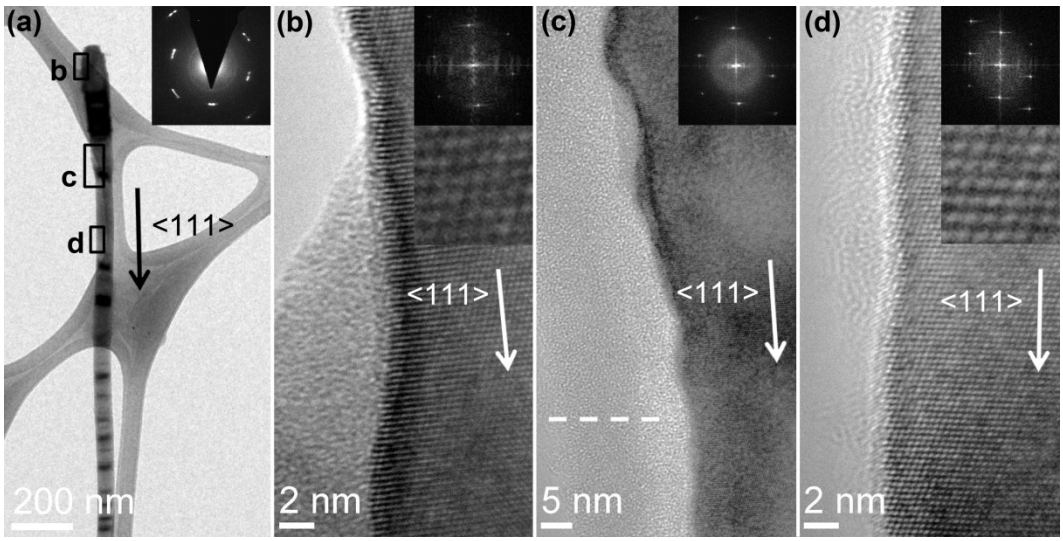

Figure 3.5 HRTEM images along the [011] zone-axis of a representative Ge nanowire grown by the same protocol as used in Figure 3.1f. (a) Low-magnification image of the nanowire with a selected area diffraction pattern inset. High magnification bright field image of the nanowire (b) below, (c) at, and (d) above the point at which MG is added. Insets are corresponding FFTs and 300% fringe magnifications. The dashed line in (b) indicates the transition between rough and smooth sidewalls.

HRTEM images and diffraction patterns of Ge nanowires elongated in the presence of MG at 375 °C (Figure 3.1d) and 475 °C (Figure 3.1f) are shown in Figure 3.4 and Figure 3.5, respectively. The diffraction patterns shown in Figure 3.4 confirm a crystal orientation transition from <111> to <110> upon MG addition. Nanowires remain single crystalline upon MG addition and, as opposed to reports for the Si/Au system,[19] we do not observe twin defects or stacking faults near the kink. In addition, <110> oriented nanowires transition back to the <111> growth direction when MG is removed from the growth environment (Figure 3.6). Figure 3.5 shows that Ge nanowires grown at elevated temperature remain <111> oriented, even in the presence of MG, and tapering is eliminated. The spacing of the {111} lattice fringes corresponds to that of a bulk Ge lattice (0.327 ± 0.005 nm) both before and after the addition of MG, which suggests no

significant C incorporation. Post growth surface oxidation and poorly understood deviations from Vegard's rule for $Ge_{1-x}C_x$ alloys[20] prevent a more precise assessment of C incorporation at this time.

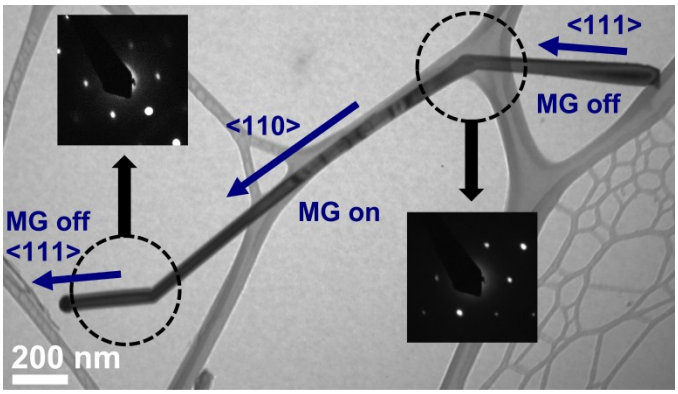

Figure 3.6 Bright field image and SAED pattern insets of a representative twice-kinked Ge nanowire grown for (i) 30 seconds at 375 °C in 0.44 Torr GeH_4 and 8.81 Torr H_2, (ii) followed by a 2 min ramp to 325 °C and growth for 5 minutes in 0.44 Torr GeH_4, 0.21 Torr GeH_3CH_3, and 8.81 Torr H_2, and (iii) an additional growth for 2 minutes with in 0.44 Torr GeH_4 and 8.81 Torr H_2. The growth directions are assigned from the SAED patterns along the [011] zone axis.

Figure 3.7 shows how varying the MG concentration during the elongation step impacts nanowire growth. At 375 °C, nanowire growth rate is first order in MG partial pressure, indicating that Ge–C bond cleavage is taking place and contributing Ge atoms to the nanowire. This occurs despite the strength of the Ge–C bond (~109 kcal mol^{-1}) and general difficulty of depositing Ge thin films with MG alone.[21] The growth of Ge nanowires at 325 °C from MG in the absence of GeH_4 (Figure 3.8) confirms that the Au/Ge eutectic catalyst can accelerate Ge–C decomposition. While complete elimination of carbon residue from nanowire surfaces and/or bulk is unlikely, our data indicates that carbon does not significantly accumulate (Figure 3.4 and Figure 3.5) and reports of Ge thin film deposition using MG support a mechanism whereby excess carbon removal is possible in the form of CH_4.[22]

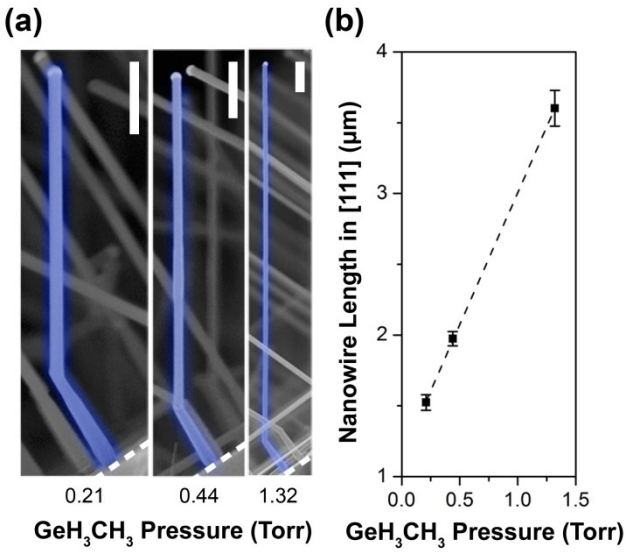

Figure 3.7 Dependence of Ge nanowire growth rate on GeH_3CH_3 partial pressure at 375 °C. (a) SEM images of nanowires grown for 1 min in 0.44 Torr GeH_4 and 8.81 Torr H_2, followed by 3 min in 0.44 Torr GeH_4, GeH_3CH_3 partial pressure as indicated, and 8.81 Torr H_2. The H_2 partial pressure was maintained at 8.81 Torr for all except the 1.32 Torr GeH_3CH_3 case, where it was set at 7.92 Torr, to enable accurate pressure readings. Dashed white lines in each SEM image correspond to the Si(111) surface, which is tilted in these images. A representative nanowire for each partial pressure is falsely colored in blue for clarity. All scale bars are 300 nm. (b) Nanowire length measured normal to the substrate is plotted as a function of GeH_3CH_3 partial pressure. The dashed line is a least squares linear fit of the data.

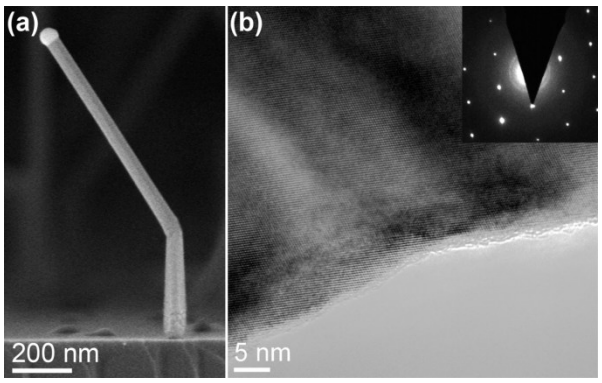

Figure 3.8 (a) SEM image of a representative Ge nanowire grown for 1 minute at 375 °C in 0.44 Torr GeH_4 and 8.81 Torr H_2, followed by ramp to 325 °C and growth for 3 minutes in 0.65 Torr GeH_3CH_3 and 9.03 Torr H_2. Note that no GeH_4 was used during the final 3 minutes. (b) HRTEM bright-field image and SAED inset along a [011] zone axis at the <111> to <110> kink.

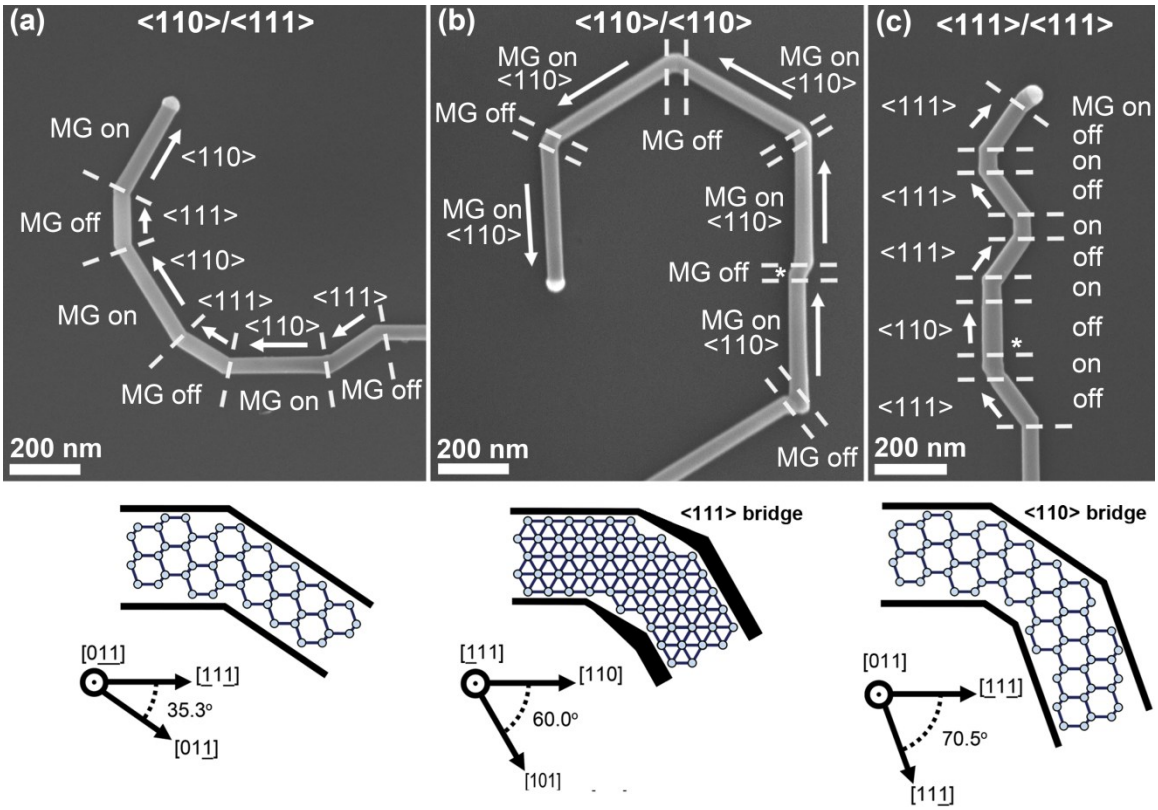

Figure 3.9 Ge nanowire kinking superstructures fabricated at 325 °C by introducing GeH_3CH_3 at user-defined points during VLS growth. Segments without GeH_3CH_3 are grown with 0.44 Torr GeH_4 and 8.81 Torr H_2 while those with GeH_3CH_3 are grown with 0.44 Torr GeH_4, 0.21 Torr MG, and 8.81 Torr H_2. SEM images of (a) <111>/<110>, (b) <110>/<110>, and (c) <111/<111> superstructures where GeH_3CH_3 is cycled on for 1 min and off for 1 min, on for 1.5 min and off for 15 seconds, and on for 10 seconds and off for 1 min, respectively. Dashed lines show where GeH_3CH_3 flow was initiated or terminated. A "*" denotes “defect” locations where transition does not occur as desired. Schematics for each growth direction change is shown below each corresponding superstructure with the smallest deviation angle labeled. As denoted by the bolded sidewalls in the schematic for (b), the diamond cubic lattice dictates that neighboring <110> segments of the <110>/<110> superstructure cannot lie in the same plane. Kinking toward a specific degenerate crystallographic direction (e.g. [1$\underline{1}$0] vs. [110]) within a family of directions (e.g. <110>) is not possible to control at this time.

The MG induced kinking described above can be leveraged to form complex Ge nanowire kinking superstructures with a variety of distinct angles. Figure 3.9 shows representative examples of <111>/<110>, <110>/<110>, and <111>/<111> superstructures fabricated at 325 °C as well as schematic illustrations of each kink type.

Since our TEM imaging of nanowires with single and double kinks (Figures 3.4 and 3.6) confirms MG's ability to modulate growth direction from <111> to <110> and vice versa below 425 °C, we assign the orientation of each superstructure segment based on MG flow (i.e. on or off).

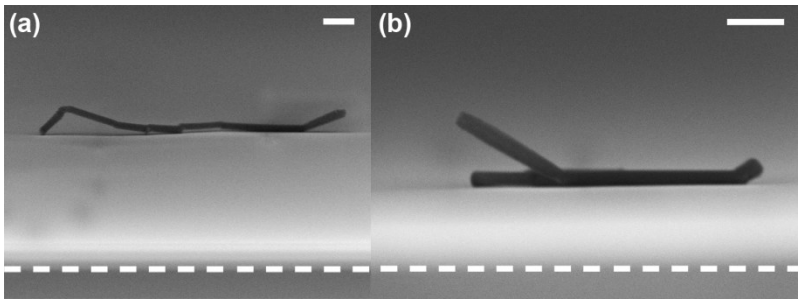

Figure 3.10 Cross-sectional SEM image of two non-planar Ge nanowire superstructures from the same sample as that shown in Figure 3.9b after sonication from the growth substrate and drop-casting onto a Si wafer. The non-coplanarity of the <110> and <111> segments, as expected from the diamond cubic crystal structure of Ge, is clearly visible. The cleaved edge of the wafer is indicated by the dotted line. Scale bars, 200 nm.

It is important to emphasize that the diamond cubic crystal structure dictates that not all <110> and <111> segments can lie in the same plane. Two non-planar nanowires from Figure 3.9b are shown from the side in Figure 3.10. While not shown in Figure 3.9 for clarity in comparison, each superstructure is formed after an initial 1 min nucleation step at 375 °C with 0.44 Torr GeH_4 and 8.81 Torr H_2 followed by <110> oriented growth in the presence of 0.21 Torr MG while cooling to 325 °C for 2 min. The superstructure shown in Figure 3.9a is accomplished with three cycles of 1 min GeH_4/H_2 flow followed by 1 min of MG co-flow (6 min total). Figure 3.9b shows a superstructure consisting of five <110>/<110> transitions, achieved by reducing the GeH_4/H_2 flow segment to 15 sec and increasing the MG co-flow segment time to 1.5 min (8 min 45 sec total). The <111> segments are almost completely eliminated in this situation, while the length of <110>

segments is increased. Figure 3.9c shows a <111>/<111> superstructure with small <110> bridge segments where a zig-zag structure, accomplished with five cycles of GeH_4/H_2 flow for 1 min and MG co-flow for 10 seconds (5 min 50 sec total), is more prevalent.

While these results show that Ge nanowire kinking superstructures with a range of angles and user-defined segments lengths are possible by temporally varying MG exposure, a number of important observations require additional discussion. As indicated by a '*' in Figure 3.9, occasionally nanowires do not transition as desired. Figure 3.9b shows a segment that does not kink to a different <110> direction and Figure 3.9c exhibits a <110> segment when <111> is expected. We attribute these superstructure defects to transients in the triple-phase region and/or local differences in MG concentration that result from the structural complexity of kinked nanowires arranged on the Si(111) substrate. It is also important to note that kinking toward a specific degenerate crystallographic direction (e.g. [110] vs. [1$\underline{1}$0]) is not possible to control at this time. The "handedness" of the nanowires seen in Figure 3.9a and 3.9b is only one of many different superstructure motifs. Figure 3.11 shows random adjacent nanowires from Figure 3.9b as they lay next to each after the drop-casting procedure.

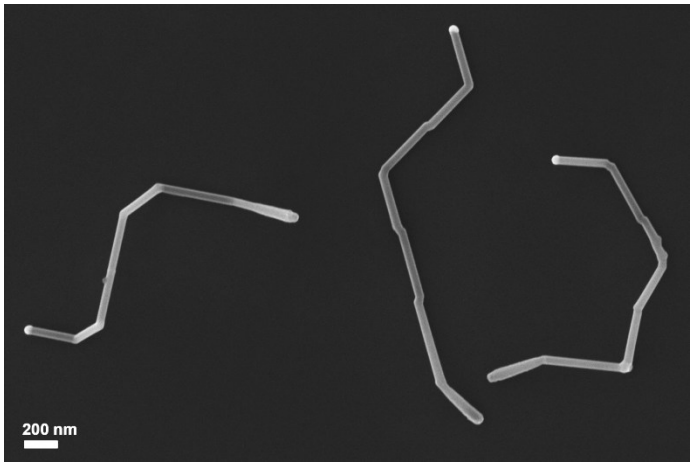

Figure 3.11 SEM image of three Ge nanowire superstructures, from the same sample as that shown in Figure 3.9b, laying side by side after sonication from the growth substrate and drop-casting onto a Si wafer.

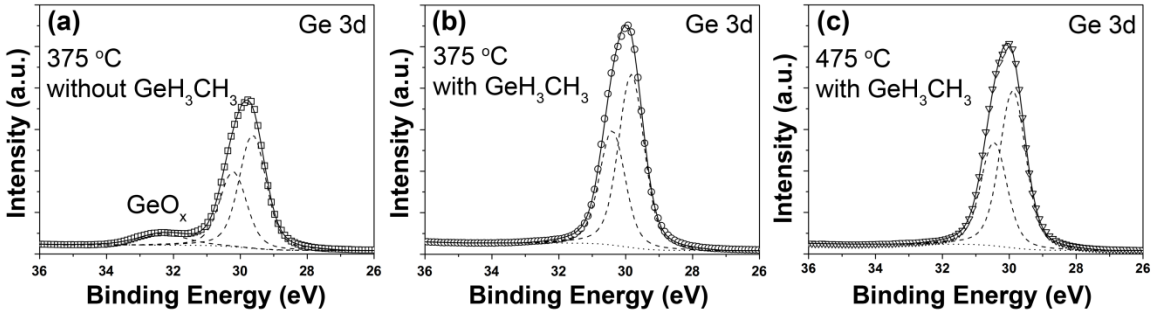

Figure 3.12 XPS of the Ge (3d) peak for Ge nanowires grown (a) with GeH_4/H_2 at 375 °C, (b) with GeH_3CH_3 at 375 °C, and (c) with GeH_3CH_3 at 475 °C after 50 min of exposure to ambient cleanroom air. Recorded data are marked with circles, squares, and triangles respectively. Fitted peaks are shown with dashed lines, baselines are shown with dotted lines, and overall fits are shown with solid lines. The intensity scale is the same for all figures.

Tuning the morphology and crystal structure of nanocrystals via surface chemistry is well known,[23, 24] but has only been sporadically discussed in the context of VLS growth.[14, 25] As shown in Figure 3.12, XPS was utilized to investigate the role of surface passivation on Ge nanowire morphology in the presence of MG. To increase the

photoelectron signal of the nanowires relative to the substrate, samples for XPS analysis were grown for an extended period of time. More specifically, the Ge nanowires in Figure 3.12a were grown without MG for 11 min at 0.44 Torr GeH_4 and 8.81 Torr H_2 at 375 °C. The sample in Figure 3.12b was nucleated at 0.44 Torr GeH_4 and 8.81 Torr H_2 at 375 °C for 3 min, with 0.21 Torr MG added for another 8 min. The sample in Figure 3.12 was nucleated at the same conditions for 1 min, and then ramped to and held for 2 min at 475 °C with 0.21 Torr MG. All samples were exposed to controlled cleanroom air at 70 °F and 38% relative humidity for 50 min prior to introduction into the XPS system. All samples exhibit Ge $3d_{5/2}$ and Ge $3d_{3/2}$ photoelectron peaks near 29.6 eV and 30.2 eV, respectively. Peak fitting of the spin-orbit doublet was accomplished by setting a 3:2 area ratio and equal FWHMs. An additional peak appears +2.7 eV above that for Ge $3d_{5/2}$ only in the case of nanowires grown without MG (Figure 3.12a). Its high binding energy is indicative of surface oxidation,[26] as would be expected for a bare Ge surface exposed to ambient. Our data is not sufficiently resolved to identify specific oxidation states; however, the peak center suggests a Ge^{3+} contribution, analogous to reports for planar Ge substrates[27] as well as nanowires synthesized in solution.[28] Notably, both the kinked (375 °C) and unkinked (475 °C) nanowire samples grown with MG are largely oxide-free. C 1s photoelectron data (not shown) is convoluted by adsorption of adventitious carbon during sample transfer and prevents a more detailed characterization of surface termination. It is important to note that all recipes include a nucleation step without MG, such that a Ge thin film is present on the Si substrate for all samples and this accounts for part of the XPS signal. While the surface chemistry of the Ge-coated substrate is

expected to be nearly identical to the nanowire sidewall, the density, diameter, and length of nanowires indicates that they contribute at least 60% of the photoelectron signal.

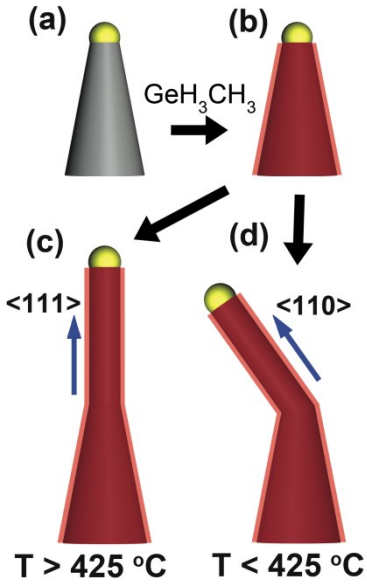

Figure 3.13 Schematic illustration of growth modes as a function of GeH_3CH_3 exposure and temperature. (a) In the absence of GeH_3CH_3, <111> oriented Ge nanowires with tapered sidewalls are observed. (b) Upon addition of GeH_3CH_3 to the growth environment, a robust sidewall coating (red) blocks subsequent conformal deposition for all of the temperatures studied here. (c) At growth temperatures above 425 °C, untapered <111> oriented growth is observed in the presence of GeH_3CH_3. (d) At growth temperatures below 425 °C, untapered <110> oriented growth is observed in the presence of GeH_3CH_3.

These results support the *in-situ* formation of a robust passivating surface layer on the nanowire sidewall, as illustrated in Figure 3.13, which blocks sidewall deposition and prevents tapering. Tapered nanowire growth is observed in the absence of MG because surface hydrogen (from GeH_4) rapidly desorbs from the sidewall (in the form of H_2),[18] thus enabling additional GeH_4 adsorption/decomposition (Figure 3.13a). These open surface sites are subsequently terminated upon exposure to MG (red shell, Figure 3.13b). A comparison of Ge–C (~109 kcal mol^{-1}) and C–H (~105 kcal mol^{-1}) bonds relative to Ge–H (~83 kcal mol^{-1})[29, 30] suggest that MG initially reacts on the nanowire surface via

the $–GeH_3$ group. While a subsequent surface reaction (e.g. decomposition of the $–CH_3$ group) is possible, we do not observe a thick surface coating along the sidewall at any temperature (Figure 3.4 and 3.5) as is seen for some nanowire syntheses.[31] Yet, the oxidation resistance observed for nanowires grown in the presence of MG at both 375 °C and 475 °C (Figure 3.12b and 3.12c) indicates a thin carbon-containing film or residue is likely present and responsible for the observed surface passivation.

MG can also influence nanowire morphology by altering the force balance at the triple-phase line. Although the precise mechanism underlying kinking during VLS growth remains under active debate,[8, 19] our pressure-dependent data (Figure 3.2) indicates that changes to catalyst supersaturation are not solely responsible for <110> oriented growth under the conditions studied here. Similar to other nanoscale systems,[23, 24] we propose that surface chemistry, specifically the lifetime of MG-derived solid-vapor interface moieties (e.g. $–CH_3$) relative to the timescale for bilayer nucleation, governs the <111>/<110> orientation transition. Below 425 °C, the presence of surface adsorbates reduces the surface energy,[32] stabilizes new Ge facets, and drives <110> oriented growth (Figure 3.13d). Recent continuum modeling by Tersoff and coworkers, which shows that small changes to the solid-vapor interface energy are sufficient to cause kinking, supports the proposed mechanism.[15] As the growth temperature is increased above 425 °C, the timescale for nucleation is faster than adsorbate delivery and/or adsorbate decomposition is accelerated. The solid-vapor interface energy is expected to rise in this situation and <111> oriented growth becomes favorable again (Figure 3.13c). Coincidentally with our transition from <110> to <111> oriented growth, temperature programmed desorption studies from planar Ge surfaces show $–CH_3$ groups desorbing above 425 °C and also

decomposing on the surface,[33] further confirming a surface chemical connection to nanowire structure. Although a detailed analysis of the precise surface chemistry requires *in-situ* spectroscopic techniques and is beyond the scope of the present work, such studies are currently underway in our laboratory.

3.4 Conclusions

In conclusion, we can control the crystal growth orientation and prevent tapering of Ge nanowires by introducing MG during VLS growth. This capability was subsequently leveraged to fabricate Ge nanowire kinking superstructures with angles based on combinations of <111> and <110> crystal orientations. Additional work is required to completely eliminate transition "defects" and select a particular kink direction among a set of degenerate crystallographic directions (i.e. [110] vs. [1$\underline{1}$0]). Importantly, the approach described here decouples kinking and tapering from global process parameters, such as temperature and pressure. Sidewall termination also expands the process window for Ge nanowire growth and is expected to simplify the fabrication of Si/Ge heterostructures. This chemistry is also expected to minimize radial dopant gradients and yield synthetic advantages when axially oriented junctions are desired. We anticipate that additional benefits will result from the application of similarly complex chemistries to the growth of this (e.g. Ge) or other nanowire systems (e.g. Si or III-V).

3.5 References

1. T. E. Clark, P. Nimmatoori, K. K. Lew, L. Pan, J. M. Redwing and E. C. Dickey, *Nano Lett.*, 2008, **8**, 1246-1252.

2. T. Hanrath and B. A. Korgel, *Small*, 2005, **1**, 717-721.

3. H. J. Joyce, J. Wong-Leung, Q. Gao, H. H. Tan and C. Jagadish, *Nano Lett.*, 2010, **10**, 908-915.

4. E. Landgraf, W. Rösner, M. Städele, L. Dreeskornfeld, J. Hartwich, F. Hofmann, J. Kretz, T. Lutz, R. J. Luyken, T. Schulz, M. Specht and L. Risch, *Solid-State Electron.*, 2006, **50**, 38-43.

5. J.-S. Heron, C. Bera, T. Fournier, N. Mingo and O. Bourgeois, *Phys. Rev. B*, 2010, **82**, 155458.

6. B. Tian, P. Xie, T. J. Kempa, D. C. Bell and C. M. Lieber, *Nat Nano*, 2009, **4**, 824-829.

7. B. Tian, T. Cohen-Karni, Q. Qing, X. Duan, P. Xie and C. M. Lieber, *Science*, 2010, **329**, 830-834.

8. P. Madras, E. Dailey and J. Drucker, *Nano Lett.*, 2009, **9**, 3826-3830.

9. E. Dailey and J. Drucker, *J. Appl. Phys.*, 2009, **105**, 064317.

10. H. Jagannathan, M. Deal, Y. Nishi, J. Woodruff, C. Chidsey and P. C. McIntyre, *J. Appl. Phys.*, 2006, **100**.

11. D. E. Perea, E. R. Hernesath, E. J. Schwalbach, J. L. Lensch-Falk, P. W. Voorhees and L. J. Lauhon, *Nat. Nanotechnol.*, 2009, **4**, 315-319.

12. P. Xie, Y. J. Hu, Y. Fang, J. L. Huang and C. M. Lieber, *Proc. Natl. Acad. Sci. U.S.A.*, 2009, **106**, 15254-15258.

13. J. H. Woodruff, J. B. Ratchford, I. A. Goldthorpe, P. C. McIntyre and C. E. D. Chidsey, *Nano Lett.*, 2007, **7**, 1637-1642.

14. F. M. Ross, *Rep. Prog. Phys.*, 2010, **73**, 114501.

15. K. W. Schwarz, J. Tersoff, S. Kodambaka, Y. C. Chou and F. M. Ross, *Phys. Rev. Lett.*, 2011, **107**, 265502.

16. H. Adhikari, A. F. Marshall, C. E. D. Chidsey and P. C. McIntyre, *Nano Lett.*, 2006, **6**, 318-323.

17. C.-B. Jin, J.-E. Yang and M.-H. Jo, *Appl. Phys. Lett.*, 2006, **88**, 193105-193103.

18. J. Y. Lee, J. Y. Maeng, A. Kim, Y. E. Cho and S. Kim, *J. Chem. Phys.*, 2003, **118**, 1929-1936.

19. S. A. Dayeh, J. Wang, N. Li, J. Y. Huang, A. V. Gin and S. T. Picraux, *Nano Lett.*, 2011, **11**, 4200-4206.

20. W. Li, I. Shah, D. Guerin, J. G. Chen and H. Hwu, *J. Vac. Sci. Technol., A*, 2001, **19**, 2617-2621.

21. M. Todd, J. Kouvetakis and D. J. Smith, *Appl. Phys. Lett.*, 1996, **68**, 2407-2409.

22. Y. Y. Fang, J. Tolle, J. Tice, A. V. G. Chizmeshya, J. Kouvetakis, V. R. D'Costa and J. Menéndez, *Chem. Mater.*, 2007, **19**, 5910-5925.

23. J. Huang, M. V. Kovalenko and D. V. Talapin, *J. Am. Chem. Soc.*, 2010, **132**, 15866-15868.

24. Y. Yin and A. P. Alivisatos, *Nature*, 2005, **437**, 664-670.

25. O. Salehzadeh and S. P. Watkins, *Nanotechnology*, 2011, **22**, 165603.

26. D. Schmeisser, R. D. Schnell, A. Bogen, F. J. Himpsel, D. Rieger, G. Landgren and J. F. Morar, *Surf. Sci.*, 1986, **172**, 455-465.

27. D. Knapp, B. S. Brunschwig and N. S. Lewis, *J. Phys. Chem. C*, 2010, **114**, 12300-12307.

28. T. Hanrath and B. A. Korgel, *J. Am. Chem. Soc.*, 2004, **126**, 15466-15472.

29. S. Chakrabarti and K. K. Das, *J. Mol. Spectrosc.*, 2008, **252**, 160-168.

30. K. D. Dobbs and W. J. Hehre, *Organometallics*, 1986, **5**, 2057-2061.

31. V. Dřínek, J. Šubrt, M. Klementová and R. Fajgar, *J. Anal. Appl. Pyrolysis*, 2010, **89**, 255-260.

32. A. A. Stekolnikov, J. Furthmüller and F. Bechstedt, *Phys. Rev. B*, 2002, **65**, 115318.

33. H. Ishii, Y. Takahashi and K. Fujinaga, *J. Electrochem. Soc.*, 1995, **142**, 1952-1956.

CHAPTER 4

SURFACE-CHEMISTRY CONTROLLED DIAMETER-MODULATED SEMICONDUCTOR NANOWIRES AND SUPERSTRUCTURES

4.1 Introduction

The use of semiconductor nanowires as active components in next generation devices is predicated on an ability to manipulate their physical properties via morphology, composition, and/or crystal structure engineering.[1-6] To date, the vast majority of studies have relied upon nanowires with a constant diameter. However, diameter-modulated superstructures, where diameter is rationally varied as a function of axial position, present a largely unexplored opportunity to engineer nanowire function with spatial and spectral specificity. For example, the optoelectronic properties of nanowires that are quantum-confined in the radial direction could be spatially tuned by adjusting diameter along the nanowire longitudinal axis.[7, 8] Diameter-modulation also presents a method to spectrally engineer phonon scattering and increase the thermoelectric figure of merit.[9, 10] Furthermore, the intimate relationship between photon scattering and nanostructure geometry suggests new routes to highly customizable light trapping materials.[11, 12]

The vapor-liquid-solid (VLS) technique is the most common bottom-up semiconductor nanowire synthesis method.[13-15] Semiconductor atoms delivered from impinging precursor gases (e.g. GeH_4) collect in a metal-semiconductor alloy (e.g. Au-

Ge) catalyst sitting atop a crystalline semiconductor nanowire (e.g. Ge). Nanowire elongation occurs via a repeated sequence of catalyst supersaturation, nucleation near the triple-phase line (i.e. where the vapor, liquid, and solid meet), and step flow across the nanowire-liquid interface.[16, 17] Nanowire diameter is generally fixed via selection of catalyst size prior to growth, but a handful of options are available for modest diameter tuning *in-situ*. For example, growth temperature effects semiconductor atom solubility in the catalyst and thus nanowire diameter.[17, 18] Unfortunately, such changes to global process parameters influence multiple aspects of nanowire synthesis.[19-21] Even if these effects can be managed, the window for stable nanowire growth[22] will limit the extent of diameter modulation. While changes to nanowire polytype[23] or composition[24, 25] can also influence diameter, an ideal synthetic method would offer independent control of diameter and crystal structure.

Here, we demonstrate that Ge nanowire surface chemistry can be controlled via the addition of tetramethyltin (TMT) to a standard hydride synthesis environment (i.e. GeH_4/H_2). This "molecular resist" blocks radial deposition, which provides a general method to adjust diameter *in-situ* and opens the door to diameter-modulated superstructures with nanoscale periodicities. The *in-situ* alloying of Sn atoms with the catalyst permits tuning of axial growth rate, and thus superstructure dimensions, without unnecessarily doping the nanowire. Recent reports, particularly the use of $C_2H_2/HCl/GeH_4$[26] and O_2/GeH_4[27] for Ge nanowire growth, show that alternative chemistries also influence sidewall deposition rates. However, the C_2H_2 chemistry requires elevated temperatures, which accelerates axial growth rate and limits the proximity of diameter-modulated regions. Furthermore, both approaches create a carbon

or oxide shell, respectively, at the catalyst growth-front only and do not significantly impact the exposed sidewalls far from the droplet. A direct approach to blocking radial deposition along the entire nanowire is presented in this work, making it possible to "lock-in" the previously formed 3-D nanowire sidewall shape and dictate structure segment by segment.

4.2 Experimental Details

Single-side polished Si(111) (El-Cat, CZ, 3-5 Ω·cm) and Ge(111) (MTI Corporation, CZ, 42-64 Ω·cm) substrates were initially etched in 10% HF to remove the native oxide. Subsequent deposition of 20 or 50 nm Au colloid (BBI) was accomplished via immersion of the substrate in the colloid-containing solution, to which 0.1M HF had been added.[28] The samples were rinsed in 10% HF and deionized water (DI) water immediately prior to placement in the reactor for nanowire growth. TMT is heated to 30 °C and delivered by bubbling with Ar. Nanowire morphology and crystal structure were analyzed with a Zeiss Ultra60 scanning electron microscope (SEM) and a FEI Tecnai F20 200 kV transmission electron microscope (TEM) equipped with an energy-dispersive X-ray (EDX) spectrometer. As-synthesized nanowire arrays were imaged with SEM without further preparation.

4.3 Results and Discussion

4.3.1 Structural Changes from TMT

Figure 4.1 shows cross-sectional SEM images of epitaxial Ge nanowires grown at 375 °C with 50 nm Au colloid on Si(111). Nanowire growth occurs under two standard flow conditions: without and with TMT. The condition "TMT-OFF" refers to 25 sccm

GeH_4, 500 sccm H_2, and 9.25 Torr total pressure, whereas "TMT-ON" refers to 25 sccm GeH_4, 500 sccm H_2, 20 sccm Ar bubbled through TMT, and 9.25 Torr total pressure.

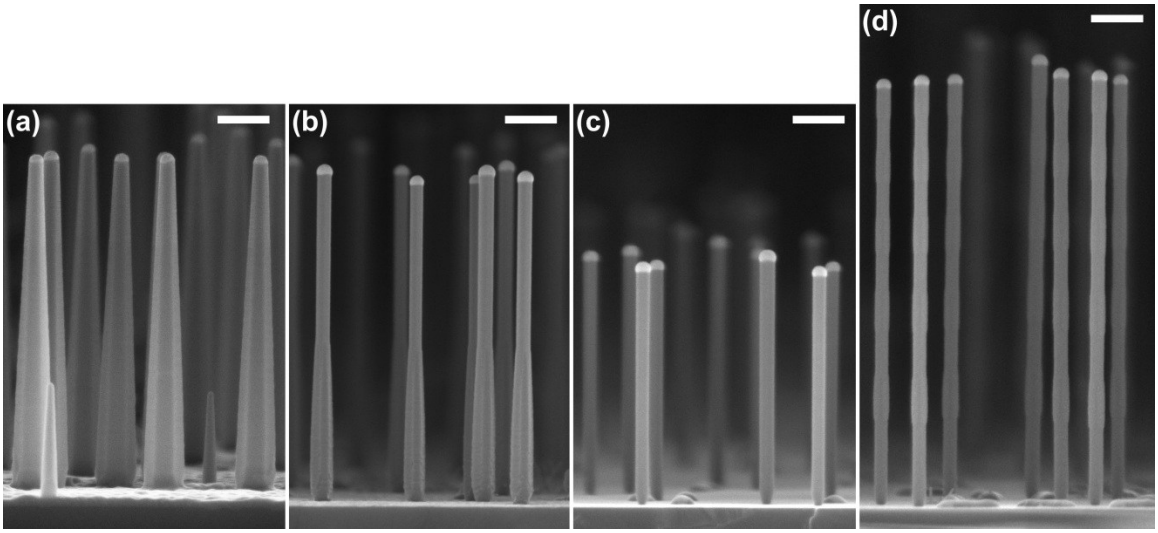

Figure 4.1 SEM images of Ge nanowires grown at 375 °C, 9.25 Torr total pressure, 50 sccm GeH_4, and 500 sccm H_2 (a) without TMT for 5 min, (b) without TMT for 2 min followed by 3 min with 20 sccm Ar bubbled through TMT, (c) with 20 sccm Ar bubbled through TMT for 5 min. (d) Diameter modulation is accomplished by modulating TMT flow on and off at 1 minute intervals a total of 5 times. Scale bars, 200 nm.

Figure 4.1a shows a representative image of nanowire growth with the condition "TMT-OFF". The clear tapering is a common structural motif for Ge nanowires grown at substrate temperatures above 300 °C.[19] The nanowires shown in Figure 4.1b were grown at condition "TMT-OFF" for 2 minutes followed by condition "TMT-ON" for 3 minutes. The addition of TMT immediately eliminates nanowire tapering. A comparison of Figure 4.1a and Figure 4.1b further reveals that the tapering in the lower portion of Figure 4.1b does not increase after the addition of TMT. As shown in Figure 4.1c, no tapering is observed when the entire nanowire is grown with condition "TMT-ON." Whereas tapering becomes significant above 300 °C for the classic GeH_4/H_2 chemistry, temperatures in excess of 400 °C are required with TMT. This expansion of the process

window for taper-free Ge nanowire growth offers important benefits for controlling dopant incorporation[26, 29] and fabricating abrupt heterostructures.[30] The clear changes in nanowire growth rate as a function of TMT delivery time are addressed in detail below.

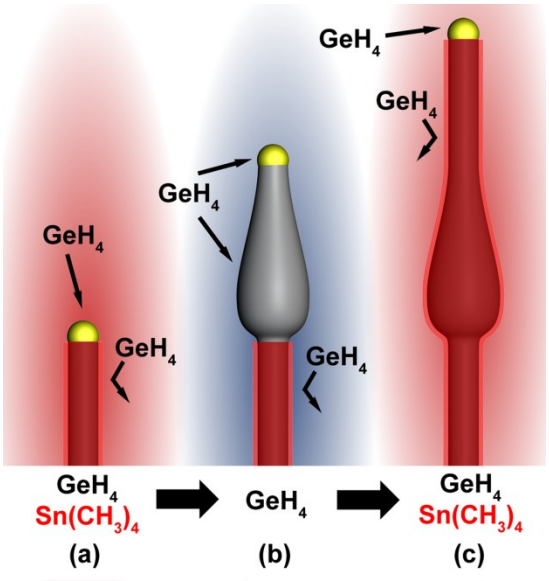

Figure 4.2 Schematic of diameter modulated Ge nanowire synthesis. The exposed Ge nanowire surface is shown in gray and the transparent red shell represents the surface termination that results from TMT adsorption. (a) A nanowire with uniform diameter is grown in the presence of GeH_4 and TMT (i.e. "TMT-ON" conditions). TMT decomposition on the sidewall creates a passivating layer that eliminates radial deposition and tapering. (b) Growth with only GeH_4 (i.e. "TMT-OFF" conditions) enables radials deposition initially only on newly formed sections of the nanowire. (c) Reinitiation of TMT co-flow (i.e. "TMT-ON" conditions) terminates the recently formed sidewall. A repeated sequence of these basic steps yields diameter-modulated superstructures.

We accomplish diameter-modulation with sub-200 nm periodicity by allowing and then suppressing radial growth in the absence and presence of TMT, respectively. The nanowires shown in Figure 4.1d were synthesized with five cycles, each consisting of 1 min "TMT-ON" and 1 min "TMT-OFF." The diameter-modulation process is schematically illustrated in Figure 4.2. It is important to note that TMT adsorbs directly on all exposed nanowire sidewalls. Cessation of TMT flow reinitiates radial deposition

on newly formed portions of the nanowire, but the stability of the previously created surface layer "locks-in" the diameter on lower sections.

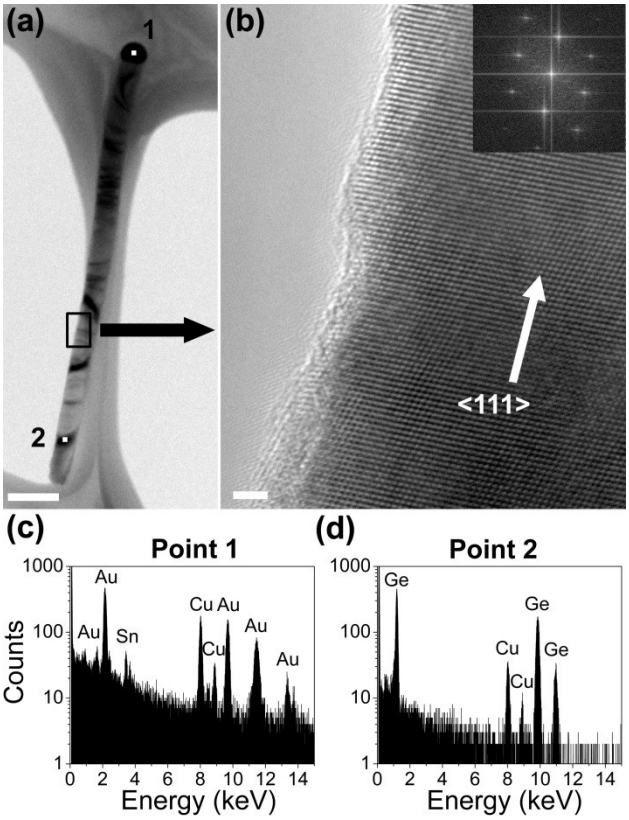

Figure 4.3 Bright field TEM images and EDX spectra of a representative Ge nanowire synthesized under "TMT-ON" conditions at 400 °C, 9.25 Torr total pressure, 50 sccm GeH_4, 500 sccm H_2, and 20 sccm Ar bubbled through TMT. (a) Low magnification image of the nanowire. Scale bar, 100 nm. (b) High resolution image and corresponding FFT inset of the area delineated by the box in (a). Scale bar, 2 nm. EDX spectra acquired (c) at the center of the catalyst droplet and (d) near the nanowire base. The Cu signal results from the TEM grid.

The mechanism by which TMT limits radial deposition deserves additional discussion. In the absence of TMT, H_2 desorption[31, 32] opens surface sites for subsequent GeH_4 adsorption and decomposition. This behavior, which is commonplace for traditional thin film deposition, leads to the sidewall tapering often observed during Ge nanowire growth. We propose that TMT delivers surface species directly to the nanowire

sidewall that prevent subsequent GeH_4 decomposition, even above the H_2 desorption temperature. The weakness of the Sn–C bond (2.8 eV)[33] suggests that the initial decomposition products are Sn and $–CH_3$. A comparison of the Ge–C (4.7 eV)[34] and Ge–H (3.6 eV)[35] bond strengths, in addition to prior evidence from temperature programmed desorption studies,[36] suggest that $–CH_3$ moieties exhibit reasonable lifetimes under our nanowire growth conditions. While CH_4 desorption may occur in the highly reducing GeH_4 environment,[37] it is expected to be less rapid than H_2 desorption. A recent report of Ge nanowire synthesis via vapor-phase transport also indicates that Sn co-delivered to, and presumably adsorbed on the sidewall of, the nanowire can reduce the rate of radial deposition.[38] Therefore, Sn and $–CH_3$ may be simultaneously responsible for the diameter control observed here. Additional studies are currently underway in our laboratory to determine the identity of the surface passivating species.

High-resolution TEM imaging and EDX spectroscopy provide additional insight into the role of Sn during Ge nanowire growth under "TMT-ON" conditions. The clear (111) lattice fringes and corroborating Fast Fourier Transform (FFT) inset in Figure 4.3a,b shows that these nanowires are single-crystalline and retain a diamond cubic structure. Figure 4.3c reveals that Sn alloys with the Au catalyst and Figure 4.3d shows that the sidewall Sn concentration is undetectable (< 1-2%). Prior studies show that the solubility of Sn in bulk Ge is on the order of 1% at our growth temperatures,[39, 40] a value that lies at the edge of our ability to detect its presence with EDX. A more detailed chemical analysis, similar to dopant incorporation studies,[29] should be performed via atom-probe tomography for spatial resolution (for differentiating between nanowire and near-surface composition) and sensitivity necessary to conclude on nanowire composition

in future studies. While Sn does not strongly influence the resistivity or minority carrier lifetime of bulk Ge, even at large concentrations,[39] we plan to undertake transport measurements to assess its impact in VLS-grown material. Furthermore, we do not observe significant amorphous shells, carbon or otherwise, even though each TMT molecule delivers four carbon atoms to the nanowire sidewall. These data suggest that the surface layer generated by TMT is either self-passivating or the nanowire growth environment removes excess surface species from the sidewall.

4.3.2 Kinetic Study of the TMT Effect

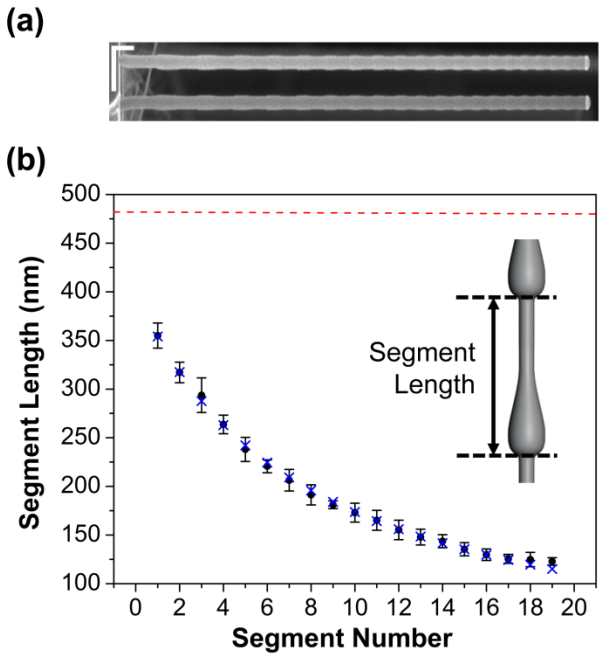

Figure 4.4 (a) SEM image of diameter-modulated nanowires grown with 20 cycles of 1 min "TMT-ON" and 1 min "TMT-OFF" at 375 ^{o}C. Scale bars, 200 nm. The radial scale has been stretched 2x for clarity. (b) Corresponding plot of average nanowire segment length vs. segment number collected from 10 representative diameter-modulated nanowires. Experimental data is shown as black circles and error bars indicate the standard deviation of segment length. The red dashed line indicates Ge nanowire growth rate without TMT (i.e. no Sn alloying). An empirical fit of segment length, as determined from the modified second-order rate law discussed in the text, is shown as blue crosses. Inset: schematic that illustrates how segment length is measured.

The observed changes to nanowire length as a function of TMT exposure time (Figure 4.1) in conjunction with EDX data (Figure 4.3) indicate that TMT alloying with the catalyst reduces the axial growth rate. We investigated the change of growth rate upon *in-situ* Sn catalyst alloying by periodically modulating TMT delivery with 20 repeated cycles of 1 min "TMT-ON" and 1 min "TMT-OFF" at 375 °C. Figure 4.4a shows representative nanowires that result from this process. The radial scale bar is intentionally stretched 2x relative to the axial scale bar to improve clarity. Figure 4.4b shows average segment length plotted as a function of elapsed segment number. Segment lengths are measured as shown in the Figure 4.4b inset and segments are numbered starting from the substrate. Average segment length clearly decreases as the growth continues.

A simple kinetic rate law is proposed to empirically describe the observed growth rate reduction as a function of Sn incorporation in the catalyst. The present data does not fit first-order kinetics as previously reported for Ge nanowire growth with a pure Au catalyst (i.e. no Sn alloying).[41] Thus, we use a second-order rate expression with an adjustable parameter that reflects the impact of Sn alloying on the concentration of catalyst "active sites":

$$r = k\,\theta_{active}\,P_{GeH_4} \qquad (4.1)$$

where k is the rate constant, θ_{active} is the concentration of active sites equivalent on the catalyst, and P_{GeH4} is the partial pressure of GeH_4. Sn alloying of the catalyst is incorporated into the rate law by assuming that it reduces the concentration of Au active sites. In other words, Sn atoms are treated as catalytically inactive and only serve to dilute the catalytically active Au atoms. In this case, the rate law becomes:

$$r = k \frac{n_{Au}}{n_{Au} + n_{Sn}} P_{GeH_4} \qquad (4.2)$$

where n_{Au} is moles of Au, n_{Sn} is moles of Sn, and the remaining variables are the same as introduced above. Dividing the numerator and denominator by n_{Au} and expressing the ratio of moles Sn to moles Au as a function of TMT exposure time:

$$\frac{n_{Sn}}{n_{Au}} = \frac{t_{TMT} F_{Sn}}{n_{Au}} = \frac{t_{TMT}}{\tau}, \qquad (4.3)$$

where t_{TMT} is the TMT exposure time, F_{Sn} is the molar delivery rate of Sn, and τ is an adjustable lumped parameter, yields the final rate law:

$$r = k \frac{1}{1 + t_{TMT}/\tau} P_{GeH_4} \qquad (4.4)$$

The rate constant is determined from measurements of Ge nanowire growth rate using a pure Au catalyst (i.e. $t_{TMT} = 0$). Nanowire arrays grown for 5, 8, and 11 min at 0.44 Torr GeH_4 and 8.81 Torr H_2 exhibit lengths of 1.33 ± 0.02, 2.08 ± 0.02, and 2.81 ± 0.02 μm, respectively. From this data, the rate constant is determined to be k = 0.56 μm min^{-1} $Torr^{-1}$ and is in agreement with previous studies of GeH_4 nanowire synthesis.[41]

To determine the value of P_{GeH4} for Equation 4.4, we require a value for the TMT partial pressure under our bubbling conditions. The Antoine parameters for TMT are estimated from thermodynamic data (A = 7.571, B = 1632, C = -3.320) and yield a vapor pressure of 135 Torr at 30 °C.[42] Assuming equilibrium above the bubbler and pure Ar at the bubbler inlet, a mass balance yields a TMT flow rate of 7 sccm. Thus, we find that the partial pressures are 0.42 Torr GeH_4, 0.12 Torr TMT, 0.33 Torr Ar, and 8.37 Torr H_2 under "TMT-ON" conditions.

It is important to note that changes to nanowire growth rate do not occur continuously because TMT is pulsed on (i.e. "TMT-ON" conditions) and off (i.e. "TMT-OFF" conditions) during the experiment shown in Figure 4.4. Thus, we determine τ via the following procedure:

1. Calculate growth rate from the rate law at 0.1 min time intervals, accounting for segments that do and do not include TMT flow (Figure 4.5a).
2. Segment length as a function of segment number is then determined from this data (Figure 4.5b).
3. Calculated (Figure 4.5b) and experimentally determined segment lengths (Figure 4.4b) are compared and the difference is minimized by varying τ and $t_{TMT,0}$ with a standard least squares algorithm.

Since the substrate is sometimes ramped to the growth temperature in TMT flow, the variable $t_{TMT,0}$ is included to account for the quantity of Sn in the droplet upon reaching the setpoint (i.e. 375 °C). For Figure 4.4b, we extract τ = 6.4 min and $t_{TMT,0}$ = 1.1 min.

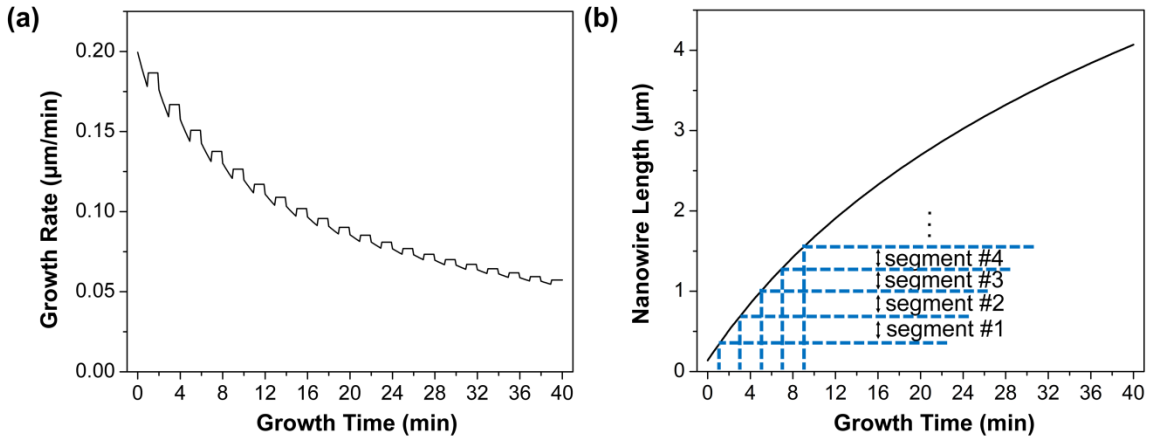

Figure 4.5 (a) Plot of calculated growth rate vs. growth time. (b) Plot of calculated nanowire length vs. growth time. Segment lengths are determined, as shown with blue dashed lines, after each 2 min "TMT-ON" and "TMT-OFF" interval and compared to the experimental data shown in Figure 4.4b via least squares minimization to determine the parameters τ and $t_{TMT,0}$.

As shown in Table 4.1, the fitted parameters from this method also predict the final length of the nanowires shown in Figure 4.1. We note that $t_{TMT,0}$ = 0 min for Figure 4.1a and figure 4.1b since the substrate temperature was ramped to 375 °C in GeH_4 only.

Table 4.1 Comparison of experimental and predicted nanowire lengths from Figure 4.1.

	$t_{TMT,0}$	Length at t = 0	Predicted Nanowire Length	Experimental Nanowire Length
	min	μm	μm	μm
Figure 4.1a	0	0.10	1.33	1.36
Figure 4.1b	0	0.10	1.19	1.25
Figure 4.1c	1.1	0.14	0.91	0.90
Figure 4.1d	1.1	0.14	1.68	1.67

This model yields an excellent empirical fit to our data, as shown with the blue crosses in Figure 4.4b. As summarized in Table 4.1, the same equation also predicts the final lengths of the nanowires shown in Figure 4.1. The need for a plasma discharge to synthesize Si nanowires with SiH_4 and a pure Sn catalyst[43, 44] suggests that Sn reduces the hydride decomposition rate specifically. The precise volume or area of the dilution effect is convoluted with unknown sticking coefficient and delivery rate, requiring further study.

4.3.3 User-Defined Diameter-Modulated Superstructures

We combine this new knowledge of sidewall termination and Sn accumulation in the catalyst to demonstrate user-programmable diameter-modulated superstructures as shown in Figure 4.6. Here, nanowire growth occurs with 20 nm Au colloid on a Ge(111) substrate at 350 °C under three distinct flow conditions labeled as follows: (1) “G” refers to 15 sccm GeH_4 and 110 sccm H_2 at 2.2 Torr total pressure (i.e. GeH_4 only), (2) “T”

refers to 20 sccm Ar bubbled through TMT and 105 sccm H_2 at 2.2 Torr total pressure (i.e. TMT only), and (3) "G+T" refers to 15 sccm GeH_4, 20 sccm Ar bubbled through TMT, and 90 sccm H_2 at 2.2 Torr total pressure (i.e. a co-flow of GeH_4 and TMT). Superstructure uniformity is excellent throughout the array as seen in Figure 4.7. Figure 4.6a shows four diameter-modulated sections created by alternating between "G" and "T" conditions. This protocol, where GeH_4 and TMT are never introduced simultaneously, demonstrates that the surface termination step can be completely separated from axial elongation. We also note a slight reduction of growth rate, as expected, after each "T" step (*vida supra*).

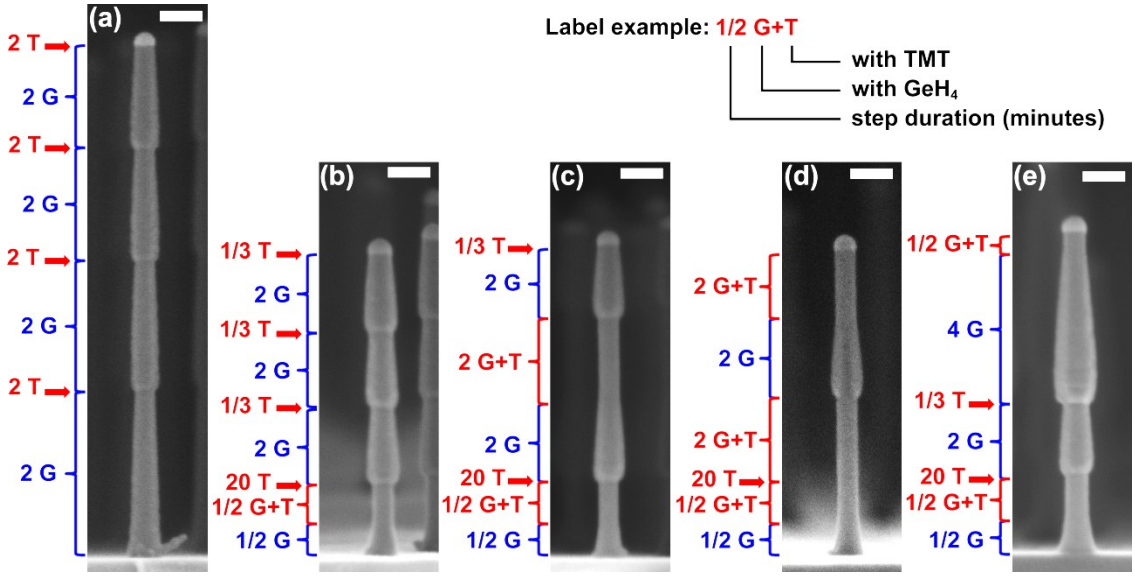

Figure 4.6 User-programmable diameter-modulated Ge nanowire superstructures fabricated from 20 nm Au colloid on a Ge(111) wafer via combinations of different flow conditions at 350 °C. The sequence of growth conditions utilized for each superstructure is shown to the left of each image. "G" refers to 15 sccm GeH_4 and 110 sccm H_2 at 2.2 Torr total pressure (i.e. GeH_4 only), "T" refers to 20 sccm Ar bubbled through TMT and 105 sccm H_2 at 2.2 Torr total pressure (i.e. TMT only), and (3) "G+T" refers to 15 sccm GeH_4, 20 sccm Ar bubbled through TMT, and 90 sccm H_2 at 2.2 Torr total pressure (i.e. co-flow of GeH_4 and TMT). The number preceding each flow designation represents the time in minutes that each condition was applied. Scale bars, 50 nm.

Figure 4.6b shows that sub-100 nm periodicity at same growth times is possible by initially adding a significant quantity of Sn to the catalyst. This capability underscores the usefulness of TMT as a route for decoupling axial and radial growth rates. To unambiguously show that the position of each diameter-modulation is user-selectable, Figure 4.6c shows two diameter expansions separated by a section with uniform diameter. The inverse of this structure, where two sections with uniform diameter straddle a single diameter-modulated region, is displayed in Figure 4.6d. Finally, Figure 4.6e shows the result from a single diameter modulation followed by extended growth in the absence of TMT, demonstrating the flexibility in the tapering dimensions and locations.

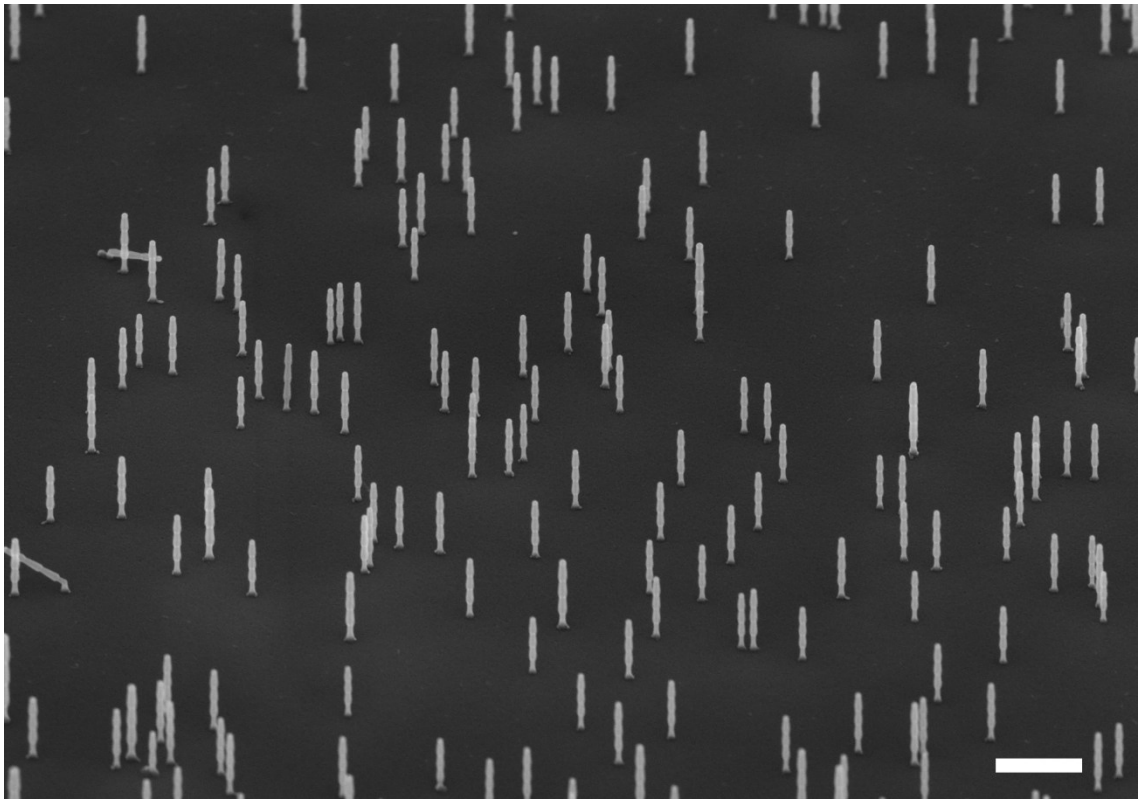

Figure 4.7 SEM image of the diameter-modulated superstructure array from Figure 4.6b observed at a 45° inclined angle. Scale bar, 400 nm.

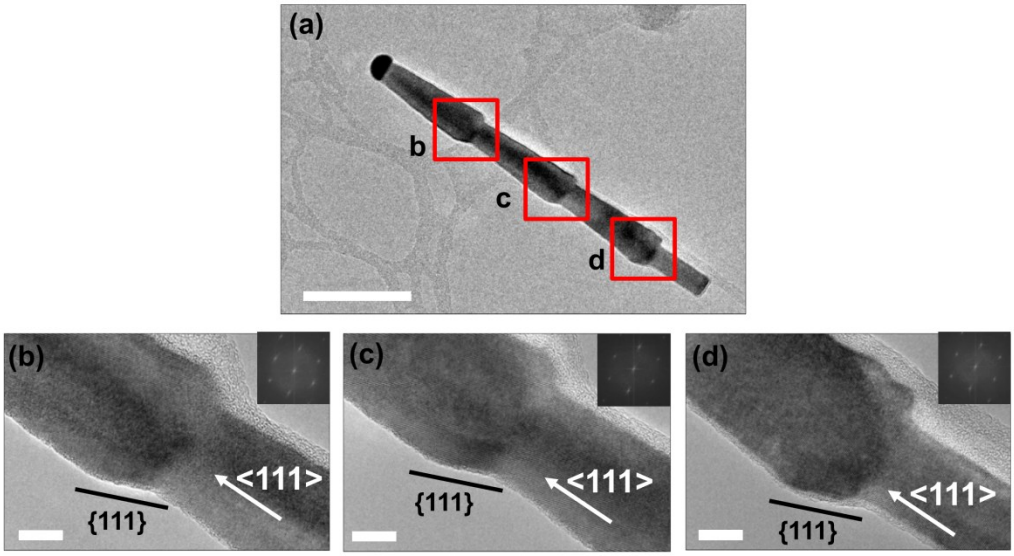

Figure 4.8 Bright field TEM images of a representative Ge nanowire superstructure from Figure 4.6b from [110] zone axis. (a) Low magnification image of the nanowire with labels for high resolution images in b-d. Scale bar, 100 nm. (b-d) High resolution images and corresponding FFT inset of the area delineated by the boxes in (a). Scale bars, 10 nm.

Figure 4.8 shows HRTEM of a representative nanowire superstructure from Figure 4.6b. The nanowires appear single crystalline throughout the tapered segments, with a clear {111} sidewall at the junctions facing away from the growth direction. This geometry suggests that the conformal deposition and growth occurs in 3-D: grows laterally and overgrows some of the previously terminated sidewall towards the base. The precise quality of the overgrowth requires additional investigation.

The process was further optimized for slightly larger nanowires grown at an elevated temperature of 385 °C on Ge(111) substrate with 20 nm gold colloid shown in Figure 4.9 where the tapering is easily observed. Additional condition "H" was added that refers to 125 sccm H_2 at 2.2 Torr total pressure (i.e. H_2 only). The following steps were used in the growth this array listed in order with numbers corresponding to duration of the adjacent condition in minutes: 1 G, 1 G+T, 20 T, 5 H, 2 G, 1/3 T, 2 G, 1/3 T, 2 G,

1/3 T. The addition of H_2 only condition after alloying step was added as a precautionary measure to purge the chamber from residual TMT vapor residues and led to more consistent results. Elevated temperature is observed to aid the formation of clear downward facing facets from conformal deposition.

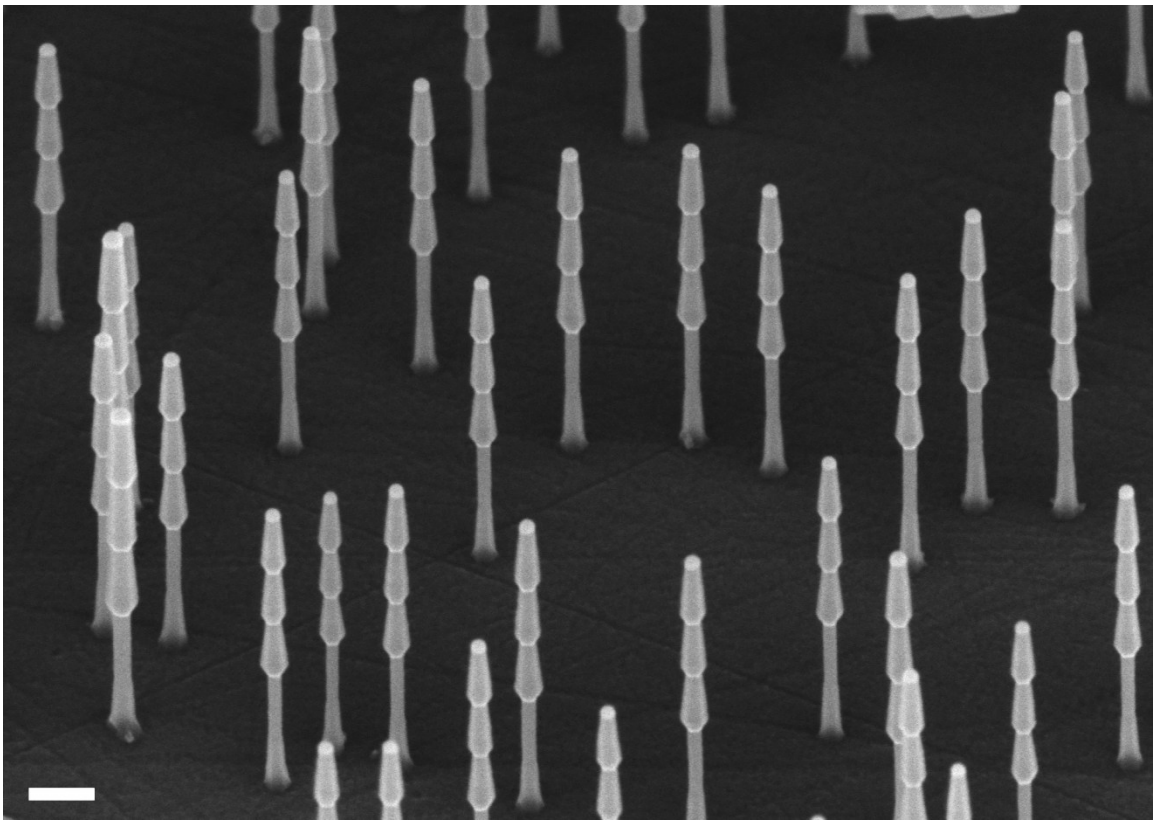

Figure 4.9 SEM image of the diameter-modulated superstructure array growth at 385 °C observed at a 45° inclined angle. Scale bar, 100 nm

4.4 Conclusions

We have demonstrated diameter-modulated nanowire superstructures by systematically modifying sidewall surface chemistry during vapor-liquid-solid (VLS) synthesis. Our approach relies on the addition of a "molecular resist," TMT in the present case, which inhibits radial deposition at user-defined points during nanowire growth. Superstructure dimensions can be rationally tuned via segment growth time as well as Sn alloying in the catalyst, which increases the radial-to-axial growth rate ratio. The use of surface chemistry to modulate radial deposition rates is a general concept and its application to other materials systems (e.g. Si) is only limited by catalyst and precursor selection. In addition to diameter-modulation, robust control of sidewall termination also promises new opportunities to engineer dopant atom incorporation and heterostructure formation.

4.5 References

1. C. K. Chan, H. L. Peng, G. Liu, K. McIlwrath, X. F. Zhang, R. A. Huggins and Y. Cui, *Nat. Nanotechnol.*, 2008, **3**, 31-35.

2. Z. Y. Fan, H. Razavi, J. W. Do, A. Moriwaki, O. Ergen, Y. L. Chueh, P. W. Leu, J. C. Ho, T. Takahashi, L. A. Reichertz, S. Neale, K. Yu, M. Wu, J. W. Ager and A. Javey, *Nat. Mater.*, 2009, **8**, 648-653.

3. A. I. Boukai, Y. Bunimovich, J. Tahir-Kheli, J. K. Yu, W. A. Goddard and J. R. Heath, *Nature*, 2008, **451**, 168-171.

4. Y. Huang, X. F. Duan, Y. Cui, L. J. Lauhon, K. H. Kim and C. M. Lieber, *Science*, 2001, **294**, 1313-1317.

5. H. T. Ng, J. Han, T. Yamada, P. Nguyen, Y. P. Chen and M. Meyyappan, *Nano Lett.*, 2004, **4**, 1247-1252.

6. C. Thelander, H. A. Nilsson, L. E. Jensen and L. Samuelson, *Nano Lett.*, 2005, **5**, 635-638.

7. S. Cahangirov and S. Ciraci, *Phys. Rev. B*, 2009, **80**, 075305.

8. J.-E. Yang, C.-B. Jin, C.-J. Kim and M.-H. Jo, *Nano Lett.*, 2006, **6**, 2679-2684.

9. X. Zianni, *Appl. Phys. Lett.*, 2010, **97**, 233106-233103.

10. A. I. Hochbaum, R. K. Chen, R. D. Delgado, W. J. Liang, E. C. Garnett, M. Najarian, A. Majumdar and P. D. Yang, *Nature*, 2008, **451**, 163-U165.

11. O. L. Muskens, S. L. Diedenhofen, B. C. Kaas, R. E. Algra, E. P. A. M. Bakkers, J. Gómez Rivas and A. Lagendijk, *Nano Lett.*, 2009, **9**, 930-934.

12. L. Hu and G. Chen, *Nano Lett.*, 2007, **7**, 3249-3252.

13. V. Schmidt, J. V. Wittemann and U. Gosele, *Chem. Rev.*, 2010, **110**, 361-388.

14. K. A. Dick, *Prog. Cryst. Growth Charact. Mater.*, 2008, **54**, 138-173.

15. H. J. Fan, P. Werner and M. Zacharias, *Small*, 2006, **2**, 700-717.

16. A. D. Gamalski, C. Ducati and S. Hofmann, *J. Phys. Chem. C*, 2011, **115**, 4413-4417.

17. F. M. Ross, *Rep. Prog. Phys.*, 2010, **73**, 114501.

18. E. Sutter and P. Sutter, *Nano Lett.*, 2008, **8**, 411-414.

19. H. Adhikari, A. F. Marshall, C. E. D. Chidsey and P. C. McIntyre, *Nano Lett.*, 2006, **6**, 318-323.

20. I. R. Musin and M. A. Filler, *Nano Lett.*, 2012, **12**, 3363-3368.

21. P. Madras, E. Dailey and J. Drucker, *Nano Lett.*, 2009, **9**, 3826-3830.

22. T. I. Kamins, X. Li, R. S. Williams and X. Liu, *Nano Lett.*, 2004, **4**, 503-506.

23. P. Caroff, K. A. Dick, J. Johansson, M. E. Messing, K. Deppert and L. Samuelson, *Nat. Nanotechnol.*, 2009, **4**, 50-55.

24. S. K. Lim, S. Crawford, G. Haberfehlner and S. Gradečak, *Nano Lett.*, 2012, **13**, 331-336.

25. M. Hocevar, G. Immink, M. Verheijen, N. Akopian, V. Zwiller, L. Kouwenhoven and E. Bakkers, *Nat Commun*, 2012, **3**, 1266.

26. B.-S. Kim, M. J. Kim, J. C. Lee, S. W. Hwang, B. L. Choi, E. K. Lee and D. Whang, *Nano Lett.*, 2012, **12**, 4007-4012.

27. C. J. Hawley, T. McGuckin and J. E. Spanier, *Cryst. Growth Des.*, 2013, **13**, 491-496.

28. J. H. Woodruff, J. B. Ratchford, I. A. Goldthorpe, P. C. McIntyre and C. E. D. Chidsey, *Nano Lett.*, 2007, **7**, 1637-1642.

29. D. E. Perea, E. R. Hernesath, E. J. Schwalbach, J. L. Lensch-Falk, P. W. Voorhees and L. J. Lauhon, *Nat. Nanotechnol.*, 2009, **4**, 315-319.

30. D. E. Perea, N. Li, R. M. Dickerson, A. Misra and S. T. Picraux, *Nano Lett.*, 2011, **11**, 3117-3122.

31. J. Y. Lee, J. Y. Maeng, A. Kim, Y. E. Cho and S. Kim, *J. Chem. Phys.*, 2003, **118**, 1929-1936.

32. B. Cunningham, J. O. Chu and S. Akbar, *Appl. Phys. Lett.*, 1991, **59**, 3574-3576.

33. R. P. Johnson and S. J. W. Price, *Can. J. Chem.*, 1972, **50**, 50-54.

34. J. Kouvetakis, A. Haaland, D. J. Shorokhov, H. V. Volden, G. V. Girichev, V. I. Sokolov and P. Matsunaga, *J. Am. Chem. Soc.*, 1998, **120**, 6738-6744.

35. K. D. Dobbs and W. J. Hehre, *Organometallics*, 1986, **5**, 2057-2061.

36. H. Ishii, Y. Takahashi and K. Fujinaga, *J. Electrochem. Soc.*, 1995, **142**, 1952-1956.

37. Y. Y. Fang, J. Tolle, J. Tice, A. V. G. Chizmeshya, J. Kouvetakis, V. R. D'Costa and J. Menéndez, *Chem. Mater.*, 2007, **19**, 5910-5925.

38. Y.-D. Ko, J.-G. Kang, G.-H. Lee, J.-G. Park, K.-S. Park, Y.-H. Jin and D.-W. Kim, *Nanoscale*, 2011, **3**, 3371-3375.

39. F. A. Trumbore, *J. Electrochem. Soc.*, 1956, **103**, 597-600.

40. Y. Feutelais, B. Legendre and S. G. Fries, *Calphad*, 1996, **20**, 109-123.

41. K. K. Lew, L. Pan, E. C. Dickey and J. M. Redwing, *J. Mater. Res.*, 2006, **21**, 2876-2881.

42. D. R. Stull, *Ind. Eng. Chem.*, 1947, **39**, 517-540.

43. M. Jeon and K. Kamisako, *Mater. Lett.*, 2009, **63**, 777-779.

44. L. Yu, B. O'Donnell, J.-L. Maurice and P. R. i. Cabarrocas, *Appl. Phys. Lett.*, 2010, **97**, 023107.

CHAPTER 5

DIAMETER MODULATION AS A ROUTE TO PROBE THE GROWTH KINETICS OF SEMICONDUCTOR NANOWIRES

5.1 Introduction

The vapor-liquid-solid (VLS) technique is the dominant synthesis method and offers control of nanowire length, diameter, orientation, composition, and doping, but often within a narrow range.[1-4] The long-term, practical utilization of nanowires will therefore require advanced growth protocols and, in pursuit of this goal, a robust understanding of process-structure-property relationships is essential. However, the few global process variables that govern growth, particularly substrate temperature, precursor species, and partial pressure, generate a vast phase space for exploration. In order to accelerate process development, we propose a method for determining basic growth kinetics for a range of conditions in one experiment. More specifically, we fabricate diameter-modulated nanowires and utilize the user-generated changes to sidewall morphology as indicators of growth rate. We note that similar studies are also possible via dopant profile modulation,[5, 6] but that measurement of the morphology changes shown herein is straightforward with electron microscopy.

Modulation of nanowire diameter, a prerequisite for the approach outlined here, is governed by adsorption and desorption on the nanowire sidewall. Most frequently, the tapering of nanowires grown with hydride species (i.e., GeH_4) is a

function of substrate temperature and precursor pressure.[7-9] By analogy to thin films, GeH_4 decomposition delivers hydrogen atoms to the nanowire sidewall that act as a resist, limiting vapor-solid (VS) deposition and enabling untapered growth at low temperature.[10, 11] As the temperature rises and the removal of adsorbed hydrogen via H_2 desorption accelerates,[12] surface sites become available for additional GeH_4 decomposition and tapering increases.

Recent demonstrations show that nanowire tapering can also be controlled, at constant temperature and pressure, by chemically passivating the sidewall. For example, O_2 and C_2H_2/HCl react at the triple-phase line to create amorphous oxide and carbon shells, respectively, that prevent VS deposition.[13, 14] We recently reported on a series of "molecular resists" that react with the sidewall directly.[15, 16] As these species can passivate and prevent VS deposition on previously grown segments, it becomes possible to create diameter-modulated structures by growing and subsequently terminating tapered segments. While many precursors can terminate the nanowire sidewall, a number of additional effects are frequently induced. For example, methylgermane (GeH_3CH_3) results in growth direction changes (i.e., kinking)[15] and tetramethyltin ($Sn(CH_3)_4$) reduces the axial growth rate.[16]

Here, we identify trimethylsilane ($SiH(CH_3)_3$, TMSH) as a precursor that resists VS deposition without permanently modifying growth direction and/or rate. TMSH consists of a central Si atom, one labile Si–H bond, and three, more stable methyl groups. The Si–H bond of TMSH is expected to react with the nanowire sidewall at locations vacated following H_2 desorption, therefore anchoring TMSH

to the surface, blocking GeH_4 adsorption, and preventing tapering. The lower reactivity of Si–H (3.9 eV) relative to Ge–H (3.6 eV),[17-19] in addition to the steric hindrance imparted by the methyl groups in TMSH, ensures that GeH_4 decomposition remains the dominant reaction in the catalyst droplet under standard nanowire growth conditions (i.e., $T \leq 385$ °C). However, in the event of TMSH decomposition in the catalyst droplet, C is poorly soluble in Au and unlikely to impact growth.[20] While Si atoms are miscible in Au,[19, 21] we show that separating axial elongation (i.e., without TMSH) and sidewall termination (i.e., with TMSH) prevents Si accumulation in the catalyst droplet.

5.2 Experimental Details

Single-side polished Ge(111) wafers (MTI Corporation, CZ, 42–64 Ω-cm) are cleaved into ~0.5 cm^2 substrates and cleaned with a sequence of 10% HF etching, deionized water rinsing, and N_2 drying. Gold colloid with diameters of 20, 30, 40, and 50 nm (≤8% coefficient of variation, Ted Pella, BBI) are subsequently deposited on each substrate. To ensure proper adhesion and a clean Au/Ge interface, 0.3% HF is added to each colloid solution immediately prior to drop casting.[22] All substrates are then rinsed in deionized water and dried under N_2 prior to insertion into the growth reactor.

Ge nanowires are grown in a cold-wall FirstNano EasyTube 3000 CVD system on a graphite susceptor heated from the bottom by infrared lamps. Four substrates, each with a different colloid diameter, are processed simultaneously and aligned perpendicular to the direction of gas flow. Germane (GeH_4, 99.999%,

Matheson Tri-Gas), hydrogen (H_2, 99.999%, AirGas), and trimethylsilane ($SiH(CH_3)_3$, 99.99%, Voltaix) are used without further purification.

The following procedure results in a tapered base that is standard for all nanowires. Substrates are first exposed to 2.2 Torr H_2, ramped to 385 °C, and stabilized for 1 min. Nanowire growth is then started with 0.28 Torr GeH_4 and 1.92 Torr H_2 at 385 °C for 2 min. Sidewall passivation is then accomplished with a two step sequence consisting of (i) 0.27 Torr GeH_4, 0.12 Torr TMSH, and 1.81 Torr H_2 for 5 sec and (ii) 0.14 Torr TMSH and 2.06 Torr H_2 for another 2 min. The 5 sec step is included to prevent Au diffusion during the removal of GeH_4 and ensures that the catalyst droplet diameter remains constant. This procedure yields arrays of nanowire bases with greater than 90% vertical alignment and lengths of 202, 233, 242, 261 nm for 20, 30, 40, 50 nm colloid, respectively.[7, 22, 23] Segments are then grown as described in the text. Samples are cooled to room temperature under H_2 flow upon completing growth.

Scanning electron microscopy (SEM) of as-grown nanowire arrays is accomplished with Zeiss Ultra 60 and Leo 1530 instruments. High resolution transmission electron microscopy (HR-TEM) of nanowire structure is performed with a FEI Titan S 80 – 300 microscope following ultrasonication of substrates in methanol and drop casting onto lacey carbon grids (Ted Pella). A Cs-corrected JEOL 2200FS equipped with a Bruker-AXS X-Flash 5030 silicon drift detector enables energy dispersive X-ray spectroscopy (EDX) of nanowire catalyst droplet composition.

5.3 Results and Discussion

5.3.1 Synthesis of Diameter Modulated Heterostructures with TMSH

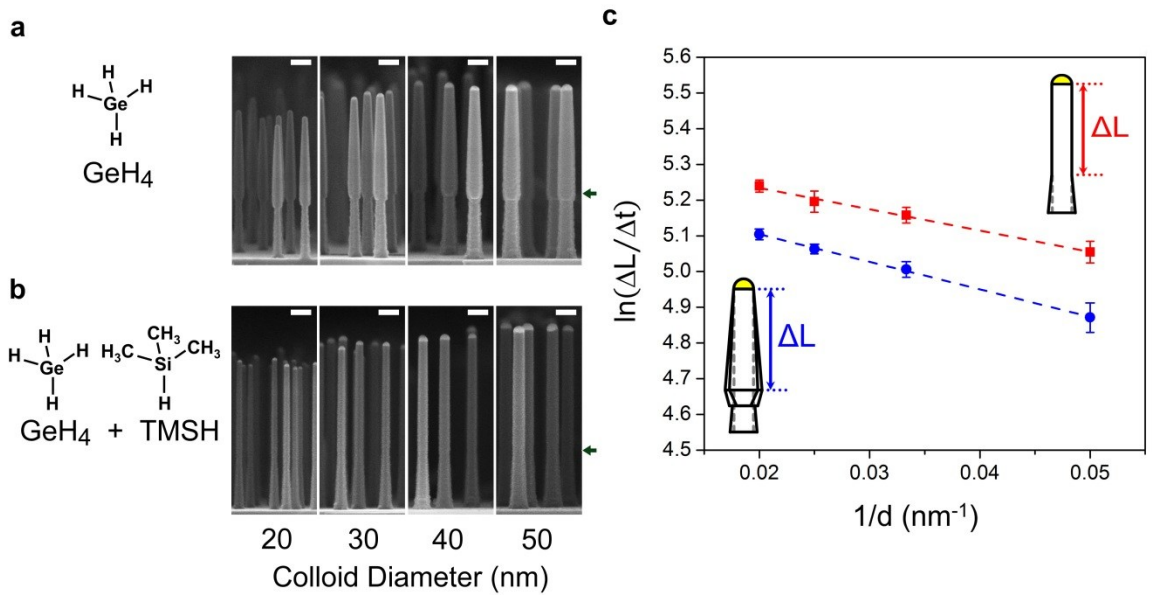

Figure 5.1 Side view SEM images of Ge nanowire arrays grown with a standard base followed by (a) 3 min with 0.28 Torr GeH_4 and 1.92 Torr H_2 or (b) 3 min with 0.28 Torr GeH_4, 0.12 Torr TMSH, and 1.89 Torr H_2 at 385 °C. Arrows denote the position of the catalyst droplet at the start of TMSH exposure. Scale bars, 100 nm. (c) Axial elongation rate, plotted as natural log of $\Delta L/\Delta t$ (nm/min), as a function of colloid diameter for the nanowires shown in (a) and (b) with circles and squares, respectively. Insets: schematic illustrations of the ΔL measurement end-points in both cases.

We begin by assessing the impact of TMSH on axial growth rate and VS deposition. Figure 5.1a shows Ge nanowires grown from gold colloid with diameters of 20, 30, 40, and 50 nm where the upper segment is grown for 3 min at 385 °C with 0.28 Torr GeH_4 and 1.92 Torr H_2. A tapered base is clearly visible (below the arrow), which is passivated with TMSH and thus resists VS deposition during growth of the upper segment. On the other hand, the upper segment exhibits significant taper since TMSH is absent during its elongation. Figure 5.1b shows

nanowires, grown with the same base (below the arrow), but subsequently elongated for 3 min at 385 °C with 0.28 Torr GeH_4, 0.12 Torr TMSH, and 1.89 Torr H_2. Tapering is significantly reduced at all points above the base due to co-flow of GeH_4 and TMSH. The probability of nanowire kinking with TMSH is negligible, and is particularly helpful for these experiments. A study of the related precursor methylsilane (SiH_3CH_3, MS) shows that this is not always the case (Figure 5.2), most significant with the 20 nm colloid diameter where 100% of the nanowires kink. Despite the dramatic reduction in VS deposition observed following or during TMSH addition, minor sidewall roughening is present far from the catalyst droplet and indicates that resistance to attack by GeH_4 is imperfect.

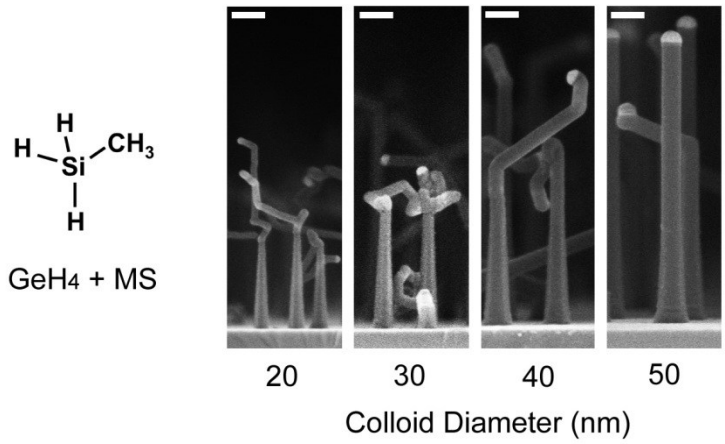

Figure 5.2 Side view SEM images of Ge nanowires grown with a standard base as described in the experimental details and followed by 3 minutes with 0.28 Torr GeH_4 and 0.12 Torr SiH_3CH_3. 100, 96, 86, and 51 % of the nanowires kink at least once for 20, 30, 40, and 50 nm colloid, respectively. Scale bars, 100 nm.

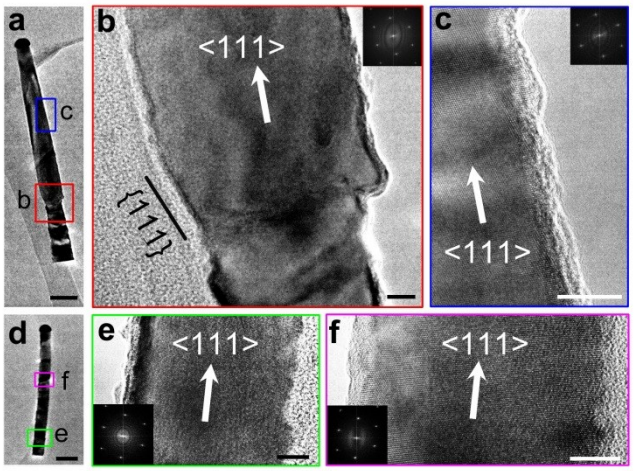

Figure 5.3 (a) Low magnification bright field TEM image along the [110] zone axis of a representative Ge nanowire from the array shown in Figure 5.1a. Scale bar, 100 nm. (b, c) High resolution bright field TEM images and FFT insets of the regions denoted by boxes in (a). Scale bars, 10 nm. (d) Low magnification bright field TEM image along the [110] zone axis of a representative Ge nanowire from the array shown in Figure 5.1b. Scale bar, 100 nm. The base is missing and likely broke during TEM grid preparation. Most nanowires exhibit this behaviour. (e, f) High resolution bright field TEM images and FFT insets of the regions denoted by boxes in (d). Scale bars, 10 nm.

Elongation rate ($\Delta L/\Delta t$) can be determined by dividing the upper segment length (ΔL) by its growth time (Δt). These data for nanowires grown with and without TMSH are plotted in Figure 5.1c as a function of diameter. As shown in the Figure 5.1c insets, the upper segment lengths are measured for the nanowires in Figure 5.1a and Figure 5.1b from the catalyst-nanowire interface to the point where the diameter is largest or where the sidewall slope changes, respectively (*vide infra*). The axes in Figure 5.1c are selected to linearize the data and are based on a recent model where growth rate is exponentially dependent on the inverse of diameter.[24] We find that growth rate is 14 - 20% faster in the presence of TMSH. The slope, which is related to the Gibbs-Thompson effect,[24-26] exhibits a reduction of 22% when the sidewall is passivated by TMSH. The y-intercept, which describes growth rate at infinite diameter, shows a smaller 2% increase.

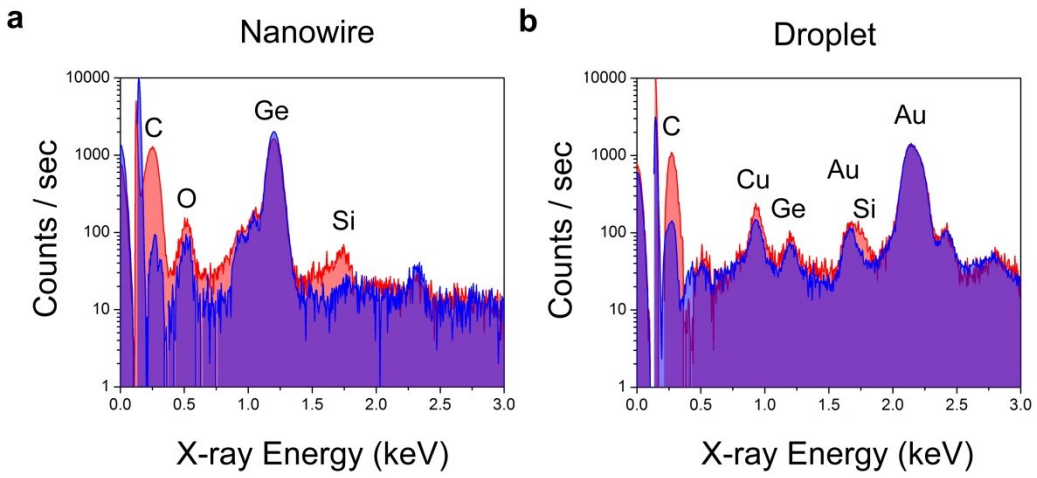

Figure 5.4 (a) EDX spectra of the upper segment for representative 50 nm Ge nanowires from the arrays in Figure 5.1a (shown in blue) and Figure 5.1b (shown in red). (b) EDX spectra of the catalyst droplet for representative 50 nm Ge nanowires from the arrays in Figure 5.1a (shown in blue) and Figure 5.1b (shown in red). Spectra in blue in (b) are scaled by 1/3. We note that EDX cannot distinguish between Si located in the bulk of or on the surface of the nanowire.

TEM analysis yields important information about nanowire crystal structure and morphology. Figures 5.3a-c display bright field TEM images of a representative Ge nanowire from the array shown in Figure 5.1a, where TMSH is added only for a brief period of time after base growth. The FFTs confirm that the nanowire is single crystalline and oriented in the <111> direction. Figure 5.3b shows the junction between the base and upper segment. A {111} facet oriented toward the substrate is clearly visible and results from conformal deposition. We make note of this point, as this is where nanowire diameter is greatest and, as shown in the Figure 5.1c inset, serves as the end-point of all segment length (ΔL) measurements. Figures 5.3d-f show bright field TEM images of a representative Ge nanowire from the array seen in Figure 5.1b, where the upper segment is grown in the continuous presence of TMSH. This nanowire is also single crystalline and

<111> oriented. Some sidewall roughness is detectable for both cases, likely from conformal deposition, and increases away from the catalyst droplet.

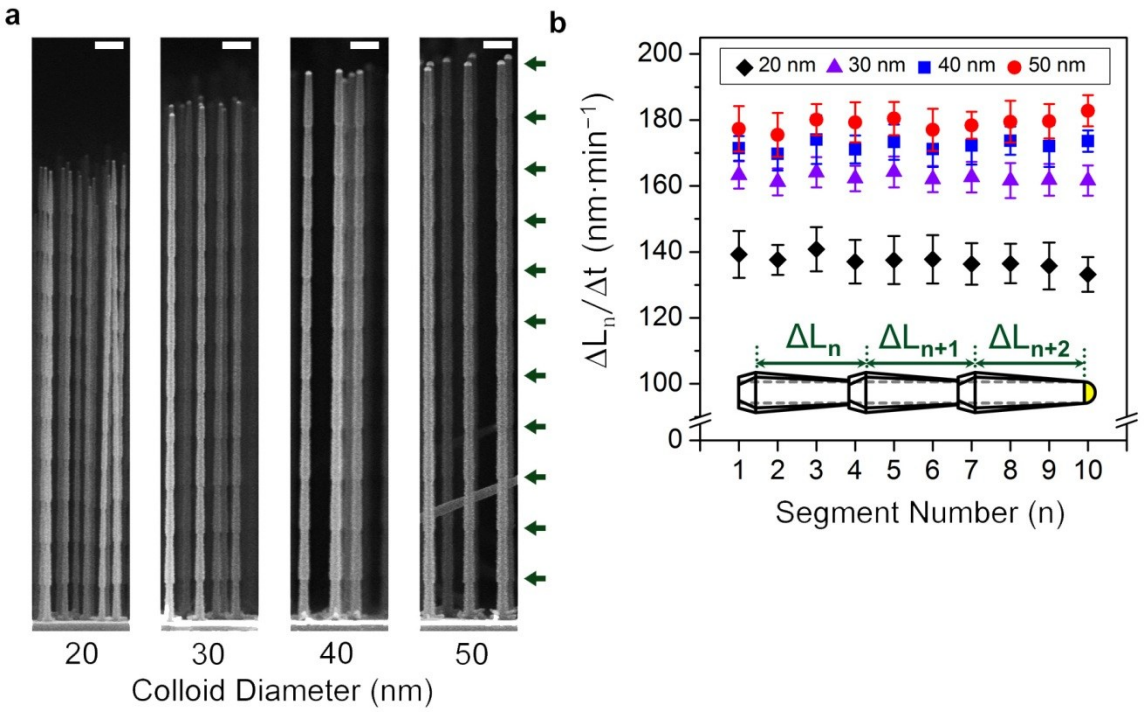

Figure 5.5 (a) Side view SEM images of Ge nanowire arrays grown with a standard base and followed by 10 diameter-modulation cycles, each consisting of 2 min with 0.28 Torr GeH_4 and 1.92 Torr H_2 and the standard passivation sequence at 385 °C. Arrows denote the position of the catalyst droplet during each TMSH exposure. Scale bars, 200 nm. (b) Axial elongation rate ($\Delta L_n/\Delta t$) plotted as a function of segment number (n) and gold colloid diameter. Inset: schematic illustration showing the ΔL_n measurement end-points. The diameter-modulated segment closest to the substrate is denoted n = 1.

Energy dispersive X-ray (EDX) spectra of the catalyst droplet for both nanowires (Figure 5.4) reveals the presence of Si in the catalyst droplet for situations where TMSH is co-delivered with GeH_4. This finding provides an explanation for the growth rate differences observed in Figure 5.1c. Importantly, the creation of a SiGeAu alloy may impact supersaturation and/or interface energetics, thus modifying growth rate and influencing our results. However, the

fact that no Si is found for the nanowire in Figure 5.1a suggests that decoupling the addition of TMSH (i.e., sidewall termination) and GeH_4 (i.e., nanowire elongation) will mitigate the impact of Si incorporation. Even if a small quantity Si is incorporated into the catalyst droplet during TMSH flow, the process is likely reversible on a time and length scale far shorter than segment growth. In other words, Si will be quickly expelled upon removal of TMSH and reinitiation of GeH_4 flow. Reports for $Si_{1-x}Ge_x$ heterostructures provide support for this reasoning.[27-29]

We demonstrate that separating TMSH and GeH_4 delivery results in constant nanowire growth rate as a function of axial position, which experimentally confirms that Si does not impact our results. Figure 5.5a shows nanowires with 10 diameter-modulated segments grown with 20, 30, 40, and 50 nm colloid. Each segment is achieved with 2 min at 0.28 Torr GeH_4 and 1.92 Torr H_2 followed by the standard passivation sequence at 385 °C. The former elongates the nanowire with concomitant VS deposition, while the later passivates the sidewall and inhibits additional tapering.

The elongation rate for each segment ($\Delta L_n/\Delta t$) is plotted as a function of segment number (n) in Figure 5.5b. Despite the observed sidewall roughening, which increases with distance away from the catalyst droplet, the shape and end points of each tapered segment are easily identifiable. Unless the properties of the catalyst (e.g., temperature, size, etc.) change as a function of distance from the substrate, the length of each diameter-modulated segment, and thus measured growth rate, should be constant. Consistent with this expectation, we find that

growth rate deviates from the first segment length by no more than 0.4 % per total number of segments. A clear diameter dependence, consistent with that observed in Figure 5.1, is also seen. These data confirm that nanowire growth, with discrete delivery of GeH_4 and TMSH, does not depend on axial position and permits the pressure- and temperature-dependent measurements discussed next.

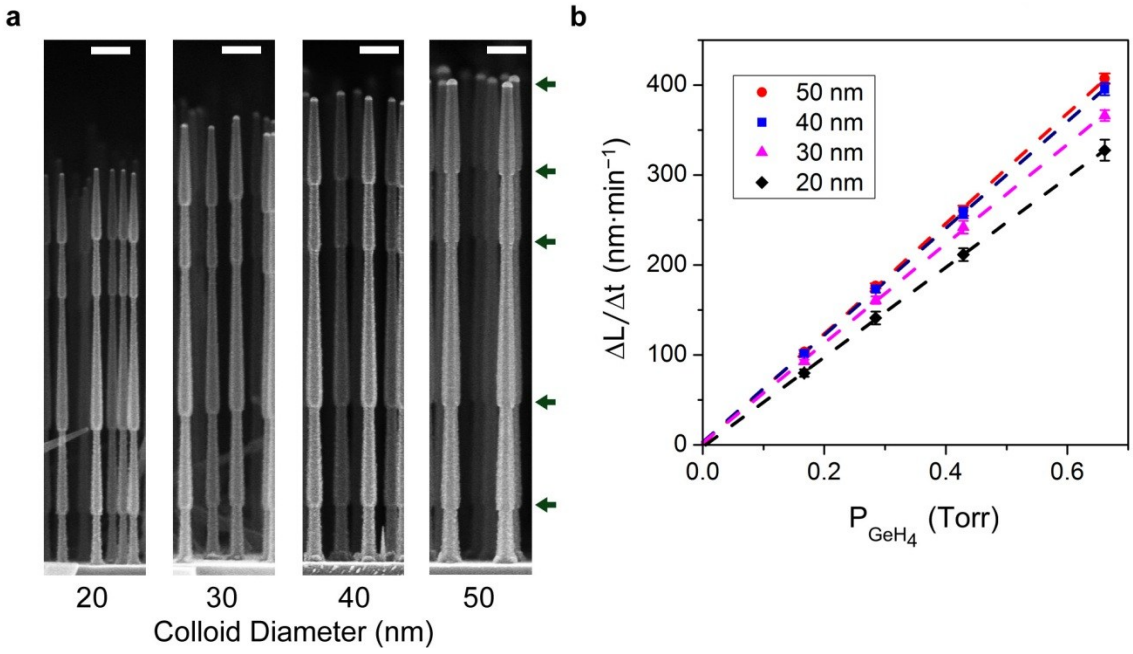

Figure 5.6 (a) Side view SEM images of Ge nanowire arrays grown with a standard base and followed by a sequence of pressure-dependent segments: 2 min with 0.28 Torr GeH_4, 2 min with 0.43 Torr GeH_4, 2 min with 0.66 Torr GeH_4, 2 min with 0.28 Torr GeH_4, and 4 min with 0.17 Torr GeH_4 with the balance as H_2 for all segments at 385 °C. The growth of each segment is followed by the standard passivation sequence. Arrows denote the position of the catalyst droplet during each TMSH exposure. Scale bars, 200 nm. (b) Axial elongation rate ($\Delta L/\Delta t$) plotted as a function of GeH_4 partial pressure and colloid diameter. Dashed lines are linear fits for each colloid size.

The dependence of nanowire growth on GeH_4 partial pressure is displayed in Figure 5.6. Here, each diameter-modulated segment is grown with different, but not monotonically increasing, GeH_4 partial pressure at a constant temperature of 385 °C and total pressure of 2.2 Torr. More specifically, the first three segments

(after the base) are each grown for 2 min with partial pressures of 0.43, 0.66, and 0.28 Torr GeH_4, respectively, with the balance as H_2. The final segment is grown at 0.17 Torr GeH_4 with the balance as H_2 for 4 min (i.e., twice the time) to ensure that tapering is observable. Similar to Figure 5.5, the standard passivation sequence is applied after the growth of each segment. We reemphasize that TMSH is only delivered between segment elongation steps and not during. Side view SEM images of the resulting nanowires are shown in Figure 5.6a. Nanowire elongation rate, measured in the same manner as above, is plotted as a function of GeH_4 partial pressure in Figure 5.6b for 20, 30, 40, and 50 nm colloid. Growth rate is clearly proportional to GeH_4 partial pressure as previously reported.[19] A diameter-dependent slope is also found and consistent with the other growth data included herein.

Diameter-modulation can also be utilized to explore the temperature dependence of nanowire growth. Six successive, segments are grown at 385, 330, 360, 300, and 385 °C for 3 min with 0.28 Torr GeH_4 and 1.92 Torr H_2. Each segment is passivated with the standard passivation sequence, during which the substrate is ramped to and stabilized at the next temperature. We note that the first and last segments are grown at the same temperature (i.e., 385 °C) to ensure consistency and that temperatures are not changed in a monotonic fashion. Figure 5.7a displays side view SEM images of the resulting nanowires. Sidewall tapering is clearly proportional to growth temperature as expected. The elongation rate of the two segments grown at 385 °C are within 5% of each other for all diameters and confirm that our results are independent of segment order or axial position.

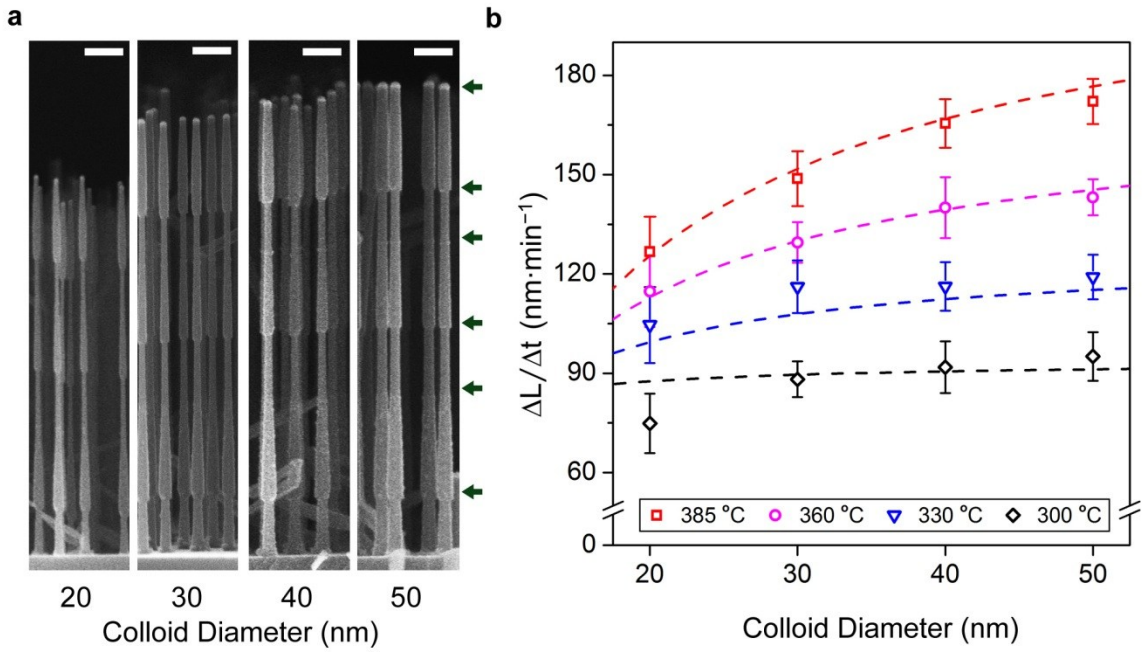

Figure 5.7 (a) Side view SEM images of Ge nanowires grown with standard base followed by a sequence of temperature-dependent segments at 0.28 Torr GeH_4 and 1.92 Torr H_2: 3 min at 385, 330, 360, 300, and 385 °C. Each temperature-dependent segment is followed by the standard passivation sequence, during which the substrate temperature is ramped to and held at the next condition. Arrows denote the position of the catalyst droplet during each TMSH exposure. Scale bars, 200 nm. (b) Axial elongation rate ($\Delta L/\Delta t$) plotted as a function of gold colloid diameter and substrate temperature. The dashed curves for each temperature are from a fit to the data based on Equation 5.7.

5.3.2 Empirical Model for Temperature, Pressure, and Diameter Phase Space Dependence

Many models have been proposed to describe VLS nanowire growth.[19, 24-26, 30] We fit our data to the recently reported model by N. Li et al,[24] but emphasize that the use of this model is largely illustrative of the fitting made possible by the rapid and accurate extraction of nanowire growth rate. The model assumes that nucleation at the liquid-solid interface is rate limiting and leads to the following expression for growth rate

$$dL/dt = \alpha \exp\left(-\frac{\beta}{d_S}\right), \tag{5.1}$$

with

$$\alpha = c^L \sqrt{\pi C_0^S}\lambda^{S\,5/2}\omega \exp\left(-\frac{\pi\lambda^S\Omega^S{\gamma_{LS}}^2}{2\left(kT\ln\left(\frac{C^L}{C_{eq}^L}\right)\right)^2}\ln\left(\frac{C^L}{C_{eq}^L}\right)\right), \tag{5.2}$$

$$\beta = \frac{\pi\lambda^S\left(\Omega^S\right)^2{\gamma_{LS}}^2}{kT\left(kT\ln\left(\frac{C^L}{C_{eq}^L}\right)\right)^2}\left(\frac{\Omega^S\gamma_{VS}-2\Omega^L\gamma_{VL}sin(\theta)}{\Omega^S}\right), \tag{5.3}$$

where d_S – nanowire diameter, C^L – Ge atom concentration in the droplet, ${C_{eq}}^L$ – Ge atom concentration in the catalyst droplet at equilibrium with the Ge solid assuming a flat liquid-solid interface, ${C_0}^S$ – volumetric atom density in the solid, λ^S – solid layer thickness, ω – capture rate of Ge atoms by growing island, Ω^S – solid Ge atom volume, Ω^L – liquid Ge atom volume, γ_{LS} – liquid-solid interface energy, γ_{VS} – vapor-solid interface energy, γ_{VL} – vapor-liquid interface energy, k – Boltzmann's constant, T – absolute temperature, θ is the catalyst droplet contact angle to the liquid-solid interface plane. The assumptions that $kT\ln(C^L/{C_{eq}}^L) >> 2(\Omega^S\gamma_{VS} - 2\Omega^L\gamma_{VL}\sin(\theta))/d_S$ and $\Omega^S \approx \Omega^L$ allow the terms dependent in nanowire diameter to be collected, which should be valid here when far from the critical diameters.[25]

The diameter and volume of the catalyst droplet, assuming a spherical shape, are related via $d_L = [(24V/\pi)(1+\cos(\theta))^{-2}(2-\cos(\theta))^{-1}]^{1/3}$. The diameter of the liquid catalyst droplet (d_L) and solid nanowire (d_S) beneath can be related via $d_S = d_L\sin(\theta)$. V is the actual volume of the catalyst droplet and can be expressed as V =

$d_{colloid}^3(\pi/6)/(1-C^L\Omega^L)$, assuming an ideal solution, where $d_{colloid}$ (nm) is the original diameter of the, assumed spherical, Au colloid nanoparticle. Substituting these relationships into the above equations provides growth rate as a function of Au colloid diameter

$$dL/dt = \alpha' \exp\left(-\frac{\beta'}{d_{colloid}}\right) P_{GeH_4}\,, \tag{5.4}$$

$$\alpha' = K\sqrt{\pi C_0^S}\lambda^{S\,5/2}\omega\exp\left(-\frac{\pi\lambda^S\Omega^S{\gamma_{LS}}^2}{2(kT)^2\ln\left(\frac{KP_{GeH_4}}{C_{eq}^L}\right)}\right), \tag{5.5}$$

$$\beta' = \frac{\pi\lambda^S\Omega^S{\gamma_{LS}}^2\left(\Omega^S\gamma_{VS}-2\Omega^L\gamma_{VL}\sin(\theta)\right)}{kT\left(kT\ln\left(\frac{KP_{GeH_4}}{C_{eq}^L}\right)\right)^2}\ \frac{(1+\sin(\theta))^{\frac{2}{3}}(2-\sin(\theta))^{\frac{1}{3}}}{\sin(\theta)}\left(\frac{1-KP_{GeH_4}\Omega^L}{4}\right)^{\frac{1}{3}}, \tag{5.6}$$

where $K = C^L/P_{GeH4}$ is a temperature-dependent equilibrium constant, assuming crystallization is rate limiting and P_{GeH4} is the partial pressure of GeH_4 (Torr). Based on the data shown in Figure 5.6, the pressure dependence appears nearly first order (1.00±0.02). Clearly, almost every unknown variable comprising the lumped parameters (i.e., α‘ and β’) varies with temperature. Thus, we determine, via fitting of our data, the functional form of the overall T dependence for each parameter using a minimum number of free variables. α‘ and β’ exhibit a exp(A×T) and B×T–C relationship, respectively, where A, B, and C are positive empirical constants. These dependencies lead to the following final rate expression

$$dL/dt = \exp(AT)\exp\left(-\frac{BT-C}{d_{colloid}}\right) P_{GeH4}\,. \tag{5.7}$$

We plot our data as $\ln(\Delta L/\Delta t/P_{GeH4})$ as a function of $1/d_{colloid}$, as shown in Figure 5.9a, to extract α' and β' from the slope and y-intercept, respectively. We find that $A = 1.01\times10^{-2}$, $B = 1.18\times10^{-1}$, and $C = 6.64\times10^{1}$ when using data collected at all the temperatures shown in Figure 5.7. This equation successfully captures, as shown in Figure 5.7b, the decrease of growth rate with decreasing diameter and the increase of diameter dependence with increasing temperature.

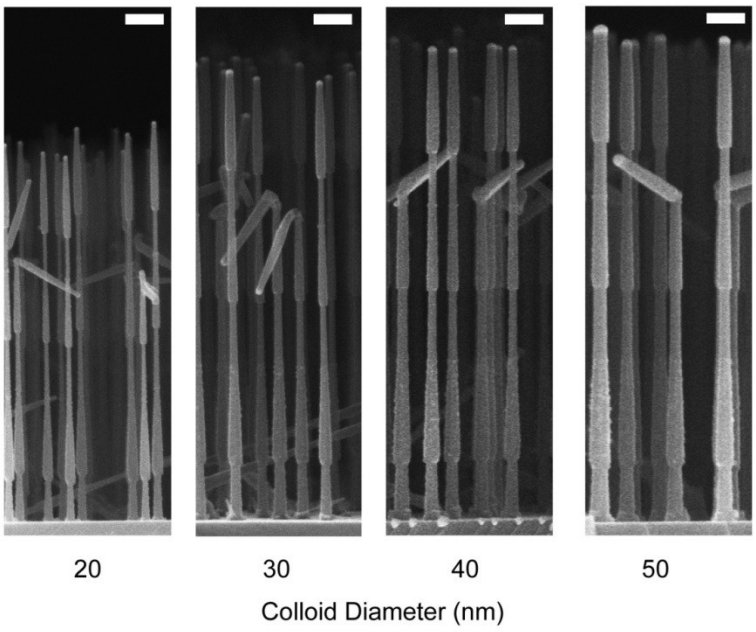

Figure 5.8 Additional side view SEM images of the samples in Figure 5.7 showing typical kinking and missing segments observed for segments grown at 300 °C. Scale bars, 200 nm.

We note that segments grown at 300 °C appear to deviate from the model prediction. At this temperature, we observe that the segment grown at 300 °C is kinked (Figure 5.8) and, in some instances, is missing entirely or undetectably short. We attribute both of these effects to solidification of the droplet upon removal of GeH_4 and cooling at the end of the previous segment. This behavior, which results in vapor-solid-solid (VSS) growth[31] and/or kinking,[23] is well-

documented during sub-eutectic Ge nanowire growth. Thus, we tentatively attribute the reduced elongation rate ($\Delta L/\Delta t$) to the extra time (Δt) needed for liquefaction of the solid catalyst when GeH_4 flow is reinitiated at the beginning of the segment. Nevertheless, the model is able to describe our results reasonably well, especially at larger diameters and higher temperatures where nanowires are less susceptible to solidification.[31]

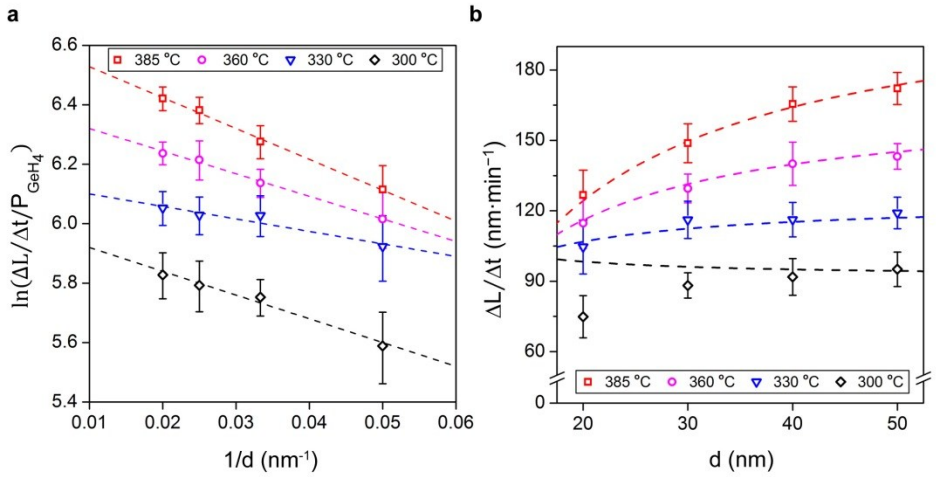

Figure 5.9 (a) Temperature data plotted in linearized version of equation 5.7. Dashed lines are linear fits to each individual temperature range. (b) Axial elongation rate ($\Delta L/\Delta t$) plotted as a function of gold colloid diameter and substrate temperature. The dashed curves for each temperature are from a fit of equation 5.7 to the data for 330 – 385 °C temperatures only, showing the reversal of the diameter dependence sign at 300 °C.

The model, when fitted to our data, suggests diameter-independent growth will occur at 290 °C; however, it's clear that our 300 °C data remains diameter-dependent. If we assume that the morphological and trend differences observed for growth at 300 °C are attributable to catalyst droplet phase change, then a fit without data at this temperature is warranted. This possibility is explored in Figure 5.9b, which shows the experimental data and model prediction when excluding the

300 °C data in the fit. We find $A = 1.01\times10^{-2}$, $B = 1.47\times10^{-1}$, and $C = 8.57\times10^{1}$ for this case. Importantly, this fit results in the prediction of an inverse diameter-dependence at temperatures below 310 °C that results from a sign change for β'. Such behaviour is known for other nanowire systems,[32-34] but its significance here, if any, requires additional investigation.

5.4 Conclusions

We demonstrate a new method for determining semiconductor nanowire growth rate at a range of pressures and temperatures. The technique relies on user-defined morphological markers, in the form of diameter-modulated segments positioned along the axial direction of VLS-synthesized nanowires, to rapidly and accurately measure length via electron microscopy. To demonstrate the usefulness of this approach, we fit an empirical expression for Ge nanowire growth rate as a function of diameter, substrate temperature, and precursor pressure with data extracted from just a single experiment. TMSH is an excellent precursor for this purpose due to its ability to passivate the sidewall without permanently impacting nanowire growth rate or direction. While additional studies are necessary to determine the chemical functionality responsible for the observed resistance to GeH_4 decomposition, we suggest that $–CH_3$ moieties play an important role. Finally, we note that chemical termination of the sidewall, when accomplished without influencing the triple-phase line, is beneficial for dopant profile and heterostructure engineering.

5.5 References

1. V. Schmidt, J. V. Wittemann, S. Senz and U. Gosele, *Adv. Mater.*, 2009, **21**, 2681-2702.

2. E. Koren, N. Berkovitch and Y. Rosenwaks, *Nano Lett.*, 2010, **10**, 1163-1167.

3. F. M. Ross, *Rep. Prog. Phys.*, 2010, **73**, 114501.

4. K. W. Schwarz, J. Tersoff, S. Kodambaka, Y. C. Chou and F. M. Ross, *Phys. Rev. Lett.*, 2011, **107**, 265502.

5. F. Glas, J.-C. Harmand and G. Patriarche, *Phys. Rev. Lett.*, 2010, **104**, 135501.

6. H. Schmid, M. T. Björk, J. Knoch, S. Karg, H. Riel and W. Riess, *Nano Lett.*, 2008, **9**, 173-177.

7. H. Jagannathan, M. Deal, Y. Nishi, J. Woodruff, C. Chidsey and P. C. McIntyre, *J. Appl. Phys.*, 2006, **100**.

8. S.-g. Ryu, E. Kim, J.-h. Yoo, D. J. Hwang, B. Xiang, O. D. Dubon, A. M. Minor and C. P. Grigoropoulos, *Acs Nano*, 2013, **7**, 2090-2098.

9. C.-B. Jin, J.-E. Yang and M.-H. Jo, *Appl. Phys. Lett.*, 2006, **88**, 193105-193103.

10. B. Cunningham, J. O. Chu and S. Akbar, *Appl. Phys. Lett.*, 1991, **59**, 3574-3576.

11. N. M. Russell and W. G. Breiland, *J. Appl. Phys.*, 1993, **73**, 3525-3530.

12. J. Y. Lee, J. Y. Maeng, A. Kim, Y. E. Cho and S. Kim, *J. Chem. Phys.*, 2003, **118**, 1929-1936.

13. C. J. Hawley, T. McGuckin and J. E. Spanier, *Cryst. Growth Des.*, 2013, **13**, 491-496.

14. B.-S. Kim, M. J. Kim, J. C. Lee, S. W. Hwang, B. L. Choi, E. K. Lee and D. Whang, *Nano Lett.*, 2012, **12**, 4007-4012.

15. I. R. Musin and M. A. Filler, *Nano Lett.*, 2012, **12**, 3363-3368.

16. I. R. Musin, D. S. Boyuk and M. A. Filler, *J. Vac. Sci. Technol., B*, 2013, **31**, 020603.

17. J. M. Buriak, *Chem. Rev.*, 2002, **102**, 1271-1308.

18. X. Yang and M. Tao, *J. Electrochem. Soc.*, 2007, **154**, H53-H59.

19. K. K. Lew, L. Pan, E. C. Dickey and J. M. Redwing, *J. Mater. Res.*, 2006, **21**, 2876-2881.

20. H. Okamoto and T. B. Massalski, *Bull. Alloy Phase Diagr.*, 1984, **5**, 378-379.

21. I. Sa, B.-M. Lee, C.-J. Kim, M.-H. Jo and B.-J. Lee, *Calphad*, 2008, **32**, 669-674.

22. J. H. Woodruff, J. B. Ratchford, I. A. Goldthorpe, P. C. McIntyre and C. E. D. Chidsey, *Nano Lett.*, 2007, **7**, 1637-1642.

23. J. H. Kim, S. R. Moon, H. S. Yoon, J. H. Jung, Y. Kim, Z. G. Chen, J. Zou, D. Y. Choi, H. J. Joyce, Q. Gao, H. H. Tan and C. Jagadish, *Cryst. Growth Des.*, 2011, **12**, 135-141.

24. N. Li, W. Li, L. Liu and T. Y. Tan, *J. Appl. Phys.*, 2013, **114**, 064302.

25. S. A. Dayeh and S. T. Picraux, *Nano Lett.*, 2010, **10**.

26. E. I. Givargizov, *J. Cryst. Growth*, 1975, **31**, 20-30.

27. D. E. Perea, N. Li, R. M. Dickerson, A. Misra and S. T. Picraux, *Nano Lett.*, 2011, **11**, 3117-3122.

28. T. E. Clark, P. Nimmatoori, K. K. Lew, L. Pan, J. M. Redwing and E. C. Dickey, *Nano Lett.*, 2008, **8**, 1246-1252.

29. C. Y. Wen, M. C. Reuter, J. Bruley, J. Tersoff, S. Kodambaka, E. A. Stach and F. M. Ross, *Science*, 2009, **326**, 1247-1250.

30. Y. Y. Lü, H. Cui, G. W. Yang and C. X. Wang, *Nano Lett.*, 2012, **12**, 4032-4036.

31. S. Kodambaka, J. Tersoff, M. C. Reuter and F. M. Ross, *Science*, 2007, **316**, 729-732.

32. K. A. Dick, K. Deppert, L. Samuelson and W. Seifert, *J. Cryst. Growth*, 2006, **297**, 326-333.

33. D. S. Kim, U. Gösele and M. Zacharias, *J. Cryst. Growth*, 2009, **311**, 3216-3219.

34. J. Bauer, V. Gottschalch, H. Paetzelt, G. Wagner, B. Fuhrmann and H. S. Leipner, *J. Cryst. Growth*, 2007, **298**, 625-630.

CHAPTER 6

CONCLUSIONS

6.1 Impact and Related Work

In recent years, the significance of user defined chemistry-structure relationship in VLS has been demonstrated by several reports. The incorporation of atoms into the nanowire from the droplet is the foundation of VLS growth and has been known from the initial observations. Much early work was spent on studying basic thermodynamic effects from temperature and pressure variations, and the resulting properties of observed nanowires[1-4] with precursors borrowed from thin film chemistry. However, the first direct confirmation of surface chemistry effect on the VLS growth of nanowires was shown by Shin, et al only in 2012.[5] The authors grew Si nanowires with Si_2H_6 and an in-situ FTIR spectrometer correlating strong Si-H signals to <110> oriented nanowires at low temperatures and high pressures and weak S-H signals to <111> nanowires grown under high temperature and low pressure conditions. The relationship of surface hydrogen to morphology was then confirmed through introduction of atomic hydrogen that induced kinking to <112> from <111> of nanowires with diameters larger than 100 nm through chemical bonding. After all, temperature and pressure affect desorption and adsorption kinetics of chemical species on the sidewall, and not just the nucleation driving forces from semiconductor atoms. The importance of ligands (e.g. -H in Si_2H_6) used in vapor phase species became clearer.

In parallel, our research on Ge nanowire synthesis yielded similar results in kinking the nanowires via the use of additional methyl groups.[6] In both cases, at low temperatures where the surface species had longer lifetimes, a specific growth orientation was selected, while at higher temperatures or when surface species were not used, a different orientation became favorable. Just as the Si case was able to use atomic hydrogen to modulate growth orientation, we were able to do the same by modulating methyl containing GeH_3CH_3 species on and off from concurrent flow with GeH_4 creating kinking superstructures (Chapter 3). Further work demonstrated the ability to utilize surface-species-rich conditions to introduce defect planes into group IV nanowires for rational control of the lattice within same material.[7, 8] Even thin-shell formation was reported through reactions at the triple phase line with O_2[9] and C_2H_2/HCl[10] chemistries in addition to GeH_4. Overall, these studies demonstrated the ability to change structural properties of nanowires through reactions directly at the growth front by the triple phase line.

Other interface reactions of interest are on the sidewalls away from the droplet that govern the radial growth and tapering without impacting the growth front. In chapter 3, GeH_3CH_3/GeH_4 combined system was successfully used to reduce sidewall reactions and change growth orientation. However, the combined effect of tapering suppression and orientation control made it difficult deconvolute the effects with high selectivity. Chapters 4 and 5 focused on the use of surface species to block the sidewall termination without orientation control. To this end, we used tetramethyltin (Chapter 4) or trimethylsilane (Chapter 5) successfully as a molecular resist on the sidewall to govern where and when, during growth, the vapor-solid deposition was allowed to occur.[11] In

both cases, orientation controlling effects at triple phase line were suppressed. This allowed us to demonstrate chemical morphological control selectively at the sidewall, opening up an avenue to explore what makes reactions selective in VLS. For example, additional methyl groups on trimethylsilane, when compared to (mono)methylsilane, appear to quench the kinking mechanism, possibly due to steric effects and lower reactivity. We then took advantage of easily observed radial morphological changes to study effect of tetramethyltin on axial growth rate and various temperature and pressure process conditions in axial superstructures, rapidly on top of one another. Tetramethyltin appeared to have a secondary effect of slowing down axial growth permanently without permanently impacting the radial expansion.

The major contributions of this work are as follows. First, it introduced the concept of using concurrent or intermittent flows of growth and surface reacting groups for rapid chemical modulation via a highly reactive anchor group (Ge-H, Si-H, Sn-C) bonded to more stable groups (e.g. Ge-CH_3, Si–CH_3, Sn) for modifying surface chemical stability on demand. This stability in turn drives either stabilization of specific facet formations that lead to kinking or acts as a "molecular resist" and blocks conformal deposition directly on the sidewall at user-selected locations. This work allows robust generation of diameter modulated superstructures with user-defined expansions or introduction of changes in the crystal growth direction at user defined intervals from simply varying the precursors alone. The specific chemistry or the basic synthetic approach of allowing or blocking conformal deposition can be used by research groups around the world now to create and optimize the nanowire structure they want for the properties they need.

Temperature studies of MG growth suggested a link between decomposition of methyl groups on the Ge surfaces and growth orientation, matching the connection behind hydrogen decomposition on Si and growth orientations.[5] Similarly, rapid decomposition of surface hydrogen from Ge surfaces compared to more stable TMT or TMSH delivered moieties can influence the lateral dimensions. Overall, these studies also highlight the importance of selecting specific ligands for delivering semiconductor atoms in CVD processes. The decomposition of surface species with a clean desorption (such as with –H species) or decomposition with products remaining on surface (such as with –CH_3) will have to be taken into account. The stability of the ligands delivered to the nanowire surfaces have to be taken into consideration to predict the final morphology of nanowires rather than blindly explore the vast phase space of process parameters and functional group chemistry. This, in turn, allows rational engineering of the chemistry for the formation of specific user-defined predictable nanowire structure.

The other major contribution is the use of these morphological markers to study kinetics of growth under varying conditions (time of tetramethyltin exposure, temperatures, pressures) within a single wire. These morphological methods provide a simple way to rapidly extract kinetic profiles from *ex-situ* measurements and serve as calibration or exploration tools. These calibration recipes can be used to match process conditions between various reactors or to observe deviations from the standard conditions due to other experimental variables, such as additional precursors.

6.2 Future Outlook

The bottom-up synthesis of semiconductor nanowires has come a long way since its initial demonstration in 1964.[12] Vapor-liquid-solid (VLS) synthetic approach has

allowed many nanoscale material systems to be successfully demonstrated.[13] Methods are continuously investigated in forming structures with axial and radial compositional and dopant profiles, changes in growth orientations, defect introductions, modifications to sidewall morphologies, and other motifs. However, a majority of these studies are done through investigating the pressure and temperature phase space with chemical precursors designed for 2-D thin film growth. As this research field matures, the "low hanging fruits" of basic growth parameters will get rapidly exhausted and additional approaches will be vital to further progress. The empirical approaches to finding novel arbitrary structures through growth parameter exploration are limited and inefficient. A more direct approach is essential for creating new technologies and materials based on user demands. Nanowire growth field requires fundamental understanding of the chemistry-structure-property relationships for demanded applications. The addition of chemistry variation increases the phase space for VLS growth considerably while providing important new handles of the underlying synthesis, including synthesis far from the thermodynamic equilibrium. Ideally, researchers would want the ability to build complexity in nanostructures much like an organic chemist builds complexity in molecules via specific and targeted steps from a synthetic "toolbox." The complexities of VLS growth, in particular three distinct phases and their relationships, force us to consider and design reactions for multiple interfaces.

Future progress in the field will have to address molecular precursor designs for selective reactions at multiple interfaces, degenerate symmetry of the crystal lattice, and high yield reproducibility. External fields (e.g. magnetic, electric, etc.), custom designed catalyst particles (alloys, multiphase), directional radiation (photon, electron, etc.),

addition of top-down approaches (etching, lithography, plasma processing, etc.), self-assembly on the nanostructures (Van der Waals attachment, click chemistry, polymerization, hydrophobic/hydrophilic interactions, etc.), and many other ideas are still available for expansion of the synthetic phase space and breaking away from the limitations and degeneracy of a simple symmetric crystal. For example, an external magnetic field may be used to break the symmetry of the catalyst particle and aid the nucleation event at a specific edge to allow formation of kinks to a specific among degenerate crystal growth directions. Combinations of etching and growth could allow formation of quantum scale nanowires or segments of nanowires grown at larger more controllable diameters. *In-situ* crystallographic and compositional analysis (e.g. environmental TEM, EDX, etc.), *in-situ* chemical bond detection tools (e.g. XPS, electron energy loss spectroscopy, Fourier transform infrared spectroscopy, Time-of-flight mass spectrometry, etc.), and *ex-situ* analysis (e.g. atom-probe tomography, SEM, etc.) provide methods of gaining further fundamental understanding in the chemistry-structure relationships of VLS growth. Furthermore, as more synthetic mechanisms are developed, the complexity of possible nanomaterials from their combinations will grow rapidly.

Mastering the chemistry-structure relationship would allow the design of nanowires for specific properties and applications that range from everything semiconductors are used for to more novel ideas. While the 1-D applications are the most apparent, VLS growth of nanowires can serve as a foundation for building complex 3-D architectures. Controlled changes in compositions, orientations, radial and axial dimensions could also theoretically allow bottom-up synthesis, or self-assembly, of very

complex designs at the nanoscale like 3-D nanoprinters. It is not difficult to imagine only needing the seed particles on a growth surface to create unlimited copies of high-complexity user programmable designs simultaneously, side-by-side in roll-to-roll like processing.

6.3 References

1. V. Schmidt, J. V. Wittemann and U. Gosele, *Chem. Rev.*, 2010, **110**, 361-388.

2. K. W. Schwarz, J. Tersoff, S. Kodambaka, Y. C. Chou and F. M. Ross, *Phys. Rev. Lett.*, 2011, **107**, 265502.

3. E. Dailey, P. Madras and J. Drucker, *Appl. Phys. Lett.*, 2010, **97**, 143106.

4. E. A. Sutter and P. W. Sutter, *Acs Nano*, 2010, **4**, 4943-4947.

5. N. Shin and M. A. Filler, *Nano Lett.*, 2012, **12**, 2865-2870.

6. I. R. Musin and M. A. Filler, *Nano Lett.*, 2012, **12**, 3363-3368.

7. N. Shin, M. Chi, J. Y. Howe and M. A. Filler, *Nano Lett.*, 2013, **13**, 1928-1933.

8. N. Jeon, S. A. Dayeh and L. J. Lauhon, *Nano Lett.*, 2013, **13**, 3947-3952.

9. C. J. Hawley, T. McGuckin and J. E. Spanier, *Cryst. Growth Des.*, 2013, **13**, 491-496.

10. B.-S. Kim, M. J. Kim, J. C. Lee, S. W. Hwang, B. L. Choi, E. K. Lee and D. Whang, *Nano Lett.*, 2012.

11. I. R. Musin, D. S. Boyuk and M. A. Filler, *J. Vac. Sci. Technol., B*, 2013, **31**, 020603.

12. R. S. Wagner and W. C. Ellis, *Appl. Phys. Lett.*, 1964, **4**, 89-90.

13. K. W. Kolasinski, *Curr. Opin. Solid State Mater. Sci.*, 2006, **10**, 182-191.